Basin and Petroleum System Modeling
9th Annual Industrial Affiliates Meeting
and
Field Trip to Santa Cruz-San Mateo County Coast Petroleum Systems

November 1-3, 2016
Stanford, California

Meeting Guide compiled by
Allegra Hosford Scheirer and Jane Moss

Field Trip Guide by Allegra Hosford Scheirer, Steve Graham, and Les Magoon
http://bpsm.stanford.edu

2016 BPSM Industrial Affiliates

ConocoPhillips
Ecopetrol S.A. (new for 2016!)
Hess
Nexen
Pemex
Petrobras
Saudi Aramco
Southwestern Energy
Total Energy (new for 2016!)

with special thanks to
Biomarker Technologies, Inc.
Schlumberger
US DOE National Energy Technical Laboratory

Schedule of Events

Tuesday, 11/1/16, 5:30-7:30 p.m.	Icebreaker at Stanford Golf Course
Wednesday, 11/2/16, 9:00 a.m.-5:00 p.m.	Oral Session at Jasper Ridge Biological Preserve
Wednesday, 11/2/16, 6 p.m.	Group Dinner, Il Fornaio Restaurant, 520 Cowper St., Palo Alto, CA 94301
Thursday, 11/3/16, 7:30 a.m.-5:00 p.m.	Santa Cruz County Coastal Petroleum System Field Trip

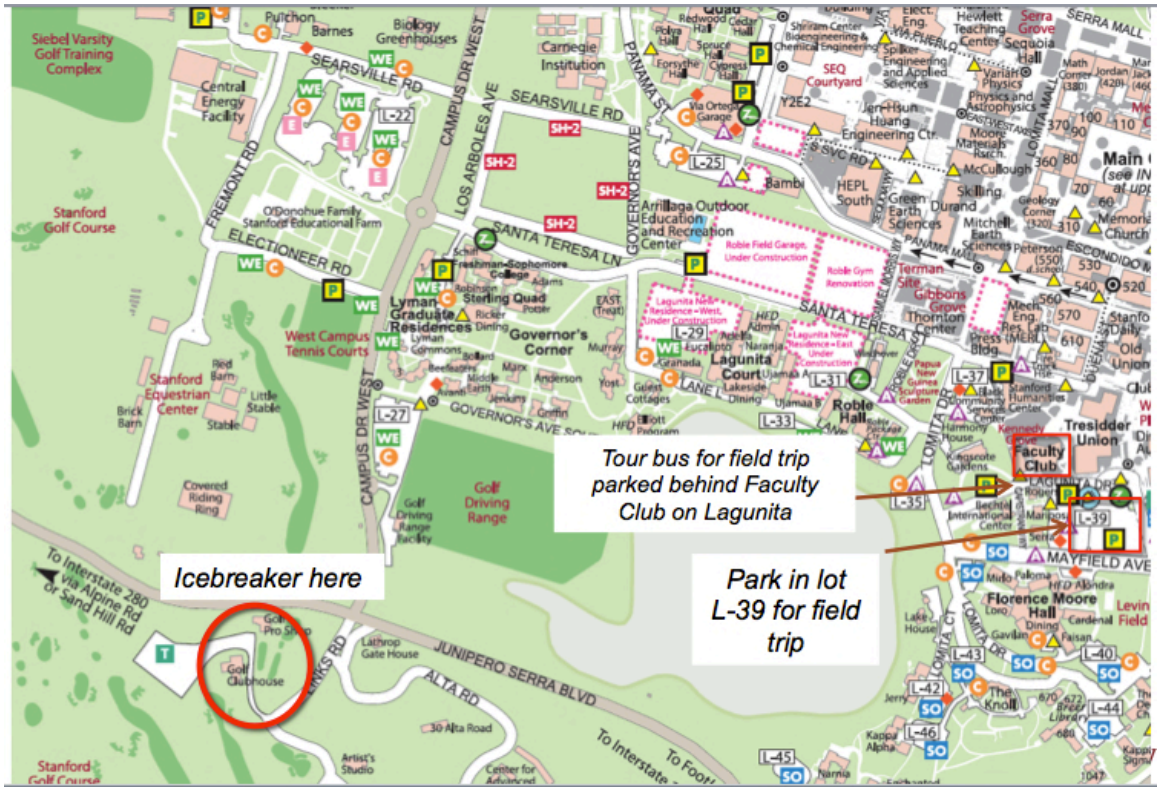

November 2, 2016, Oral Session Agenda

9:00 a.m.	**Steve Graham**, Introduction
9:20 a.m.	**Devon A. Orme**, A 3D subsidence analysis of the Great Valley forearc, California
9:55 a.m.	**Wisam AlKawai**, Allochthonous salt impact on reservoir architecture in the Thunder Horse Mini-basin, Gulf of Mexico
10:20-10:35 a.m.	**Coffee break**
10:35 a.m.	**Wisam AlKawai**, Constraining thermal and pressure history by combining basin modeling with rock physics: Applications to the Gulf of Mexico
11:05 a.m.	**Laura Dafov,** Petroleum system characterization of Terrebonne Mini-basin gas hydrates in NW Walker Ridge Area (Gulf of Mexico)
11:20 a.m.	**Inessa Yurchenko**, Multiproxy reconstruction of depositional environments of the Shublik Fm of Arctic Alaska
12:00-1:30 p.m.	**Lunch and small group guided walking tour**
1:30 p.m.	**Iris Yang,** Mathematical modeling of fracture growth in source rock during kerogen thermal maturation
1:50 p.m.	**Will Thompson-Butler,** Geochemically distinct oil families in the Middle Magdalena Valley, Colombia
2:25 p.m.	**Zack Burton,** Towards a basin and petroleum system model for the Pegasus Basin, New Zealand
2:50 p.m.	**Mustafa Al Ibrahim**, Seismic characterization of the Shublik Formation, Alaska North Slope, for improved basin and petroleum system modeling
3:15 p.m.	**Laainam (Best) Chaipornkaew**, Basin-scale geomechanics of poroplasticity and its influence in predicting stress-strain behaviors and overpressure generation through geologic time
3:40-3:55 p.m.	**Coffee break**
3:55 p.m.	**Krongrath Suwannasri,** The effect of changes in permeability during maturation on pore pressure and petroleum migration in BPSM
4:15 p.m.	**Tanvi Chheda,** Introduction
4:25 p.m.	**Allegra Hosford Scheirer,** Update on Los Angeles Basin BPSM**,** Field Trip announcements for tomorrow

2016 Meeting Attendees

Attendee	Organization
Vladimir Blanco-Velandia	Ecopetrol
Kim Butler	Southwestern Energy Company
Sergey Doronichev	Schlumberger
Francois Gelin	Total E&P
Gretchen Gillis	Aramco Services Company
Lara Heister	Anadarko
Benjamin Kirkland	Nexen
Tom Lorenson	USGS
Veit Matt	ConocoPhillips
Zachary Miller	Anadarko
J. Mike Moldowan	Biomarker Technologies (also at Stanford)
Kenneth Peters	Schlumberger (also at Stanford)
Noelle Schoellkopf	Schlumberger (also at Stanford)
Yongkoo Seol	US DOE NETL
Johannes Wendebourg	Total

BPSM Scientists & Collaborators	Stanford University
Mustafa Al Ibrahim	Graduate Student
Wisam Alkawai	Graduate Student
Alan Burnham	Consulting Professor
Zachary Burton	Graduate Student
Laainam ("Best") Chaipornkaew	Graduate Student
Tanvi Chheda	Graduate Student
Laura Dafov	Graduate Student
Jeremy Dahl	Physical Science Research Associate
Nader Dutta	Visiting Scientist
Steve Graham	Professor and Co-Principal of BPSM
Allegra Hosford Scheirer	Co-Principal of BPSM
Les Magoon	Co-Principal of BPSM
Jane Moss	Webmaster & Assistant
Tapan Mukerji	Professor and Co-Principal of BPSM
Devon Orme	Postdoctoral Scholar
Krongrath Suwannasri	Graduate Student
Will Thompson-Butler	Graduate Student
Iris Yang	Graduate Student
Inessa Yurchenko	Graduate Student

2016 Meeting Abstracts

http://bpsm.stanford.edu

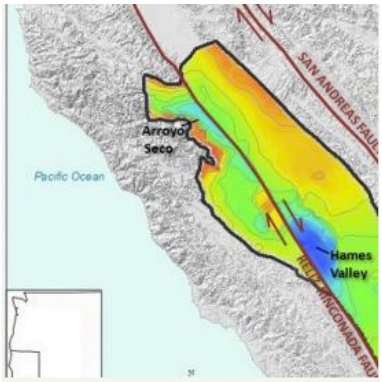

Salinas Basin, California

The Salinas basin is a Cenozoic strike-slip basin in the Coast Ranges of central California.

FAULTING STUDIES

SALINAS BASIN, CALIFORNIA

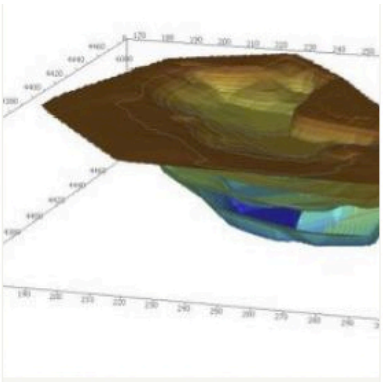

Piceance Basin, Colorado

The Piceance Basin is an asymmetrical sedimentary basin in the northeast part of the Colorado Plateau.

THEORETICAL STUDIES

PICEANCE BASIN, COLORADO

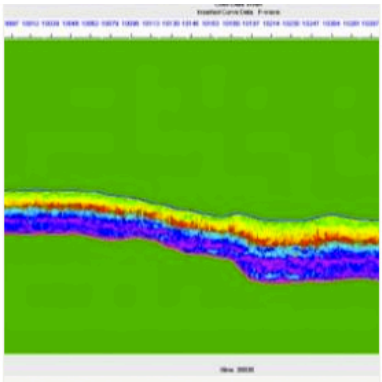

Gulf of Mexico

The study area in the Gulf of Mexico is located off the coast of Louisiana in the Ship Shoal and South Timbalier area.

PORE PRESSURE STUDIES

GULF OF MEXICO

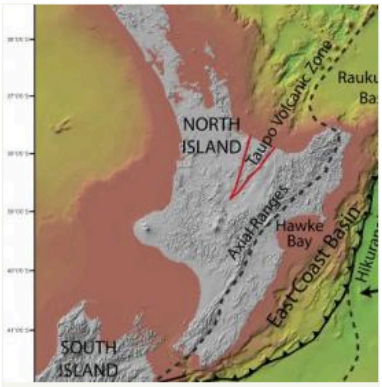

East Coast Basin, New Zealand

The East Coast Basin (ECB) is a petroliferous Neogene forearc basin located on the eastern margin on the North Island, New Zealand.

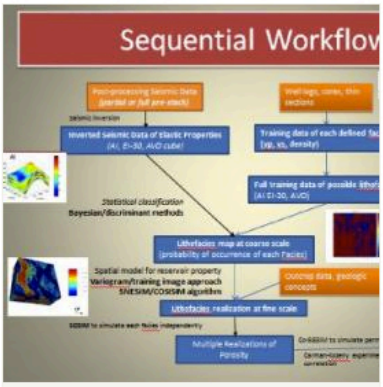

Understanding petrophysics of shale to calibrate regional basin models

Second-year Masters student Minh Tran works at the intersection of

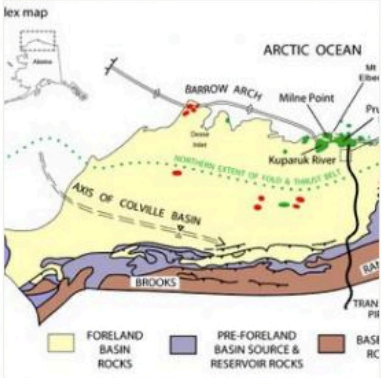

Source Rock Geochemistry, Stratigraphic Architecture, Unconventional Shale Resource Analysis and Petroleum System Modeling: Central North Slope

ASSESSING CONTROLS ON FOREARC BASIN SUBSIDENCE: BACKSTRIPPING THE GREAT VALLEY FOREARC, NORTHERN CALIFORNIA

Devon A. Orme[1,*], **Stephan A. Graham**[1], **Kurt N. Constenius**[2], **Allegra Hosford Scheirer**[1]
[1]*Department of Geological Sciences, Stanford University*
[2]*Snowslip Corporation, Tucson, AZ*
[*]dorme@stanford.edu

Introduction

Forearc basins evolve between magmatic arcs and accretionary prisms and are important sediment archives of convergent margins. Forearc basins often contain several kilometers of sedimentary rocks and may be characterized by high magnitude subsidence. However, unlike other types of basins, such as foreland or rift basins (DeCelles and Giles, 1996; Beaumont, 1981; McKenzie, 1978), the fundamental tectonic mechanisms controlling basin subsidence in a forearc basin are poorly understood (Noda, 2016; Xie and Heller, 2009; Angevine et al. 1990). Much of this challenge stems from the majority of modern forearcs being submarine, the investigation of which requires expensive deep-sea coring expeditions. In addition, most forearc basins have limited petroleum potential, typically hosting relatively few reflection seismic surveys. The majority of these basins are highly deformed and significantly eroded (e.g., Kázmér et al. 2003) or removed entirely by subduction erosion processes (Lallemand, 1998). There are, however, some ancient forearcs that are preserved and sub-aerially exposed (e.g., Orme et al. 2014; Trop et al., 2008; Dürr, 1996; Garzanti and Van Haver, 1988; Ingersoll, 1976). Thus, the majority of both ancient and modern forearc basins lack the necessary data for a thorough three-dimensional (3D) subsidence analysis necessary to produce a distinctive and well-understood forearc evolutionary and subsidence history.

The Great Valley forearc in California is a notable exception to many of the challenges to resolving the complex processes active during the life cycle of a forearc basin. Extending for 680 km along the continental margin, it was part of a series of forearc basins that developed from Early Cretaceous to early Cenozoic time as subduction of oceanic crust was accommodated beneath the western margin of North America (Dickinson, 1995; Ingersoll, 1976). The Great Valley forearc was part of an accretionary forearc system (e.g., Clift and Vannucchi, 2004), and developed between the Franciscan subduction complex to the west and the Sierra Nevada magmatic arc to the east (Figure 1). Unlike other ancient convergent margins, such as the Mesozoic Andean margin, drastic changes in the geometry of the subducting plate along western North America did not cause the magmatic arc and forearc system to migrate substantially thorough time. Thus, a thick stratigraphic succession more than 18 km was deposited during the Mesozoic and early Cenozoic (Ingersoll, 1976). Following a change from convergence to transform motion along the Californian margin in the Oligocene, the majority of Great Valley forearc basin was preserved east of the new plate boundary.

The preservation of the Great Valley forearc has led to over 60 years of research devoted to understanding its evolution, as well as the deep-water sedimentologic processes

related to the development of vast petroleum and natural gas reservoirs (e.g., Graham, 1987). Recent advances in detrital-zircon geochronology and provenance analysis have led to new models of sediment dispersal patterns, which link changes in the geometry of the subducting slab to changes in sedimentation in the Great Valley forearc (Sharman et al. 2014; Dumitru et al. 2012; 2015; DeGraff-Surpless et al. 2002). In addition, the availability of high quality proprietary 2D-3D seismic volumes have allowed for subsurface analysis of the stratigraphic architecture of the basin, but with little emphasis on deciphering the mechanisms of basin subsidence. The work of Williams and Graham (2013) and Williams (1997) are notable exceptions. Therefore, despite these efforts, much of the geohistory of the Great Valley forearc remains incompletely understood.

This study seeks to define a holistic model for forearc basin evolution by performing the first 3D tectonic subsidence analysis of the well-preserved Mesozoic-early Cenozoic Great Valley forearc basin in northern California (Figures 1). The objectives of this study are to (1) *use subsurface stratal geometric relationships and spatio-temporal changes in basin fill thickness to determine the primary subsidence mechanisms acting on the Great Valley forearc and (2) use these results to define a framework for interpreting subsidence trends in other ancient and modern forearc basins*. We hypothesize that the shape of a forearc tectonic subsidence curve may be predicted and used to understand spatial and temporal processes driving basin subsidence, *if* detailed basin geometries and paleobathymetric reconstructions are available. Thus, the availability of previously proprietary seismic, borehole, and paleobathymetric datasets allows for thorough evaluation of the three-dimensional structural and stratigraphic architecture of the Great Valley forearc.

Methodology

This research seeks to address the questions presented herein by (A) reconstructing the primary depositional basin geometry by building a 3D basin model, (B) producing a series of isopach maps for the Cretaceous and early Cenozoic, and (C) performing a 3D quantitative subsidence analysis. The study focuses on the Sacramento Basin, an area of about 6000 km^2, bounded on its northern and southern boundaries by the Stockton Arch and Klamath Mountains, respectively (Figure 1).

Reconstruction of Primary Depositional Geometries and Sediment Thickness

This study uses the following three datasets to reconstruct basin geometry and stratigraphic thicknesses: (1) boreholes from the California Division of Oil, Gas, and Geothermal Resources (DOGGR) database, (2) boreholes and 2D multichannel seismic reflection from Williams (1997) and Williams and Graham (2013), and (3) 2D seismic-reflection survey from Constenius et al. (2000). To date, the database consists of 1205 boreholes and 5 2D seismic reflection lines (Figure 3). Borehole penetration of pre-Campanian strata is limited in the Sacramento basin, but we use 145 boreholes to reconstruct the geometry of the Jurassic-Early Cretaceous basement and overlying Lower Cretaceous strata. We chose the tops of 24 horizons based on 1169 resistivity borehole records, with aide from 36 previously interpreted boreholes from Williams (1997). Nineteen maps are presented in this report. Horizon maps for the five paleocanyons are not

included. In addition, we use several east-west trending seismic lines and corresponding velocity surveys from Constenius et al. (2000) to determine the depth to the top of basement, top of the Stony Creek Formation, and the Cretaceous-Paleocene unconformity (Figure 4).

In the Great Valley forearc, stratigraphic interpretation must address the structural overprint of Cenozoic deformation (Williams and Graham, 2013; Constenius et al. 2000). Retro-deforming a seismic grid involves flattening the seismic volume along specific stratigraphic surfaces. This process first converts time-migrated seismic profiles to depth in order to interpret the basin structure with no vertical exaggeration. Following the depth conversion, the seismic profiles are flattened along specific marker horizons interpreted as having near-original horizontality. This analysis allows for identification of the primary geometries in regions of sediment accumulation. In regions where we have a high density of seismic data, flattened seismic reflection data also may be used to construct a series of plan-view thickness isopach maps to study the spatio-temporal changes in sediment thickness (e.g., Posamentier et al. 2007; Scheck and Bayer, 1999). In turn, these maps may be used to produce a regional structural model of the basin fill, which integrates the distribution of Early Cretaceous to Paleocene sediment thicknesses in three-dimension.

Subsidence Analysis: 1D versus 3D

A comprehensive subsidence analysis, first referred to as a *Geohistory Analysis* by Van Hinte (1978), uses the decompaction of stratigraphic units to reconstruct their correct thicknesses at the time of interest. To gain insight into subsidence rates and tectonically driven subsidence, a backstripping analysis is used to differentiate between subsidence due to sediment and water loading versus tectonic subsidence. Assuming Airy isostasy, the 1D backstripping technique involves removing successively older layers and correcting the thickness of deeper layers for sediment compaction, paleobathymetric changes and eustatic sea level fluctuations. In turn, subsidence due to sediment and water loading is removed to calculate the portion of tectonically driven subsidence (Y) using the "backstripping equation":

$$Y = W_d + S^* \left[\frac{(\rho_m - \rho_s)}{(\rho_m - \rho_w)}\right] - \Delta_{sl} \frac{\rho_m}{(\rho_m - \rho_w)}$$

where the first term is water depth (W_d), the second term is sediment loading (S^* is decompacted sediment thickness and ρ_m, ρ_s and ρ_w are mantle, sediment and water densities), and the third term is a sea-level loading term (Δ_{sl} is the height of sea level at a specific time interval) (Bond and Kominz, 1984). 2D or 3D backstripping involves a similar technique, but includes a flexural component to address the effects of lateral differential loading by distributing isostatic loads regionally (Watts et al. 1982; Norris and Kusznir, 1993).

To perform a 3D flexural-isostatic backstripping analysis, we also need to create a series of lithologic and paleobathymetric maps, two key input parameters for our model. Lithologic percentages for each genetically meaningful stratigraphic package are determined from electric logs and porosity-depth relationships (e.g., Zieglar and Spotts, 1978) and used to determine decompacted sediment thicknesses. We use biostratigraphic

age control and paleobathymetric constraints from Williams (1997) and several newly obtained paleontological reports from the California core repository to construct a series of digital paleobathymetric maps from the Tithonian through the Miocene. Eustatic sea level corrections follow the "long-term" eustatic sea level curve of Miller et al. (2011). An initial set 1D backstripping calculations are performed on 9 outcrop and borehole datasets using the *PetroMod* geohistory program as a quality control check on the model. The final product will be a series of 3D tectonic subsidence maps from the Tithonian to the present (145-0 Ma).

Basin model and results

The first component of our basin model is a series of horizon maps from the top of Tithonian (145 Ma) to the top of the basin-wide Miocene unconformity (13 Ma) (Figure 5). Horizon maps are shown in feet to be consistent with the resistivity logs from which they were derived. Crystalline basement extends continuously from the Sierra Nevada to the outcrop belt exposed in the Coast Ranges along the western margin of the basin (Figure 6). The depth to basement increases from east to west across the basin with a broad "shelf-like" geometry east of the longitude of Sacramento, before dipping off sharply to the west to a maximum depth of ~ 11,582 m (38,000 ft), east of the town of Williams (Figure 5, 6). This sharp increase in the depth to basement is also observed in seismic line AYD-3 (Figure 4). There are few basement-penetrating boreholes in the western parts of the basin, but our interpolation from the few available is consistent with a previous study for the southern part of the Sacramento basin and northern San Joaquin basin (Wentworth, 1995). The preservation of the Jurassic-Lower Cretaceous strata (Stony Creek and Lodoga Formations) is limited to the western part of the basin and primarily found in outcrop (Figure 5). In the subsurface, these units are found west of the Humble Michael borehole and in cross-section, seismic line AYD-3 shows Jurassic-lower Cretaceous strata parallel to sub-parallel with basement.

The majority of the stratigraphic thickness of the Great Valley accumulated during the Late Cretaceous between ~ 90 and 65 Ma; the remaining 16 horizon maps document deposition during this time period (Figure 5). The horizon maps for the Venado, Yolo and Sites Formations (Turonian-early Coniacian) are spatially limited to the northwest part of the basin, primarily reflecting the lack of boreholes penetrating these units in the south. Nevertheless, the general depositional pattern shows southward deepening. The Guinda through Mokelumne Formation (late Coniacian-Maastrichtian) maps show the development of an elongate, narrow (< 25 km) trough that migrated southward during this time period. Isopach maps for the Dobbins, Forbes, Sacramento and Winters are shown in Figure 7. Between the late Coniacian and Maastrichtian, >2600 m of sediments accumulated within this depositional center. Notably, the Winters, Starkey and Mokelumne Formations are found only in the southern part of the basin; coeval stratigraphy is absent in the north where Eocene units are in unconformable contact with Campanian Kione-Sacramento stratigraphy.

The Cenozoic basin fill is challenging to reconstruct owing to local paleocanyon and basin-wide unconformities. From the Ypresian (55 Ma) to the Miocene Unconformity (13

Ma), ~ 1981 m of stratigraphy was deposited, primarily filling the Eocene Princeton, Markley, Meganos, and Martinez paleocanyons. The primary depositional center remained in the south-southwest area of the basin. The middle Miocene is marked by a basin-wide unconformity dated at ~ 13 Ma; less than <1 km of Neogene sediment exists above this horizon.

Paleobathymetric maps were constructed for each horizon interval from the Tithonian to the Miocene unconformity. Middle Turonian to middle Campanian maps were digitized from Williams (1997), whereas Early Cretaceous and middle Campanian-Miocene maps are a new contribution. Figure 8 highlights the variability of basin bathymetry from the middle Turonian to latest Campanian. Paleobathymetric constraints for the deposition of the Stony Creek Formation are consistently lower bathyal to abyssal, as evidenced by genera such as *Trochammina*, *Saracanaria*, and *Cribrostomoides*. By Middle Turonian, it appears that the bathyal and abyssal depths were concentrated along the western margin of the basin. From early Coniacian to early Santonian, the position of the neritic-bathyal boundary remained relatively constant whereas the latest Santonian saw an increase in water depth. By the middle Campanian water depths had significantly decreased and the majority of basin deposition was <200 m. By latest Campanian, the northern part of the basin was subaerially exposed, whereas local bathymetry in the southern part of the basin was between 1500-200 m water depth. Cenozoic water depths were primarily <30 m, with the exception of four transgressive-regressive cycles which locally saw bathyal conditions during infilling of incised canyons (e.g., Almgren, 1984).

Subsidence Analysis

A series of 1D Airy-isostatic subsidence curves, consisting of 1 outcrop and 8 borehole stratigraphic sections, are plotted from north to south in Figure 9. Dry Creek (A), American Hunter Alvarez (B), Humble Michael (C), Sunray M-C Whyler-Walcott (D), Humble Capital #1 (E), Glide Court 65-10 (G), and Ojai Ranch (I) extend to basement and subsidence is calculated from ~145 Ma to 65 Ma. By contrast, the stratigraphic information available for Ridge Cutt Farms (F) and RGVU (H) extend from 78-65 Ma and 65-0 Ma, respectively.

The Late Jurassic-Early Cretaceous subsidence trends are difficult to constrain owing to the lack of preservation of strata of this age and poor paleobathymetric constraints between 140 and 90 Ma. Nevertheless, a backstripping analysis for this period was conducted on the Dry Creek outcrop and the American Hunter Alvarez and Humble Michael wells where Stony Creek and Lodoga stratigraphy is preserved. Paleowater depth constraints from the basal contact with basement are used and held constant, as sidewall paleobathymetric samples are not available for a more detailed reconstruction. This analysis shows total subsidence on the order of 1000 m to 5000 m for American Hunter Alvarez and Humble Michael, and ~ 5000 m of subsidence for Dry Creek. Tectonically driven subsidence is 500 m and 1000 m for AHA and HM, respectively, and 2000 m for Dry Creek. For the remaining boreholes which penetrate basement, the dashed line for this time period is inferred; each of these boreholes show a period of uplift from 100-95 Ma.
The Cenomanian to Maastrichtian is the best constrained time period for reconstructing subsidence histories in the Sacramento basin. From the Cenomanian to Santonian, a series

of rapid subsidence and uplift events are observed (Figure 9). In the central to north area a period of rapid subsidence starts at ~ 93 Ma, followed by a period of uplift at ~ 85 Ma. This period of rapid subsidence is younger (~85-80 Ma) in the sections farther east, Glide Court 65-10, Ridge Cutt Farms and Ojai Ranch. From 92-90 Ma, Glide Court 65-10 shows a period of rapid subsidence and uplift, prior to the seemingly episodic subsidence and uplift patterns observed basin wide between 93 and 80 Ma.

From the Campanian to Maastrichtian (83.6-65 Ma), rates of tectonic subsidence were low. During deposition of the Forbes Shale (~82-78 Ma), basin wide uplift is observed. Following this, sections in the central to southern parts of the basin (Humble Capital #1, Glide Court 65-10 and Ojai Ranch) show a period of renewed tectonic subsidence on the order of 250-500 m during deposition of the Sacramento Shale (~78-77 Ma). By 77 Ma, tectonic subsidence ceases throughout the basin for the remainder of the Cretaceous.

As mentioned previously, the basin scale Cenozoic subsidence history is difficult to determine owing to numerous unconformities, primarily resulting from paleocanyon incision and infilling. However, in the southern Sacramento basin, the majority of Cenozoic stratigraphy is preserved and there are strong paleobathymetric estimates for paleocanyon sedimentary fill. Borehole Ojai Ranch, located just south of the limit of Markley paleocanyon, shows a period of limited tectonic subsidence (<300 m) from 65-13 Ma, with coeval total basin subsidence ~ 900 m. Borehole RGVU records deposition from the infilling of the Meganos canyon by the Capay Shale (~56 Ma) to Neogene sedimentation. Similar to Ojai Ranch, a period of limited tectonic subsidence and uplift is seen between 56-53 and 53-49 Ma, respectively; the component of tectonic subsidence is <500 m.

Summary and Conclusions

This work will produce the first 3D basin model for the Great Valley forearc and first 3D subsidence analysis for an ancient forearc globally. Construction of the horizon stacks (Figure 5), age assignments, facies maps, and paleowater depth maps (Figure 8) is complete. As a quality control on the data, preliminary isopach maps (Figure 7) were made and a 1D subsidence analysis was performed (Figure 9). The assembly of this data into *PetroMod* and building of the model is in progress. The following briefly describes some of the findings from construction of the horizon stacks and 1D backstripping analysis presented in this report.

Basin Model

The basement map constructed for the Sacramento basin is consistent with the structural trends observed in the basement map of Wentworth (1995) for the San Joaquin basin. In cross-section, seismic line AYD-3 shows Jurassic-Lower Cretaceous strata parallel to sub-parallel to basement, suggesting deposition was primarily on a relatively planar basement surface. Williams and Graham (2013) note that the angularity of onlap suggest that the average slope of the unconformity at the time of deposition was 3-5 degrees, similar to modern continental slopes.

The horizon stacks show a southward migration of the primary depositional center along the partially preserved western limit and central part of the basin, consistent with outcrop stratigraphy which shows a southward deepening from upper slope mudstones through slopes channels to thick-bedded incised mid-fan and unconfined fan lobe deposits during the Turonian to early Campanian (Ingersoll, 1976; Dailey, 1973; Lowe, 2000). Geometric relationships along the east side of the basin are difficult to extract at the scale with which these horizons are plotted in Figure 5, but paleobathymetric profiles from the middle Turonian to Santonian show an overall pattern of eastward transgression. Previous work on subsurface stratigraphy along the eastern margin of the basin shows details a series of transgressive sequences with deposition occurring in the sub-littoral to outer neritic zones (e.g., Haggart and Ward, 1986). The horizon and paleobathymetric maps also show that the northern Sacramento basin filled by lower Campanian time, whereas the southern part of the basin remained a primarily a marine to deltaic depositional environment until the latest Maastrichtian. Lacking in our current model are a series of faults that slipped during the Late Cretaceous and localized deposition of units such as the Winters sandstone (Cherven, 1983; Moxon, 1990). Incorporation of these faults and Late Cretaceous deformation and uplift of the now western margin of the basin will be considered when constructing the basin model. Similarly, erosion and infilling of paleocanyons will also be included in the model.

Subsidence

The 1D subsidence analysis captures basin-wide trends in subsidence, but also highlights local variability. Initial Early Cretaceous subsidence depths in the northern part of the Sacramento basin were variable, with the Dry Creek outcrop recording ~11,000 m of total subsidence versus the American Hunter Alvarez and Humble Michael recording 4000-7000 m of total subsidence. This local variability reflects differences in the underlying basement, whereby the Dry Creek outcrop, which overlies Klamath basement, likely experienced rapid subsidence driven by fault-bounded blocks active during the Early Cretaceous (Moxon, 1990). Interestingly, the period of rapid tectonically driven uplift between 100 and 95 Ma, is observed in all three regions, suggesting, by that time, a more basin-wide mechanism drove uplift.

Along the length of the basin, the Cenomanian to Maastrichtian is characterized by episodic tectonically-driven subsidence and uplift events. In the central to northern parts of the basin, these periods are synchronous. Williams (1997) suggested the episodic synchroneity to reflect flexurally-driven subsidence, similar to foreland basins, but acknowledge the nature of the load is unclear. In the eastern part of the basin, the periods of rapid subsidence and uplift are locally synchronous, but younger than the northern sections. Although the Sierra Nevada magmatic arc imparted a significant load on the continental margin during this time period, the temporal eastward migration in the timing of periods of subsidence is inconsistent with the flexural load being located to the west. In contrast, Williams and Graham (2013) suggest that western portion of the basin experienced flexural loading from arcward thrusting of the accretionary prism. Harrison et al. (2007) also interpreted arcward thrusting of the western basin margin from a reflection seismic survey at the latitude of Merced. The preliminary 1D analysis supports the interpretation of a flexural load controlling the periodicity observed during the Late

Cretaceous, but the origin of the flexural load remains unclear. Furthermore, there is once again local variability that suggests that a second-order mechanism (e.g., local faulting, local paleobathymetric changes) may be responsible for the local variability observed.

Thermal, isostatic, and flexural forces drive subsidence in sedimentary basins. Specific processes, such as the growth of a topographic load or negative buoyancy of underlying oceanic crust, result in unique shapes of tectonic subsidence curves. For example, foreland basin systems, which develop under the influence of a thrust belt load, record the migration of a flexural "wave", producing an overall upward convex subsidence curve. Relative to other sedimentary basins, subsidence curves from forearc basins vary significantly in their shape. Loading from an accretionary subduction complex, magmatic arc and sediment accumulation, thermal relaxation due to conductive cooling of forearc basement crust and magmatic arc migration, and changes in the subduction angle all likely influence forearc basin subsidence. These processes may vary spatially and temporally across the basin, causing their unique subsidence signals to conflict with each other. These interference signals might result in a non-unique subsidence curve when compared to other sedimentary basins. The 1D analysis presented here emphasizes this variability and highlights how interpretation of a 1D subsidence curve limits our ability to decipher between mechanisms driving basin subsidence.

A 3D subsidence analysis applies a flexural component, rather than local Airy isostasy, to address the effects of lateral differential loading (Watts et al., 1982). Application of a flexural model is only possible in basins with good paleobathymetric control, such as the Great Valley forearc. However, the Sacramento basin is not without its complications. Specifically, assumptions regarding the degree of sediment loading imparted by the eroded stratigraphy along the western half of the basin must be made. In addition, the flexural strength (i.e. flexural rigidity, D and elastic thickness, T_e) of the lithosphere must vary according to different lithologies of the underlying basement (e.g., granite versus ophiolite). Although PetroMod will be used to construct the model, the 3D flexural subsidence analysis likely will be done through an in-house MATLAB code currently in development. Following this study, the results will serve as the basis for interpreting the mechanisms driving subsidence in forearcs globally. In addition, it is our hope that this 3D basin model may form the foundation for future petroleum system modeling that will incorporate petroleum generation, fluid analysis, and petroleum migration.

References

Almgren, A.A., 1984, Timing of Tertiary Submarine Canyons and Marine Cycles of Deposition in the Southern Sacramento Valley, California, in A.A. Almgren and P.D. Hacker, eds. Paleogene Submarine Canyons of the Sacramento Valley, California: Pacific Section, American Association of Petroleum Geologists, p. 1-16.

Angevine, C.L., Heller, P.L., and Paola, C., 1990, Quantitative sedimentary basin modeling: American Association of Petroleum Geologists Short Course Note Series 32, 247 p.

Beaumont, C., 1981, Foreland Basins: Geophysical Journal of the Royal Astronomical Society, v. 65, p. 291-329.

Bond, G.C., and Kominz, M.A., 1984, Construction of tectonic subsidence curves for the early Paleozoic miogeocline, southern Canadian Rocky Mountains: Implications for subsidence mechanisms, age of breakup, and crustal thinning, Geological Society of America Bulletin, v. 95, p 155–173.

Clift, P.D. and Vannucchi, P., 2004, Controls on tectonic accretion versus erosion in subduction zones: Implications for the origin and recycling of the continental crust: Reviews in Geophysics, v. 42, RG2001.

Cherven, V.B., 1983, Stratigraphy, facies, and depositional provinces of the Middle Eocene Domengine Formation, southern Sacramento basin: Pacific Section Society of Economic Paleontologists and Mineralogists, Field Trip Guidebook, p. 43-54.

Constenius, K.N., Johnson, R.A., Dickinson, W.R., and Williams, T.A., 2000, Tectonic evolution of the Jurassic–Cretaceous Great Valley forearc, California: Implications for the Franciscan thrust-wedge hypothesis: Geological Society of America Bulletin, v. 112, p. 1703–1723.

DeCelles, P.G., and Giles, K.A., 1996, Foreland basin systems: Basin Research, v. 8, p. 105–123.

DeGraaff-Surpless, K., Graham, S.A., Wooden, J.L., and McWilliams, M.O., 2002, Detrital zircon provenance analysis of the Great Valley Group, California: Evolution of an arc-forearc system: Geological Society of America Bulletin, v. 114, p. 1564–1580.

Dickinson, W.R., 1995, Forearc basins, *in* Busby, C.J., and Ingersoll, R.V., eds., Tectonics of sedimentary basins: Cambridge, Massachusetts, Blackwell Science, p. 221–261.

Dickinson, W.R., Armin, R.A., Beckvar, N., Goodlin, T.C., Janecke, S.U., Mark, R.A., Norris, R.D., Radel, G., and Wortman, A.A., 1987, Geohistory analysis of rates of sediment accumulation and subsidence for selected California basins, *in* Ingersoll, R.V., and Ernst, W.G., eds., Cenozoic basin development of coastal California: Englewood Cliffs, New Jersey, Prentice-Hall, 496 p.

Dumitru, T.A., Elder, W.P., Hourigan, J.K., Chapman, A.D., Graham, S.A., Wakabayashi, J., 2015, Four Cordilleran paleorivers that connected Sevier thrust zones in Idaho to depocenters in California, Washington, Wyoming, and indirectly, Alaska: Geology, v. 44, p. 75-78.

Dumitru, T.A., Ernst, W.G., Wright, J.E., Wooden, J.L., Wells, R.E., Farmer, L.P., Kent, A.J.R., and Graham, S.A., 2012, Eocene extension in Idaho generated massive sediment floods into the Franciscan trench and into the Tyee, Great Valley, and Green River basins: Geology, v. 41, p. 187-190.

Dürr, S.B.,1996, Provenance of Xigaze forearc basin clastic rocks (Cretaceous, south Tibet).

Geological Society of America Bulletin, v. 108, p. 669-684.

Garzanti, E. and Van Haver, T., 1988, The Indus clastics: Forearc basin sedimentation in the Ladakh Himalaya (India): Sedimentary Geology, v. 59, p. 237-249.

Graham, S.A., 1987, Tectonic controls on petroleum occurrence in central California, *in* Ingersoll, R.V., and Ernst, W.G., eds., Cenozoic basin development of coastal California: Englewood Cliffs, New Jersey, Prentice-Hall, 496 p.

Graham, S.A., 1976, Tertiary sedimentary tectonics of the central Salinian block of California [Ph.D. thesis]: Stanford University, 510 p.

Haggart, J.W. and Ward, P.D, 1984, Late Cretaceous (Santonian-Campanian) stratigraphy of the northern Sacramento Valley, California: Geological Society of America Bulletin, v. 95, p. 618-627.

Harrison, D.H., Jones, S.D., Harrison, P.J., Armentrout, J.M., Suek, D.H., Codding, D.B., 2007, Repeated cycles of progradation and incision of Upper Cretaceous shelf-margin deltas, northern San Joaquin Basin, California: American Association of Petroleum Geologists Annual Meeting, Long Beach, California, 1-3 April.

Hosford Scheirer, A., Tennyson, M.E., Magoon, L.B., Charpentier, R.R. Cook, T.A., Klett, T.R., Pollastro, R.M., Schenk, C.J., 2007, Assessment of Undiscovered Natural Gas Resources of the Sacramento Basin Province of California, 2006: United States Geological Survey, No. 2007-3014.

Ingersoll, R.V., 1976, Evolution of the Late Cretaceous forearc basin of northern and central California [Ph.D. thesis]: Stanford University, 200 p.

Kázmér, M., Dunkl, I., Frisch, W., Kuhlemann, J., Ozsvárt, P., 2003, The Palaeogene forearc basin of the Eastern Alps and Western Carpathians: subduction erosion and basin evolution: Journal of the Geological Society of London, v. 160, p. 413-428.

Lallemand, S.E., 1998, Possible interaction between mantle dynamics and high rates of arc consumption by subduction processes in Circum-Pacific area, *in* Flower, M.F.J., et al., eds., Mantle dynamics and plate interactions in east Asia: American Geophysical Union Geodynamic Series, v. 27, p. 1-9.

McKenzie, D.P., 1978, Some remarks on the development of sedimentary basins: Earth and Planetary Science Letters, v. 40, p. 25-31.

Moxon, I.W., and Graham, S.A., 1987, History and controls of subsidence in the Late Cretaceous-Tertiary Great Valley forearc basin, California: Geology, v. 15, p. 626–629.

Moxon, I.W., 1990, Stratigraphic and structural architecture of the San Joaquin-Sacramento basin [Ph.D. thesis]: Stanford University, 371 pp.

Noda, A., 2016, Forearc basins: Types, geometries, and relationships to subduction zone dynamics: Geological Society of America Bulletin, v. 128, p. 879–895.

Norris, S., and Kusnir, J.K., 1993, 3-D reverse modeling of post-rift extensional basins: Terra Nova, v. 5, p. 173–174.

Orme, D.A., Carrapa, B., Kapp, P., 2014, Sedimentology, Provenance, and Geochronology of the Upper Cretaceous-Lower Eocene Western Xigaze forearc basin, southern Tibet: Basin Research, v. 27, p. 387-411.

Posamentier, H.W., Davies, R.J., Cartwright, J.A., Wood, L., 2007, Seismic geomorphology—an overview: Geological Society of London, Special Publications, v. 277, p. 1-14.

Sharman, G.R., Graham, S.A., Grove, M., Kimbrough, D.L., Wright, J.E., 2014, Detrital zircon provenance of the late Cretaceous-Eocene California forearc: Influence of Laramide low-angle subduction on sediment dispersal and paleogeography: Geological Society of America Bulletin, v. 127, p. 38-60.

Scheck, M., and Bayer, U., 1999, Evolution of the Northeast German Basin: Inferences from a 3D structural model and subsidence analysis: Tectonophysics, v. 313, p. 145-169.

Surpless, K.D., Graham, S.A., Covault, J.A., Wooden, J.L., 2010, Does the Great Valley Group contain Jurassic strata? Reevaluation of the age and early evolution of a classic forearc basin: Geology, v. 34, p. 21-24.

Trop, J.M., 2008, Latest Cretaceous forearc basin development along an accretionary convergent margin: South-central Alaska: Geological Society of America Bulletin, v. 120, p. 207–224.

Van Hinte, J.E., 1978, Geohistory analysis: application of micropalaeontology in exploration geology: American Association of Petroleum Geologists Bulletin, v. 62, p. 201-222.

Watts, A.B., Karner, G.D., and Steckler, M.S., 1982, Lithospheric flexure and the evolution of sedimentary basins: Philosophical Transactions of the Royal Society, London, v. 305, p. 249-281.

Wentworth, C.M., Fisher, G.R., Levine, P., Jachens, R.C., 1995, The surface of crystalline basement, Great Valley and Sierra Nevada, California: A Digital Map Database: United States Geological Survey, Open-File Report 95-96.

Williams, T.A., Graham, S.A., and Constenius, K.N., 1998, Recognition of a Santonian submarine canyon, Great Valley Group, Sacramento basin, California: Implications for petroleum exploration and sequence stratigraphy of deep-marine strata: American Association of Petroleum Geologists Bulletin, v. 82, p. 1575-1595.

Williams, T.A. and Graham, S.A., 2013, Controls on forearc basin architecture from seismic and sequence stratigraphy of the Upper Cretaceous Great Valley Group, central Sacramento Basin, California, International Geology Review, v. 55, p. 2030-2059.

Williams, T.A., 1997, Basin-fill architecture and forearc tectonics, Cretaceous Great Valley Group, Sacramento basin, northern California [Ph.D. thesis]: Stanford University, 412 p.

Xie, X., and Heller, P., 2009, Plate tectonics and basin subsidence history: Geological Society of America Bulletin, v. 121, p. 55–64.

Zieglar, D.L., and Spotts, J.H., 1978, Reservoir and source-bed history of Great Valley, California: American Association of Petroleum Geologists Bulletin, v. 62, p. 813-826.

Figures

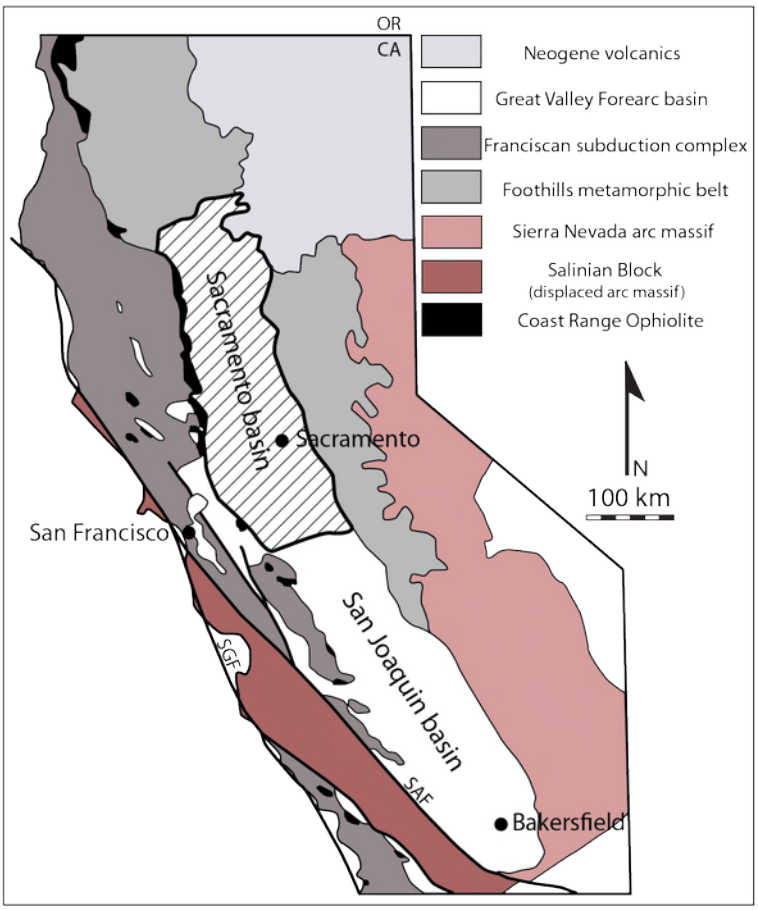

Figure 1: Generalized geologic map of California after Williams and Graham (2013) and Dickinson (1995). Sacramento basin study area outlined by the striped pattern.

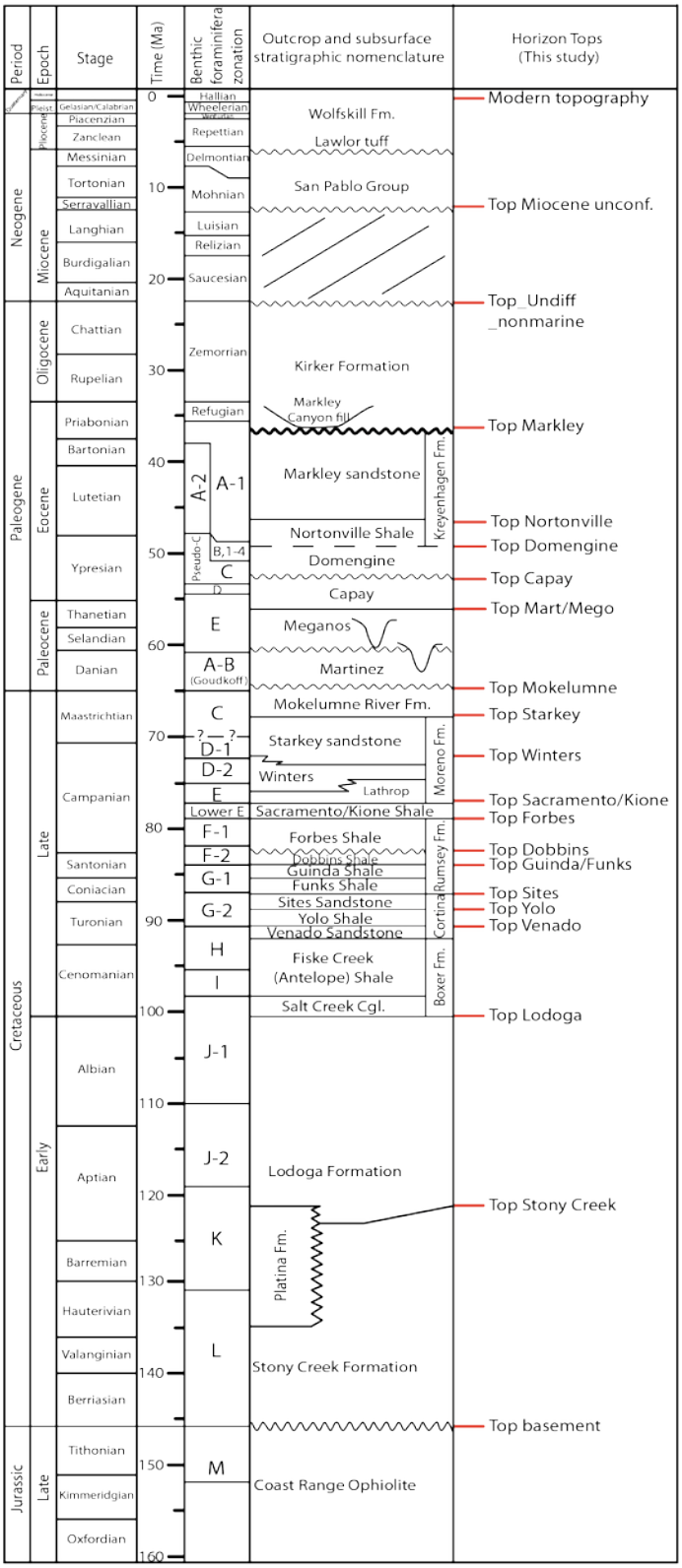

Figure 2: Late Jurassic to Quaternary stratigraphy of the Sacramento basin after Williams and Graham (2013), Surpless et al. (2010), and Almgren (1984). Unconformities marked by wavy line. Periods of hiatus or erosion shown in hatched pattern.

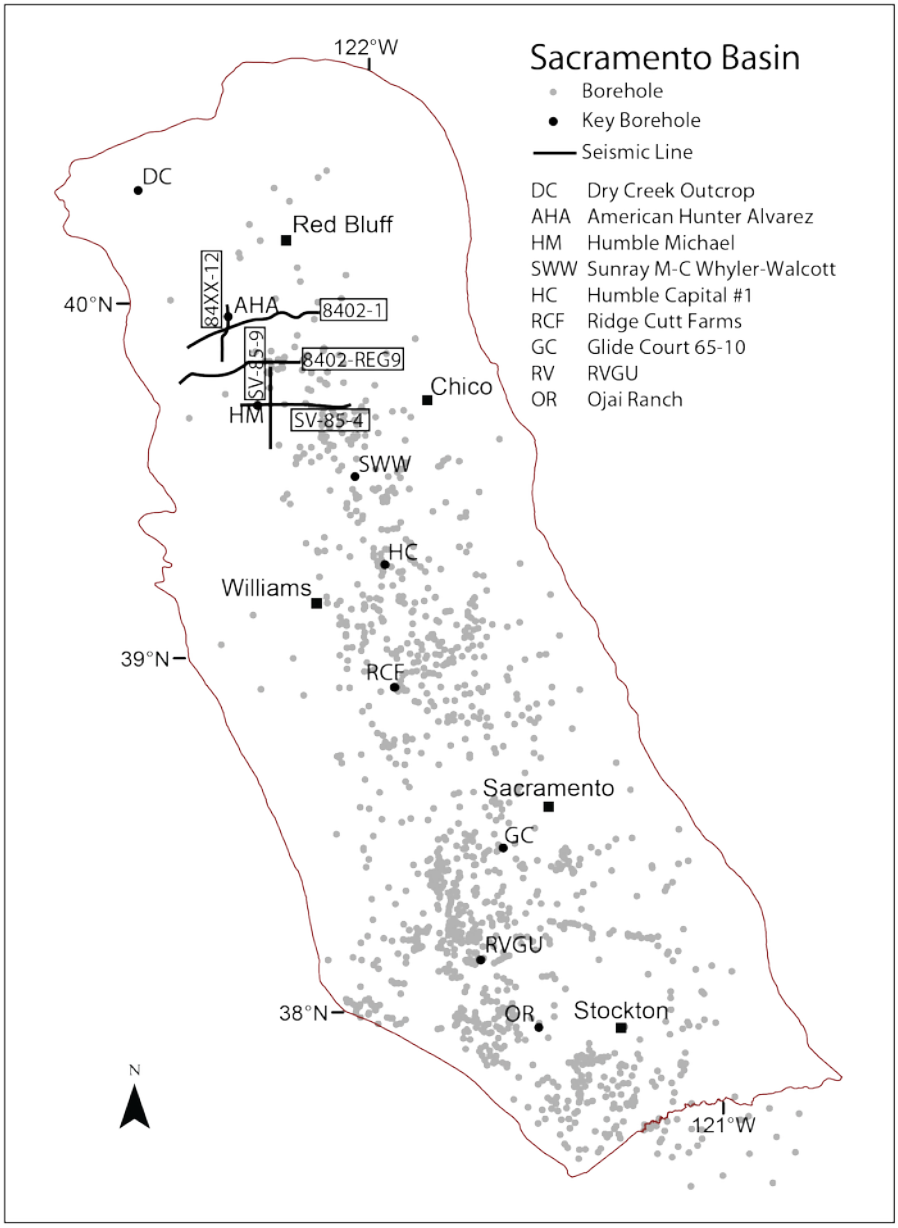

Figure 3: Outlined of the Sacramento basin with the location of boreholes (n =1205) and seismic reflection lines (n = 5) used in this study.

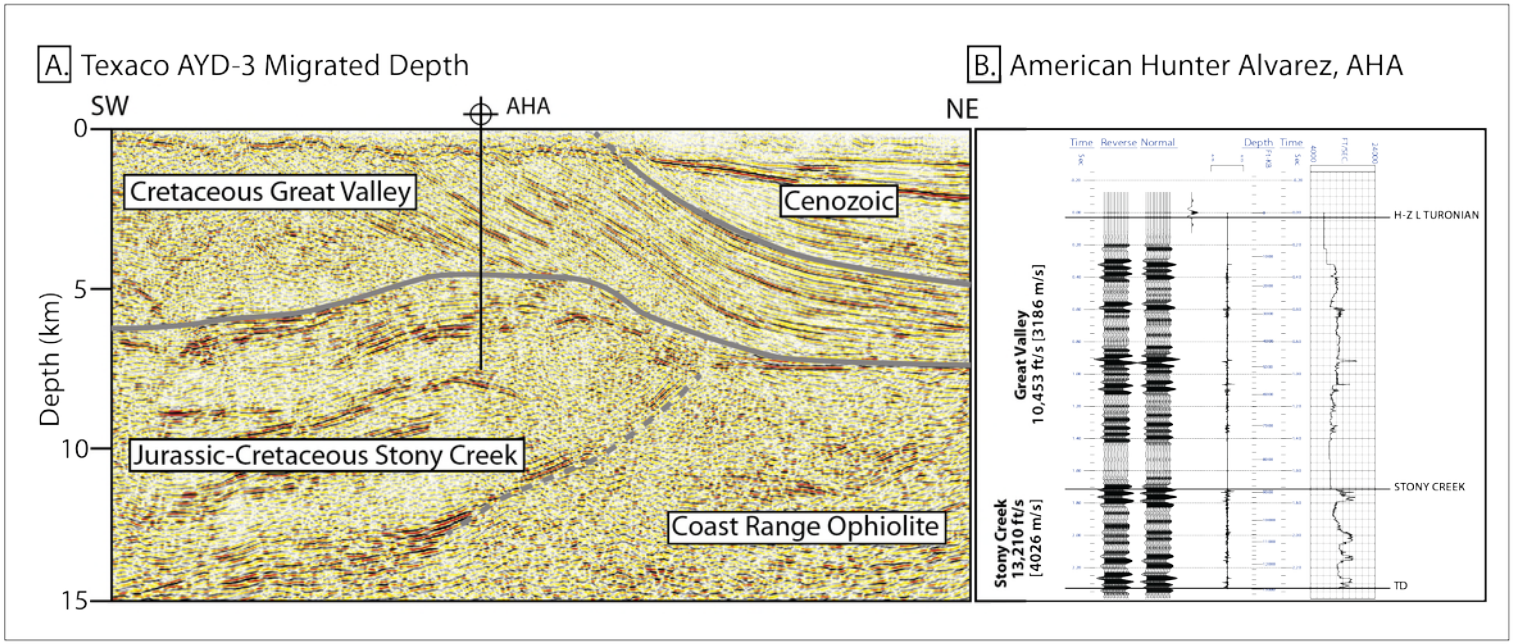

Figure 4: (A) Seismic reflection line AYD-3 showing the contact between the Coast Range Ophiolite, Stony Creek Formation, Cretaceous Great Valley group, and Cenozoic stratigraphy. Reflectors between the Stony Creek and basement are sub-parallel to parallel. (B) Velocity Survey from borehole American Hunter Alvarez.

Figure 5 (next page): Horizon maps showing the depth to the top of 19 stratigraphic surfaces used in the study; paleocanyons and modern topography are not shown. Basement, Stony Creek Formation, and Lodoga Formation are shown in a different scale (top right). The horizons show the overall southward deepening of the basin through time. White regions represent areas where specific formations were not deposited or subsequently have been eroded.

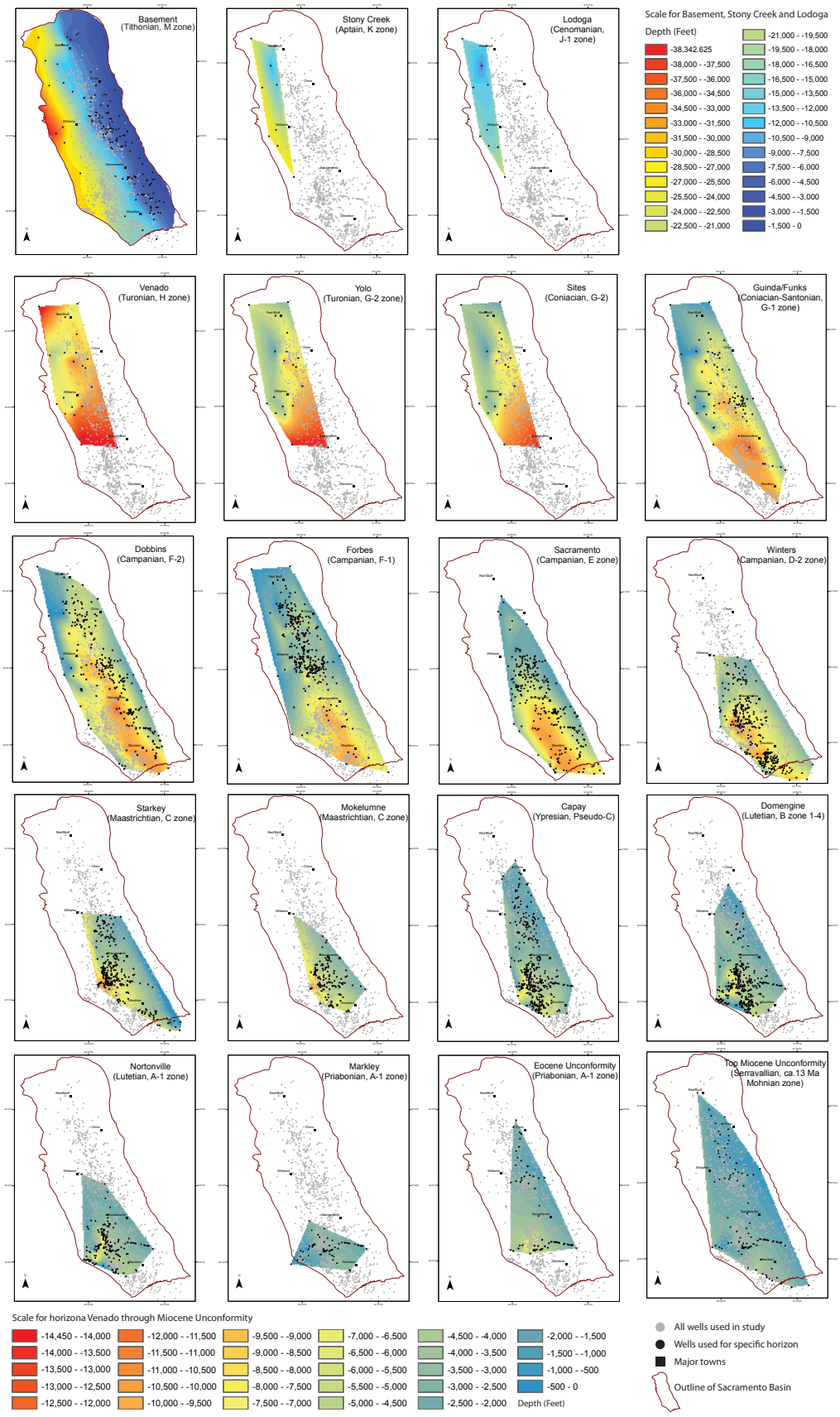
Basement (Tithonian, M zone)
Stony Creek (Aptain, K zone)
Lodoga (Cenomanian, J-1 zone)
Scale for Basement, Stony Creek and Lodoga
Depth (Feet)
-38,342.625
-38,000 - -37,500
-37,500 - -36,000
-36,000 - -34,500
-34,500 - -33,000
-33,000 - -31,500
-31,500 - -30,000
-30,000 - -28,500
-28,500 - -27,000
-27,000 - -25,500
-25,500 - -24,000
-24,000 - -22,500
-22,500 - -21,000
-21,000 - -19,500
-19,500 - -18,000
-18,000 - -16,500
-16,500 - -15,000
-15,000 - -13,500
-13,500 - -12,000
-12,000 - -10,500
-10,500 - -9,000
-9,000 - -7,500
-7,500 - -6,000
-6,000 - -4,500
-4,500 - -3,000
-3,000 - -1,500
-1,500 - 0
Venado (Turonian, H zone)
Yolo (Turonian, G-2 zone)
Sites (Coniacian, G-2)
Guinda/Funks (Coniacian-Santonian, G-1 zone)
Dobbins (Campanian, F-2)
Forbes (Campanian, F-1)
Sacramento (Campanian, E zone)
Winters (Campanian, D-2 zone)
Starkey (Maastrichtian, C zone)
Mokelumne (Maastrichtian, C zone)
Capay (Ypresian, Pseudo-C)
Domengine (Lutetian, B zone 1-4)
Nortonville (Lutetian, A-1 zone)
Markley (Priabonian, A-1 zone)
Eocene Unconformity (Priabonian, A-1 zone)
Top Miocene Unconformity (Serravallian, ca.13 Ma Mohnian zone)
Scale for horizona Venado through Miocene Unconformity
-14,450 - -14,000
-14,000 - -13,500
-13,500 - -13,000
-13,000 - -12,500
-12,500 - -12,000
-12,000 - -11,500
-11,500 - -11,000
-11,000 - -10,500
-10,500 - -10,000
-10,000 - -9,500
-9,500 - -9,000
-9,000 - -8,500
-8,500 - -8,000
-8,000 - -7,500
-7,500 - -7,000
-7,000 - -6,500
-6,500 - -6,000
-6,000 - -5,500
-5,500 - -5,000
-5,000 - -4,500
-4,500 - -4,000
-4,000 - -3,500
-3,500 - -3,000
-3,000 - -2,500
-2,500 - -2,000
-2,000 - -1,500
-1,500 - -1,000
-1,000 - -500
-500 - 0
Depth (Feet)
All wells used in study
Wells used for specific horizon
Major towns
Outline of Sacramento Basin

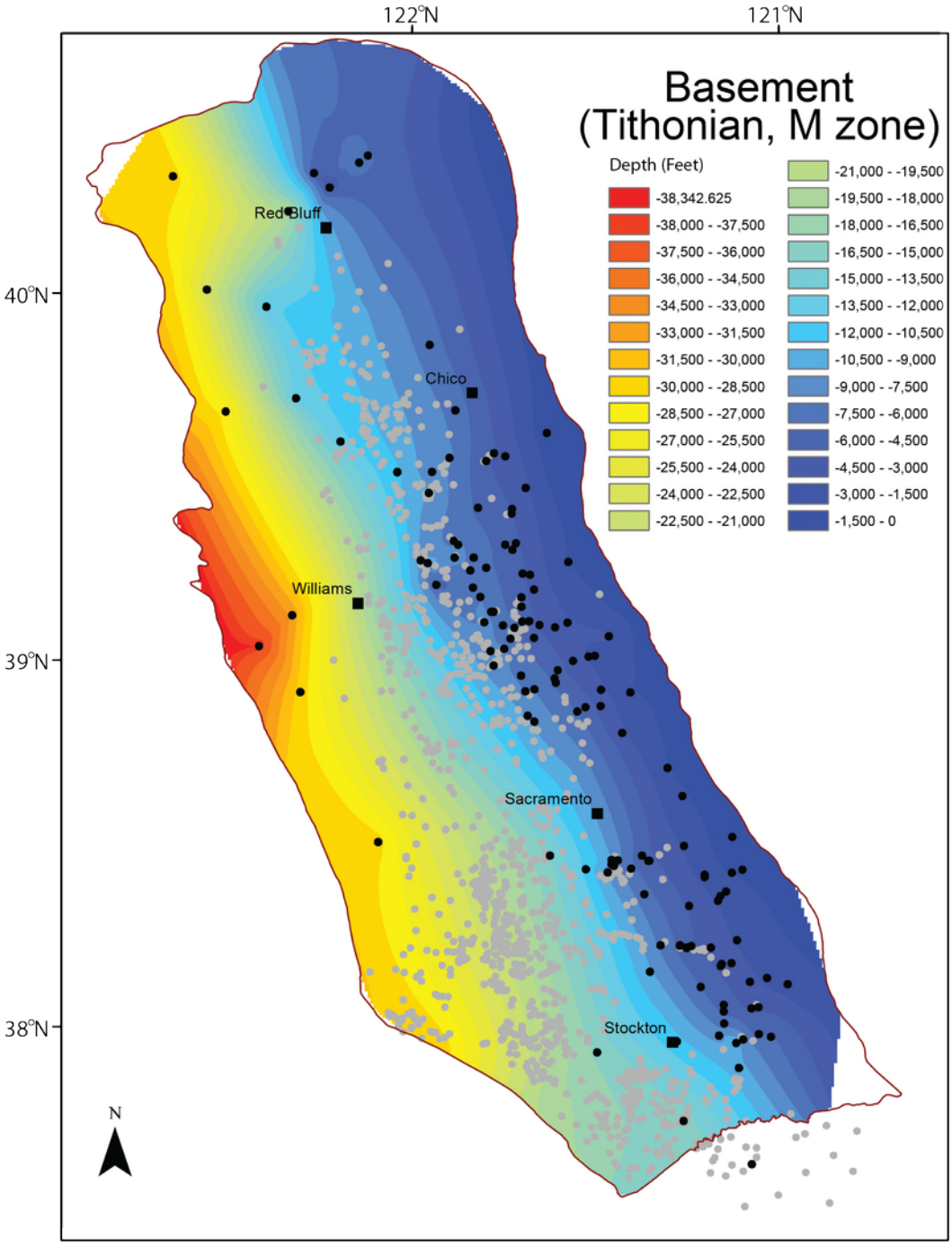

Figure 6: Depth to top of basement constructed from 145 boreholes abd 7 outcrop localities. Basement reaches a maximum depth of ~ 38,000 ft (11,582 m) west of the town of Williams.

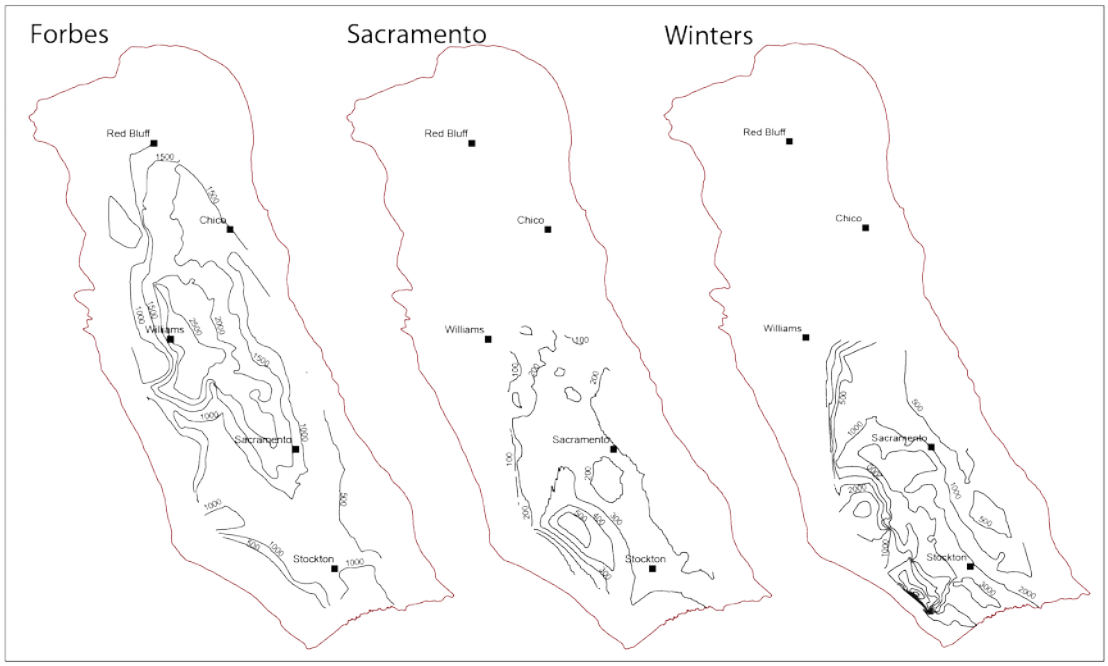

Figure 7: Isopach maps for the Forbes, Sacramento, and Winters Formations showing the southward migration of the depositional center between ~78-73 Ma. The northern Sacramento basin filled by late Campanian.

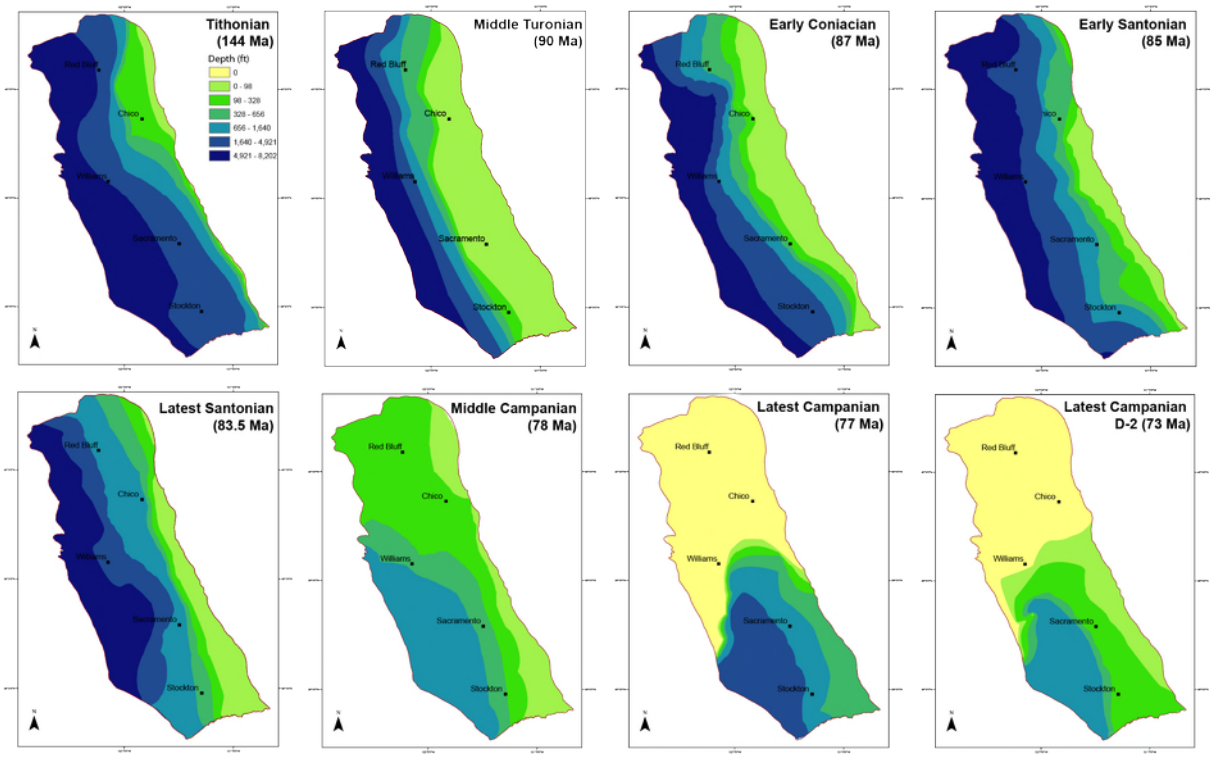

Figure 8: Paleowater depth maps for the Tithonian (basement) and Middle Turonian-Latest Campanian. An overall transgression is observed between ~ 90 to 83 Ma, with upper bathyal to abyssal water depths in the central part of the basin and a neritic environment to the east. The northern Sacramento basin was subaerial by lower Campanian time, whereas the southern part of the basin remained a primarily a middle neritic to middle bathyal until the latest Maastrichtian.

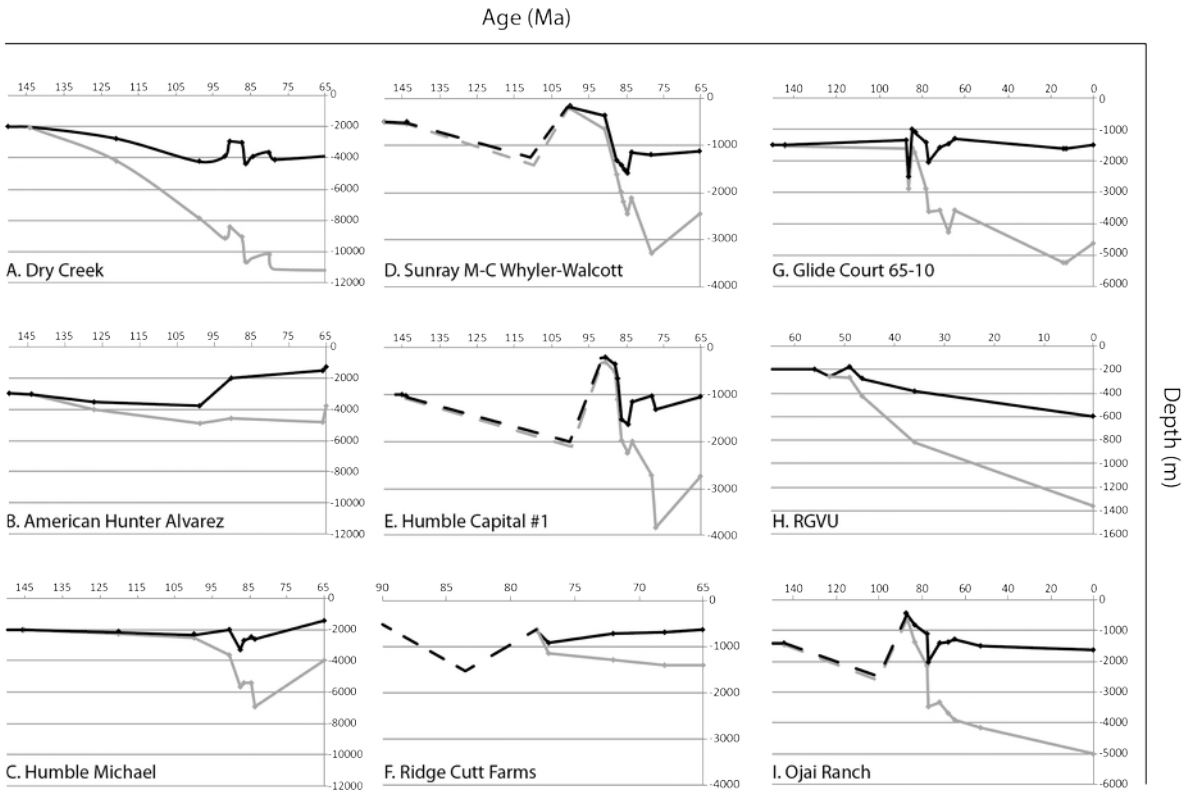

Figure 9: Tectonic (black line) and total (grey line) subsidence curves for 8 boreholes and 1 outcrop section (Dry Creek). Sections A-I are arranged from north to south. The Dry Creek section shows the greatest total amount of total subsidence. The period of greatest tectonically driven subsidence is observed between 93-85 in the north, but is younger (~83-80) in the south and east. This pattern reflects the overall southward and eastward migration of the primary depositional center.

ALLOCHTHONOUS SALT IMPACT ON THE RESERVOIR ARCHITECTURE IN THE THUNDER HORSE MINI-BASIN, MISSISSIPPI CANYON, GULF OF MEXICO

Wisam AlKawai[1,*], Tapan Mukerji[2], Kristian Meisling[1], Stephan Graham[1] and Allegra Hosford Scheirer[1]
[1]Department of Geological Sciences, Stanford University
[2]Department of Earth Resources Engineering, and of Geophysics, Stanford University
[*]walkawai@stanford.edu

Introduction

The northern Gulf of Mexico basin is one of the most prolific petroleum provinces in the world. Although it is one of the most extensively studied sedimentary basins, there are still ambiguities regarding the mechanisms of the petroleum system development due to several factors such as the structural complexity associated with salt tectonism (McBride et al., 1998; Stover et al., 2001). Basin and petroleum system modeling is a powerful tool to investigate the development of the petroleum system, from the maturation of the source rock to the charging of the reservoir (Hantschel and Kauerauf, 2009; Peters, 2009). Modeling reliable scenarios of hydrocarbon migration requires careful description of the distribution of reservoir lithofacies distribution (McBride et al., 1998; Stover et al., 2001; Hantschel and Kauerauf, 2009).

Previous studies of the deep-water sand deposition in topographically confined mini-basin by salt diapirs suggested dynamic interplay between sediment deposition and salt withdrawal (Mahaffie et al., 1995; Prather et al., 1998; Rowan and Weimer, 1998). The Thunder Horse mini-basin (Figure 1) is characterized by a dynamic salt movement history that includes formation of initial salt withdrawal mini-basin, and subsequent inversion into a turtle structure (Lapinski et al., 2004). In this study, we focus on interpreting the reservoir architecture starting at a coarse-scale, using inverted seismic impedance volumes. Then, we combine these results with interpretation of the salt movement through time to understand its implication for controls on reservoir architecture. The results from interpreting the salt movement together with the reservoir architecture serve as a foundation for modeling the petroleum system evolution.

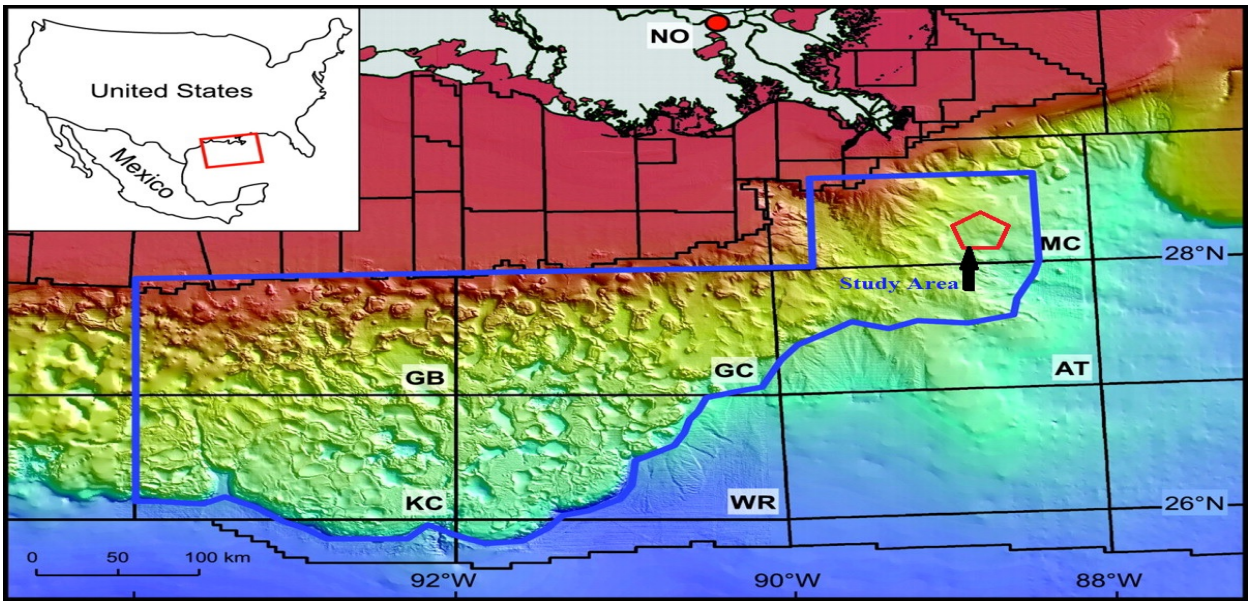

Figure 1. Location map of the Thunder Horse mini-Basin edited from Lapinski et al. (2004).

Structural Evolution

The study area is divided into two oil fields (Figure 2a): Thunder Horse Field, associated with the crest of the turtle structure; and Thunder Horse North, associated with the three-way closure against a rising salt diapir. We mapped multiple horizons between 120 to 5 Ma based on biostratigraphic data in one of the wells together with a depth-converted 3D seismic volume (Figure 2a). We interpreted the salt movement based on thickening and thinning of the horizons together with lap-out relationships. The key event to interpret, based on the onlap with the 66 Ma horizon together with the thickening at the center of the horizons ranging between 44 to 15.50 Ma (Figure 2b), is the base of a mini-basin formed due to the salt withdrawal around the center. Pronounced thickening within the 13.50-9.00 Ma interval along the flanks suggests that high sedimentation continued during middle Miocene to fill the mini-basin and caused salt withdrawal along the flanks (Figure 2c). This resulted in inverting the mini-basin into the present day turtle structure.

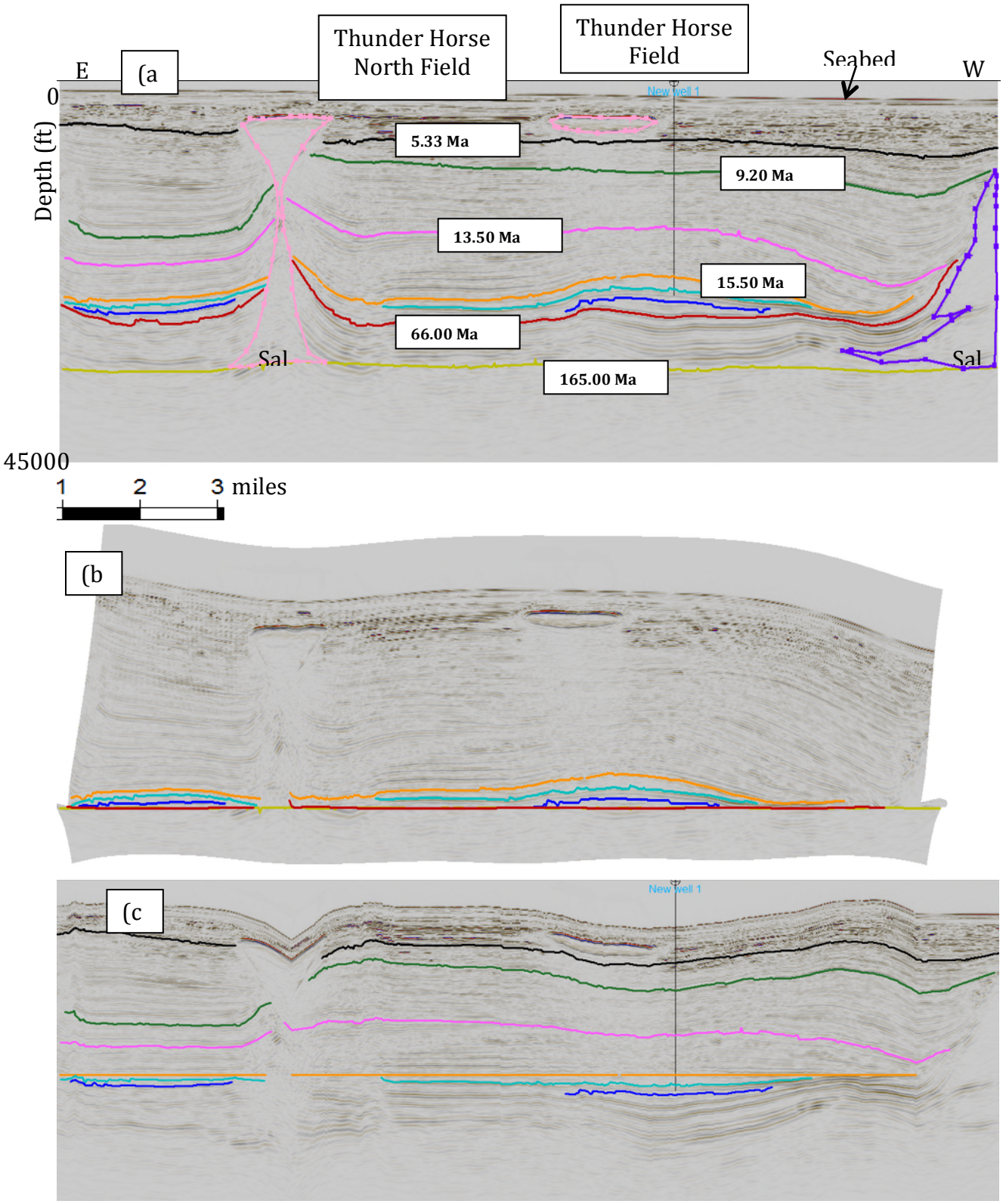

Figure 2. Seismic Section showing: (a) the structure of the area together with the mapped horizon, (b) the same section in (a) after flattening it on the 165.00 Ma horizon (i.e. base salt) and (c) flattening the same section again on the 66.00 Ma horizon.

The key reservoir intervals are interpreted to be middle Miocene deep-water sandstones (Lapinski et al., 2004). We focused in this study on three reservoir intervals: interval III (15.50-14.75 Ma); interval II (14.75-13.50 Ma); and interval I (13.50-13.00 Ma). We mapped the sandstone and shale lithofacies of each of these intervals by classifying inverted acoustic impedance and far angle (36°) elastic impedance based on the observed impedances values distributions for each lithofacies in the well-log data. The resulting lithofacies maps show a remarkable shift in the spatial distribution of sandstone in interval I when compared to intervals II and III. Interval I shows thin elongated sandstone bodies concentrated in the northern flank of the mini-basin unlike intervals II and III that have concentration of thin sandstone bodies in the northern flank and somewhat spatially extensive sandstone bodies in the center of the mini-basin. This change of deposition pattern coincides with the shift of the structure from a mini-basin into a turtle structure.

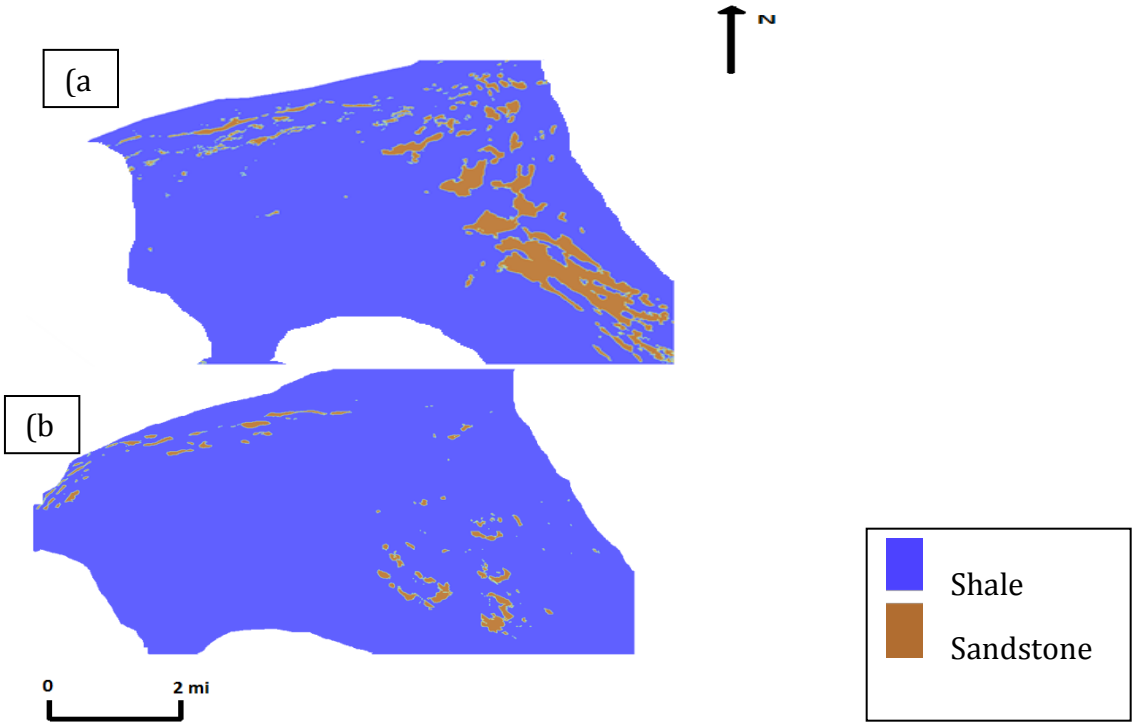

Figure 3. Reservoir lithofacies maps of intervals: (a) II and (b) I.

Conclusions and Future Work

The distribution of the reservoir lithofacies seems to have been highly influenced by the salt movement that reshapes the mini-basin topography through time. Future work will focus on building a full salt restoration model, integrated with a refined scale of reservoir lithofacies interpretation in which well-log and core data are combined with the coarse scale lithofacies maps to further delineate the depositional architecture. Understanding the interplay between salt movement and deposition of sand in this mini-basin is crucial for petroleum exploration in salt withdrawal mini-basins, as it serves as a building block to model the petroleum system development.

Acknowledgements

The authors thank BP for providing the dataset used in this study. Funding and participation in this research is made possible through the support of the Stanford Basin and Petroleum System Modeling, Stanford Project on Deep-Water Depositional Systems (SPODDS), Stanford Center for Reservoir Forecasting, and Stanford Rock Physics industrial affiliate programs and through the Saudi Aramco Scholarship. Special thanks to Stew Levin (Stanford Exploration Project) for support in setting up the project. Schlumberger graciously provided PetroMod® software. CGG Geosoftware provided the license for Hampson Russell®. Halliburton provided the license to Decision Space Desktop®.

References

Hantschel, T., Kauerauf, A., 2009, Fundamentals of Basin Modeling. Springer-Verlag, Heidelberg, 425 pp.

Lapinski, T., Bouroullec, R., and Weimer, P., 2004, Structural evolution of the Thunder Horse mini-basin, Mississippi Canyon, northern deep Gulf of Mexico: GCAGS Transactions, v. 54, p. 313-326.

Lapinski, T., Weimer, P., and Bouroullec, R., 2004, Sequence stratigraphic evolution of Thunder Horse mini-basin, Mississippi Canyon, northern deep Gulf of Mexico: GCAGS Transactions, v. 54, p. 327-341.

Mahaffie, M.J., Barnard, R.S., Kendrick, J.W., and Franceware, L.B., 1995, The interaction between accommodation space and sediment supply on depositional fill patterns within the greater Mars basin, deep-water Gulf of Mexico, U.S.A. (abs.): AAPG Annual Convention Program, p. 59A.

McBride, B., Rowan, M., Weimer, P., 1998, The evolution of allochthonous salt systems, northern Green Canyon and Ewing Bank (offshore Louisiana), northern Gulf of Mexico: AAPG Bulletin, v. 85, i.5B, p. 1013-1036.

Peters, K.E., 2009, Getting Started in Basin and Petroleum System Modeling: American Association of Petroleum Geologists(AAPG) CD-ROM #16, AAPG Datapages.

Rowan, M. G. and Weimer, P., 1998, Salt-sediment interaction, Northern Green Canyon and Ewing Bank (offshore Louisiana), Northern Gulf of Mexico 1: AAPG Bulletin, v. 82, p. 1055-1082.

Stover, S.C., Weimer, P., Ge, S., 2001, The effects of allochthonous salt evolution and overpressure development on source rock thermal maturation: a two-dimensional transient study in the northern Gulf of Mexico Basin: Petroleum Geosciences, 7, 281-290

CONSTRAINING PRESSURE AND THERMAL HISTORY BY COMBINING BASIN MODELING WITH ROCK PHYSICS: APPLICATIONS TO THE GULF OF MEXICO

Wisam AlKawai[1,*], Tapan Mukerji[2], Nader Dutta[2], Stephan A. Graham[1] and Allegra Hosford Scheirer[1]
[1]Department of Geological Sciences, Stanford University
[2]Department of Earth Resources Engineering, and of Geophysics, Stanford University
[*]walkawai@stanford.edu

Introduction

Basin and Petroleum System Modeling (BPSM) predicts pressure and thermal histories in sedimentary basins by simulating deposition, subsidence, and erosion and uplift (Hanstschel and Kauerauf, 2009; Peters, 2009). In this simulation, BPSM solves coupled partial differential equations (PDEs) with moving boundaries to calculate values of rock properties in space and time. Pressure and thermal histories can alter rock properties such as seismic velocity and porosity through compaction and diagenesis (Dvorkin and Nur, 1996; Avseth, 2005). In this study, we show two examples of how combining BPSM with rock physics modeling can improve predictions of pressure and thermal history. The first example is guiding the rock physics modeling in predicting changes in elastic properties due to smectite-to-illite transformation and applying these models in new well locations to predict pore pressure. The other example is improving thermal conductivities in the basin model by optimizing an empirical rock physics transform for predicting thermal conductivity based on petrophysical properties.

To show an example of guiding rock physics modeling through BPSM, we model changes in elastic properties associated with smectite-to-illite diagenesis. Many authors showed the changes of porosity, density, and seismic velocity relationship with effective stress due to smectite-to-illite transformation (Lahann, 2002; Katahara, 2003; Lahann and Swarbrick, 2011). Katahara (2003) questioned the application of such rock physics models in frontier areas due to lacking information about the depth of the transformation zone. We show how BPSM results can guide modeling the elastic properties changes and applying the models to predict pore pressure in new wells based on seismic velocities.

In the other example, we explore constraining the basin model thermal conductivities based on seismic velocities. Models of effective thermal conductivity of porous media such as the model by Maxwell-Euken (1932) suggested that thermal conductivity is a function of porosity in a form that is equivalent to Hashin-Shtrikman upper bound, which itself describes effective elastic moduli of porous media as functions of porosity. Because both thermal conductivity and seismic velocity are functions of porosity, studies showed that the relationship between thermal conductivity and other petrophysical properties such as seismic velocity can be simplified into a linear relationship (Houbolt and Wells, 1981; Zamora, 1993; Fuchs et al., 2015). In this study, we use this linear relationship to estimate the basin model thermal conductivities based on average sonic log velocities.

Modeling Smectite to Illite Effects

We integrated basin modeling with rock physics to quantify the changes in elastic properties due to smectite-to-illite transformation, as well as the implications for predicting the resulting overpressure. We used a dataset from the Thunder Horse Mini-basin in Mississippi Canyon (Gulf of Mexico), which includes both Thunder Horse and Thunder Horse North Fields. The dataset consists of 3D seismic data and velocity cubes for depth conversions, well-log data, and core XRD data from two wells. We built a 2D basin model that transects two wells in both fields to simulate the smectite-to-illite transformation. After calibrating the model to temperature data from the two wells, the simulation results of the transformation match the XRD data of clay samples in these two wells. The simulations suggest a shallower depth of the completion of transformation in Thunder Horse (i.e. 24,960 ft) compared to that in Thunder Horse North (i.e. 25,376 ft) due to the total coverage of Thunder Horse North by a shallow salt body that rapidly absorbs heat from the sediments below it.

Combining the simulation results with the well-log data and pore pressure measurements in the two wells, we observed changes in the relationships between P and S waves velocities (Vp and Vs), porosity, density, and effective stress. The zone of the completion of transformation in each well shows a change of the Vp and density relationship marked by a decrease of velocity and a slight increase in density (Figure 1a). When we modeled the relationships between seismic velocities and porosity, the same zone showed steepening of velocity-porosity trends. Compaction trends of Vp and porosity with effective stress show a shift toward a more compacted rock after the transformation as higher Vp and lower porosity become achievable at a lower effective stress (Figure 1b). These results suggest the need to modify compaction curves when predicting pore pressure from seismic velocities at the transformation zone. Detection of the transformation zone can come from basin modeling results. Another potential detection method based on the findings of this study is the change in amplitude variations with offset (AVO) due to changes in elastic properties driven by the transformation.

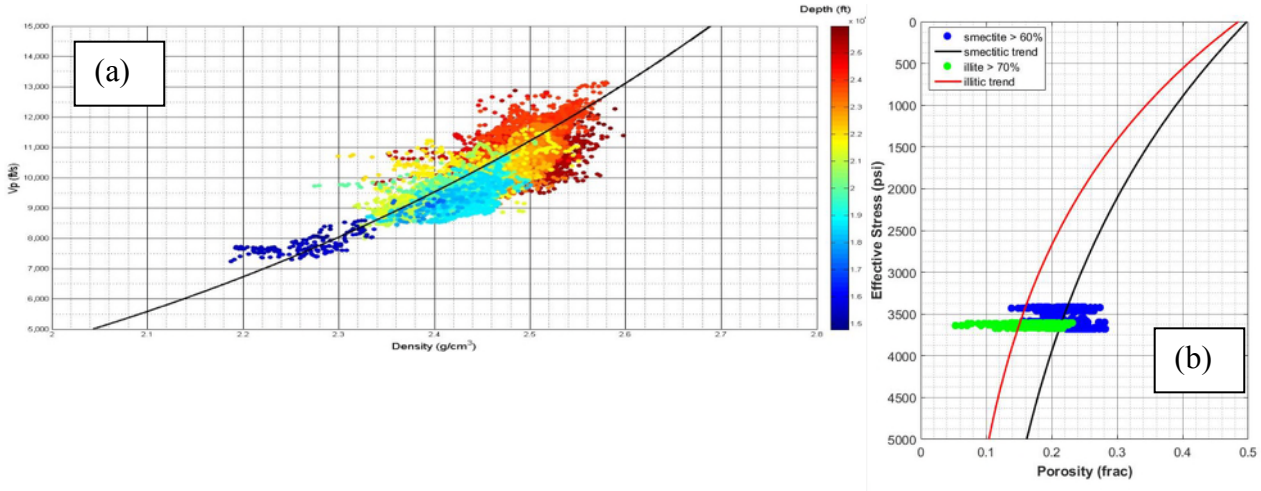

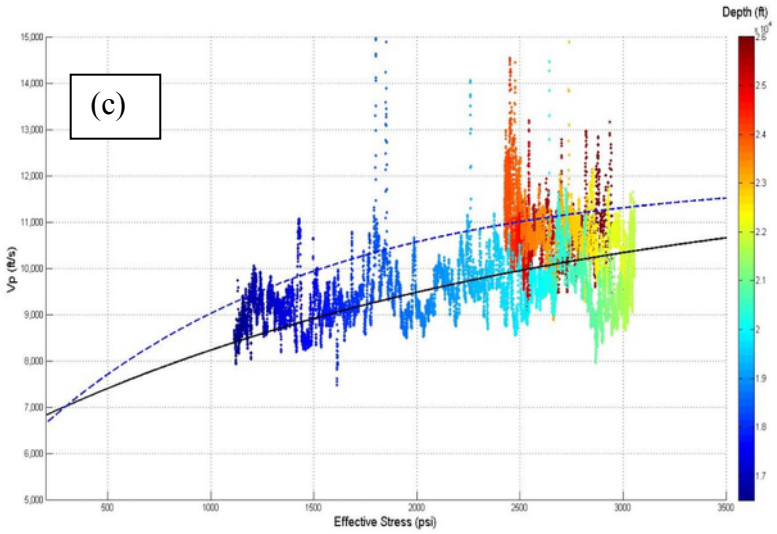

Figure 1. Smectite to illite transformation effects on Vp-density relationship (a) and compaction trends of porosity (b) and Vp (c).

Constraining Thermal Conductivities

We used the same dataset to build a 1D model in a well located in Thunder Horse Field. The lithology for each layer is a mixture of sandstone and shale based on average gamma ray values. In this model, the thermal conductivities are calculated based on geometric averaging between sandstone and shale. After calibrating this model to porosity, density, and pore pressure data, we optimized the basal heat flow based on the basin history. Resulting model temperatures are close to the corrected bottom hole temperature (BHT) data in the same well (Figure 2a). However, the apparent geothermal gradient of the basin model output is different from that of the BHT, which can have considerable implications for thermal history related processes such as source rock maturation. Thus, we estimated thermal conductivities based on their linear relationship to P-wave slowness (Fuchs et al., 2015). Fuchs et al. (2015) recognized the uncertainties in well-log based predictions of thermal conductivities based on the well-log combinations used and potentially the lithology. In this step, we tried optimizing the model for estimated thermal conductivity based on well-logs to produce a basin modeling scenario that matches BHT values and gradient. The optimization process is iterative. We used the calculated conductivities from well-logs together with BHT data to adjust the Sekiguchi (1984) models, which are used in the basin model to describe variations of thermal conductivities with temperature. The optimized thermal conductivities (Figure 2b) result in a better temperature calibration in the well (Figure 2c).

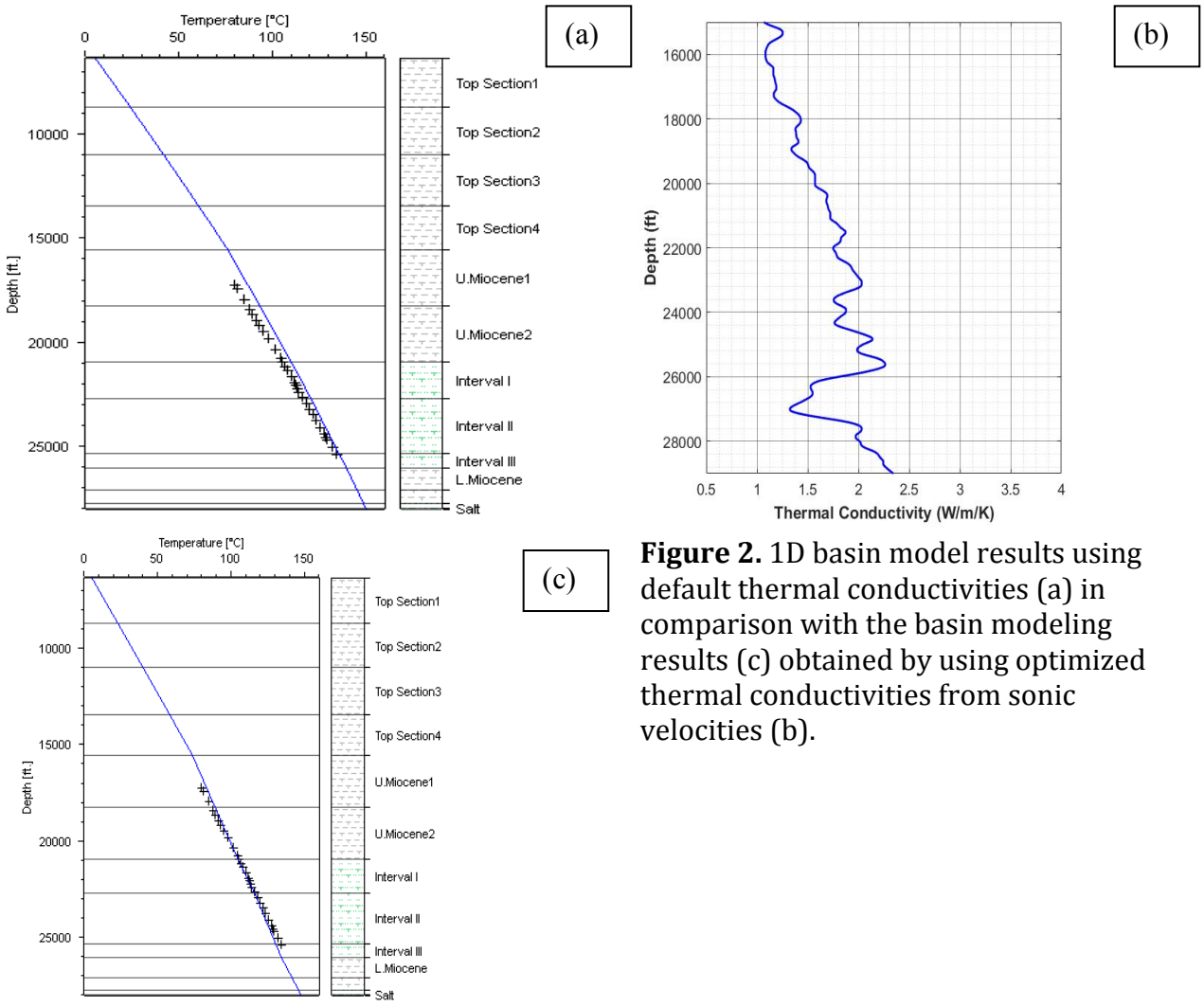

Figure 2. 1D basin model results using default thermal conductivities (a) in comparison with the basin modeling results (c) obtained by using optimized thermal conductivities from sonic velocities (b).

Conclusions

The modeling of elastic properties changes due to smectite-to-illite diagenesis showed the use of basin modeling results in predicting the transformation zone. This is important to establish reliable rock physics models and be able to use them away from available well control such as using them to predict pore pressure based on seismic velocities. The other part of the study, in which thermal conductivities are constrained by seismic velocities, is a useful approach of adding an extra control on thermal history obtained from basin modeling, especially because thermal conductivity data are difficult to obtain in many cases. The limitation of this approach is that it requires BHT data to be able to optimize the basin model along with the estimation of thermal conductivities based on seismic velocities.

Acknowledgements

The authors thank BP for providing the dataset used in this study. Funding and participation in this research is made possible through the support of the Stanford Basin

and Petroleum System Modeling, Stanford Project on Deep-Water Depositional Systems, Stanford Center for Reservoir Forecasting, and Stanford Rock Physics industrial affiliate programs and through the Saudi Aramco Scholarship. Special thanks to Stew Levin (Stanford Exploration Project) for support in setting up the project. Schlumberger graciously provided PetroMod® software. CGG Geosoftware provided the license for Hampson Russell®. Halliburton provided the license to Decision Space Desktop®.

References

Avseth, P., Mukerji, T., & Mavko, G. 2005. Quantitative Seismic Interpretation. pp. 376. ISBN 0521816017. : Cambridge University Press, Cambridge, UK

Dvorkin, J., and A. Nur, 1996, Elasticity of high-porosity sandstones: Theory for two Nort datasets, Geophysics, 61, 1363-1370.

Eucken, A. (1932). Heat transfer in ceramic refractory materials: Calculation from thermal conductivities of constituents. Fortchg. Gebiete Ingenieurw. B, 3(1), 353-360.

Fuchs, S., Balling, N., & Förster, A. (2015). Calculation of thermal conductivity, thermal diffusivity and specific heat capacity of sedimentary rocks using petrophysical well logs. Geophysical Journal International, 203(3), 1977-2000.

Hantschel, T., Kauerauf, A., 2009. Fundamentals of Basin Modeling. Springer-Verlag, Heidelberg, 425 pp.

Houbolt, J. J. H. C., & Wells, P. R. A. (1981). Estimation of Heat Flow in Oil Wells Based on Relation Between Heat Conductivity and Sound Velocity: ABSTRACT. AAPG Bulletin, 65(7), 1360-1361.

Katahara, K. (2003, January). Analysis of overpressure on the Gulf of Mexico Shelf. In Offshore Technology Conference. Offshore Technology Conference.

Lahann R.W., 2002, Impact of smectite diagenesis on compaction modeling and compaction equilibrium. In: Pressure Regimes in Sedimentary Basins and Their Prediction (Huffman AR, Bowers GL, *eds.*) AAPG Memoir, 76, 61–72.

Lahann, R. W. and Swarbrick, R. E. ,2011, Overpressure generation by load transfer following shale framework weakening due to smectite diagenesis. Geofluids, 11(4), 362–375.

Sekiguchi, K. ,1984, A method for determining terrestrial heat flow in oil basinal areas. Tectonophysics, 103(1), p. 67-79.

Zamora, M., Vo-Thanh, D., Bienfait, G., & Poirier, J. P. (1993). An empirical relationship between thermal conductivity and elastic wave velocities in sandstone. Geophysical Research Letters, 20(16), 1679-1682.

PETROLEUM SYSTEM CHARACTERIZATION OF TERREBONNE MINI-BASIN GAS HYDRATES IN NW WALKER RIDGE AREA (GULF OF MEXICO)

Laura N. Dafov[1,*], Allegra Hosford Scheirer[1], Ray Boswell[2], and Yongkoo Seol[2]
[1]*Department of Geological Sciences, Stanford University*
[2]*U.S. Department of Energy, National Energy Technology Laboratory*
[*]ldafov@stanford.edu

Abstract

Gas hydrates hold vast volumes of methane and affect a wide range of scientific interests including drilling hazards, potential future energy resource, global carbon cycling, geohazards, and climate change. The Bureau of Ocean Energy Management estimates 607 trillion cubic meters (21,444 trillion cubic feet) of gas hydrates in place in the Gulf of Mexico (GoM) alone (Boswell et al., 2012). Although total global estimates of gas hydrate volumes vary, even the most conservative estimates consider methane hydrates to be the world's largest reservoir of fossil fuel with it potentially being at least 3 times larger than all of the world's conventional and unconventional oil, gas and coal combined (Wygrala et al., 2016).

There is great opportunity for improving our understanding of gas hydrates through the basin and petroleum system modeling (BPSM) approach. BPSM is a well-established discipline that integrates geology, geophysics, geochemistry, engineering, geostatistics, rock physics and more to predict the generation, migration, and accumulation of petroleum. That prediction is accomplished by forward simulating the sedimentary basin through time. Though widely used in academy and industry, BPSM has only rarely been used to study gas hydrate systems. The reasons for that are varied, but BPSM is ideally suited for gas hydrate modeling due to its sophisticated treatment of subsurface pressure and temperature through time. BPSM is also optimally suited for modeling gas hydrates due to its ability to handle very short time steps and very fine spatial resolutions. In this way, BPSM can capture the temporal (and thus spatial) variability in gas hydrate deposits as well as changing conditions in the water column that can affect the gas hydrate stability zone.

The research project area of interest is the Terrebonne Basin in the northern GoM continental slope, a salt-withdrawal mini-basin in northwest Walker Ridge (WR) Area, including WR Block 313 (**figs. 1 and 2**). The 2009 GoM Gas Hydrates Joint-Industry-Project (JIP) Leg II drilling program provides much of the background data necessary for constructing an Earth model of the region for gas hydrate modeling (Boswell et al., 2011; Boswell et al. 2012; Frye et al., 2012; Myshakin et al. 2011). Proposed work includes: 1) Method development- Construct and integrate a 4D basin model of the entire Terrebonne mini-basin with a high-resolution deep-water sediment flow model; 2) Identify and characterize the petroleum system(s); 3) Geochemical analyses. Some of the questions that will be addressed by this research include: a) Do you need deep source/long migration to achieve the observed result; b) What is the actual history of these deposits with respect to the gas hydrate stability zone, recognizing that this area is not one characterized by simple

continuous sedimentation and subsidence, but instead by periodic uplift, tilting, plate rotation, sea-level change, salt tectonics, and evolution of temperature gradients.

In conclusion, BPSM has been called the 'great integrator' in petroleum exploration (Hosford Scheirer, 2014). Development of a BPSM model of gas hydrates in the Terrebonne mini-basin of the northern GoM will provide a vehicle within which to integrate other early exploration and assessment research being conducted on gas hydrates, a resource likely to provide many decades of energy if proven to be commercially producible in the future.

Figures

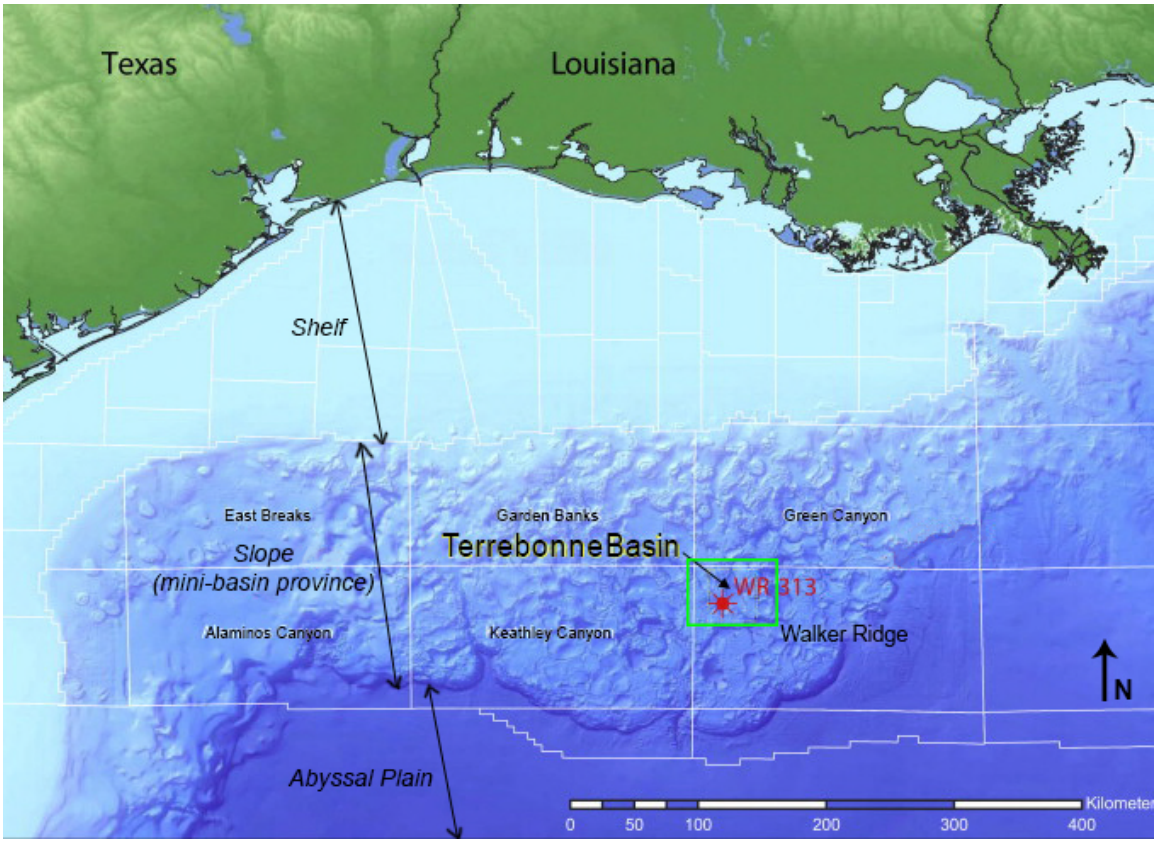

Figure 1. Northern Gulf of Mexico bathymetric relief map. JIP Leg II drilling site labeled in red (WR 313). Terrebonne Basin is shown in NW corner of Walker Ridge Planning Area. Green box encompasses area shown in Fig. 2. Modified from Frye et al., 2012 and Boswell et al. 2012.

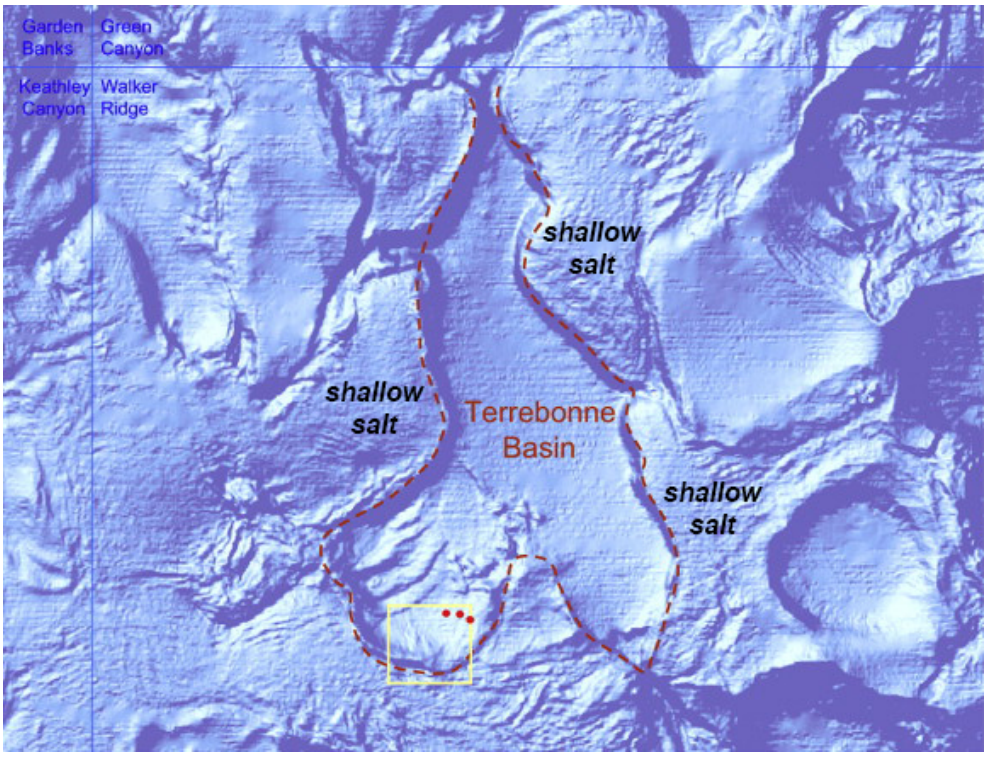

Figure 2. Shaded bathymetry map of the northwest Walker Ridge Protraction Area. See Fig. 1 for outline of this area in green box, scale, and direction. The modern expression of the Terrebonne Basin is highlighted by red dashed line. Walker Ridge block 313 is outlined in yellow. Well locations are shown in red. Modified from Frye et al., 2012 and Boswell et al. 2012.

Acknowledgements

The authors thank The National Energy Technology Laboratory (NETL) for supporting the participation in and funding of this research. We also thank Schlumberger for providing PetroMod petroleum systems modeling software.

References

Boswell, R., M. Frye, D. Shelander, W. Shedd, D.R. McConnell, and A. Cook, 2011, Architecture of gas-hydrate-bearing sands from Walker Ridge 313, Green Canyon 955, and Alaminos Canyon 21: Northern deepwater Gulf of Mexico, v. 34, p. 1-16.

Boswell, R., T.S. Collett, M. Frye, W. Shedd, D.R. McConnell, and D. Shelander, 2012, Subsurface gas hydrates in the northern Gulf of Mexico, Marine and Petroleum Geology, v. 34, p. 4-30.

Hosford Scheirer, A., 2014, The 'great integrator' in petroleum exploration, Hart's Exploration and Production Magazine, 3 p. [http://www.epmag.com/great-integrator-petroleum-exploration-758546#p=full]

Frye, M., W. Shedd, and R. Boswell, 2012, Gas hydrate resource potential in the Terrebonne Basin, Northern Gulf of Mexico, Marine and Petroleum Geology, v. 34, p. 150-168.

Myshakin, E.M., M. Gaddipati, K. Rose, and B.J. Anderson, 2011, Numerical simulations of depressurization-induced gas production from gas hydrate reservoirs at the Walker Ridge 313 site, northern Gulf of Mexico, Marine and Petroleum Geology, v. 34, p. 169-185.

Wygrala, B., R. Wolf, and T. Fuchs, 2016, Modeling Gas Hydrates in Petroleum Systems, Schlumberger, PetroMod White Paper, 23 p.

UNDERSTANDING DEPOSITIONAL ENVIRONMENTS OF THE SHUBLIK FORMATION OF ARCTIC ALASKA USING XRF CHEMOSTRATIGRAPHY

Inessa Yurchenko*, Stephan A. Graham, and Allegra Hosford Scheirer
Department of Geological Sciences, Stanford University
*inessa@stanford.edu

Abstract

Organic-rich sediments are deposited over a wide range of depositional environments. Understanding what controls the environment of deposition may help to predict the distribution of source rock properties. Numerous studies are devoted to understanding the factors controlling productivity and preservation of organic matter, such as anoxia, sedimentation rates, amount of nutrients, and type of organic macerals (Demaison and Moore, 1980; Pedersen and Calvert, 1990). Although many similarities exist in source rocks, many important differences also occur that might be used to differentiate them.

The Middle to Upper Triassic Shublik Formation is one of the key source rocks for hydrocarbons in Arctic Alaska and the greater Prudhoe Bay field area, one of the largest fields in North America (Bird and Molenaar, 1987; Magoon and Bird, 1985; Bird, 1994). It is a laterally and vertically heterogeneous unit that has been described both in outcrop and in the subsurface, and interpreted to have been deposited under fluctuating oceanic upwelling conditions (Parrish, 1987; Kupecz, 1995; Parrish et al., 2001). Modern upwelling zones are mainly associated with western sides of continents in low- to intermediate latitudes, where nutrient-rich waters result in high productivity, and are considered to be the most productive ecosystems in the ocean (Capone and Hutchins, 2013). Consistent with a coastal upwelling zone deposition interpretation (Parrish et al., 2001), the Shublik Formation is characterized by calcareous, glauconitic, phosphatic, and organic-rich lithofacies that reflect the chemical environment of Shublik deposition, suggesting that their major element and trace metal composition could be used as a proxy for paleoredox and paleoproductivity.

This study focuses on chemostratigraphic analysis of three Shublik cores using hand-held XRF data as elemental proxies for environment of deposition. The two most distant cores are 65 miles apart, and represent proximal and distal end-members. In addition to analysis of individual major and trace elements (over 20 elements) and elemental ratios (e.g. Si/Al, Si/Ti), a hierarchical cluster analysis has been applied to produce chemofacies. Combining chemofacies with biomarker paleoredox proxies, lithological description of the cores, and stochastic electrofacies analysis of well logs provides a highly-detailed, core-based understanding of the Shublik source rock environment of deposition.

Introduction

Although it has been recognized that organic-rich sediments vary lithologically, the majority of source rock research is historically focused on detailed organic geochemical assessments rather than sedimentological analysis. Conventional cores are primarily drilled for reservoir rocks, and much of the source rock analysis has been done on cuttings and/or outcrop samples, creating interpretive pitfalls. The recent success in shale-oil and shale-gas exploration and production has shifted the research focus from reservoir rock to source rock, and emphasized the importance in recognizing the geochemical and lithological heterogeneity of this part of the petroleum system (Jarvie, 2012). Source rock coring is now an essential part of the unconventional shale resource exploration procedure, and it provides vast opportunities for advanced shale research.

Geological background

Arctic Alaska is a prolific petroleum province that contains a great share of US energy resources (Bird and Houseknecht, 2011). Nearly all petroleum-producing fields are located in the Central North Slope, the area situated between the National Petroleum Reserve in Alaska (NPRA) to the west and the Arctic National Wildlife Refuge (ANWR) to the east (Fig. 1). The majority of the production is concentrated in the north, whereas the southern part of the Central North Slope remains only lightly explored. The origin of hydrocarbons has been debated and discussed in numerous publications since the discovery of the supergiant Prudhoe Bay field in 1967. It has been widely recognized that crude oil accumulations in the North Slope commonly represent a mixture of oils derived from several source rocks (Seifert et al., 1980, Wicks et al., 1991, Masterson, 2001, Peters et al., 2008). Four key petroleum source rocks identified in the North Slope include the Triassic Shublik Formation, Jurassic Lower Kingak Shale, Cretaceous pebble shale unit and Cretaceous Hue Shale (Fig. 2; Magoon and Bird, 1985; Bird, 1994; Houseknecht and Bird, 2004; Peters et al., 2006).

The Middle to Upper Triassic Shublik Formation is one of the key source rocks for hydrocarbons in Arctic Alaska and the greater Prudhoe Bay field area, accounting for nearly all of the oil in the Kuparuk River unit and about third of the oil in the Prudhoe Bay unit (Bird and Molenaar, 1987; Magoon and Bird, 1985; Bird, 1994; Peters et al., 2008). The Shublik Formation is a very heterogeneous unit interpreted to have been deposited on a south-facing passive margin under fluctuating oceanic upwelling conditions (Parrish, 1987; Kupecz, 1995; Parrish et al., 2001). As recognized by Demaison and Moore (1980), upwelling is one of the four major anoxic environments favorable for source rock deposition. Modern upwelling zones are mainly associated with western sides of continents in low latitudes, where nutrient-rich waters result in high productivity, and are considered to be the most productive ecosystems in the ocean (Capone and Hutchins, 2013). The Shublik Formation sediments are distinguished by a characteristic set of lithologies that include glauconitic, phosphatic, organic-rich, and cherty facies consistent with a coastal upwelling zone deposition interpretation (Parrish et al., 2001). These lithofacies reflect the chemical environment in which the Shublik Formation was deposited, suggesting that their major element and trace metal composition could be used as a proxy for understanding

paleoredox and paleoproductivity conditions (Parrish et al., 2001; Kelley et al., 2007). Since Bailey (2012) proclaimed the Shublik Formation as the main target of unconventional shale-oil exploration, understanding its organic-rich facies distribution and petroleum potential has become particularly important. There is renewed interest in the Shublik as an unconventional play since Great Bear Petroleum leased 500,000 acres in the Central North Slope south of the producing fields in 2010 (Hosford Scheirer et al., 2014).

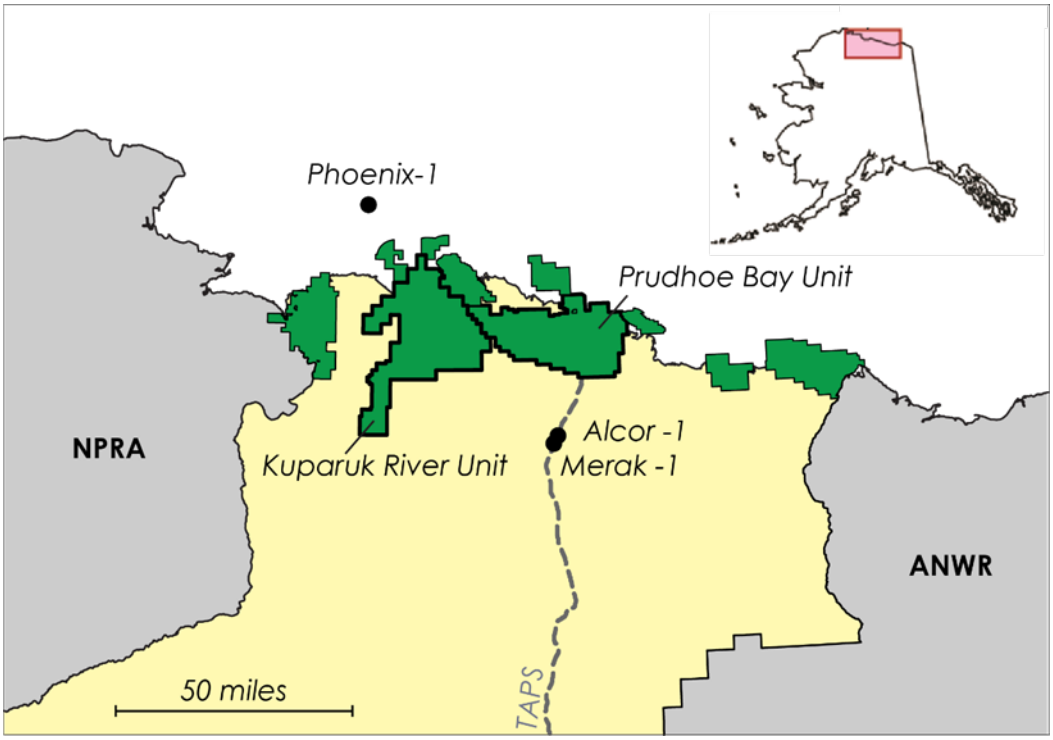

Figure 1: Map of part of Arctic Alaska showing location of study area. Central North Slope is indicated in yellow. Main producing oil fields are in green, NPRA - National Petroleum Reserve in Alaska, ANWR - Arctic National Wildlife Refuge, TAPS - Trans-Alaska Pipeline System.

Summary and Conclusions.

Even though lithological heterogeneity and thickness variability of the Shublik Formation has being widely recognized, most of the source rock literature refers to it as one source rock unit. Robison et al. (1996) published the most detailed core-based analysis of the Shublik Formation in the Phoenix-1 well (Fig. 1). His study utilized more than 60 samples in 300 ft of Shublik section and suggested presence of multiple organofacies with different hydrogen index (HI) and TOC values. Whereas the most widely-used sub-classification of the Shublik Formation is the zonation scheme of Kupecz (1995), which subdivided the Shublik into four zones (from A to D) based on their gamma-ray log signature, that reflect lithologic contrast between phosphatic sandstones (zone D), interlaminated black shales and limestones (zone C), phosphorites and phosphatic carbonates (zone B), interlaminated shales and carbonate grainstones (zone A).

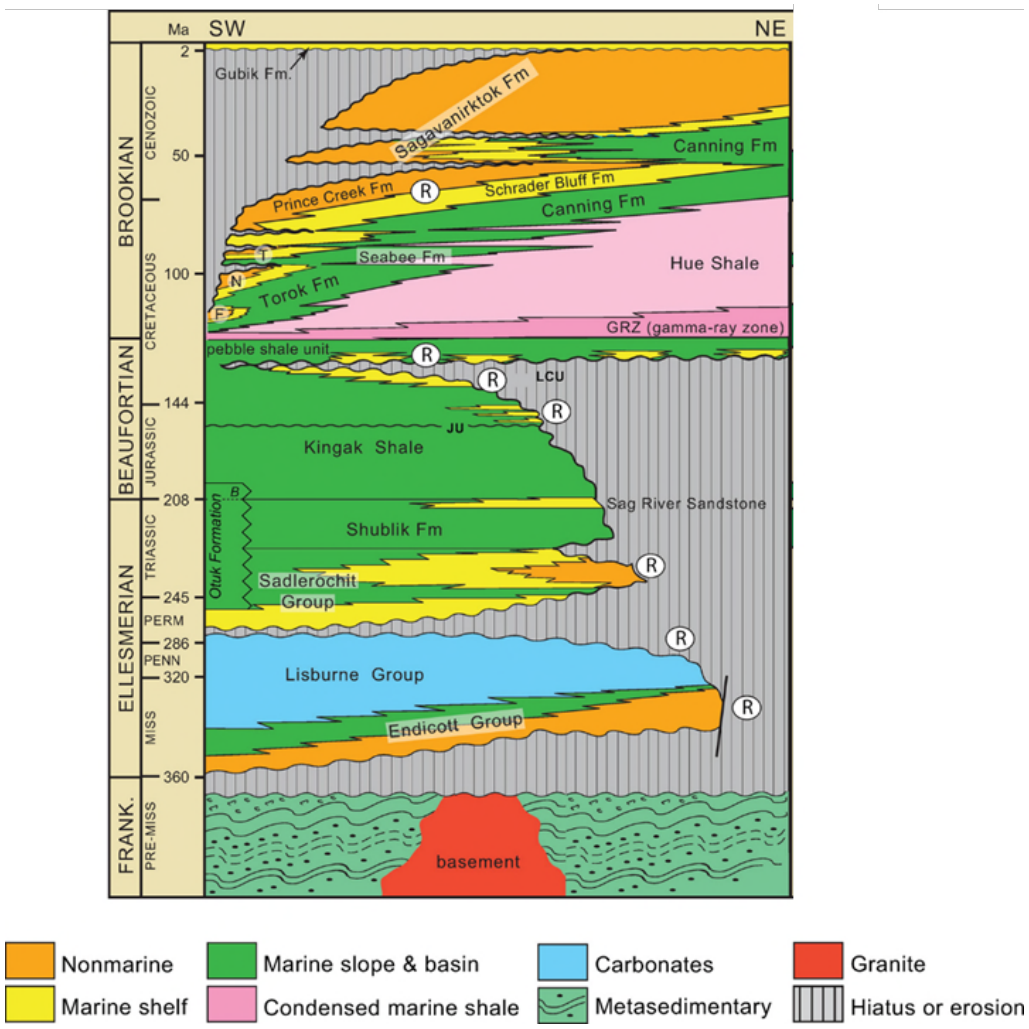

Figure 2: Generalized chronostratigraphic column of Alaska North Slope after Bird and Houseknecht (2011). Key petroleum source rocks are Shublik Formation, Kingak Shale, and Hue Shale, including the GRZ (gamma ray zone).

Materials and methods

This study focuses on chemostratigraphic analysis of three Shublik cores (Fig. 1) using hand-held XRF data as elemental proxies for environment of deposition. The two most distant cores are 65 miles apart, and represent proximal and distal end-members.

The Tenneco Phoenix-1 (OCS-Y-0338) well, drilled on a structural feature northwest of the Prudhoe Bay field, recovered continuous core through the Shublik Formation (300 ft) that represents the most detailed published core-based analysis of the Shublik Formation to date (Robison et al., 1996). As part of the current work, this core was viewed at the USGS Core Research Center and scanned at 1ft interval using hand-held XRF device.

The Alcor-1 and Merak-1 wells, drilled by Great Bear Petroleum in 2012, cored Shublik Formation from top to bottom (~100 ft) in Merak-1 well and recovered over 80 ft in Alcor-1. The distance between two wells is less the 2 miles. Access to these Shublik cores was generously granted to the Basin and Petroleum System Modeling Research Group at Stanford University by Great Bear Petroleum. Both cores were scanned at 0.5 ft interval using hand-held XRF tracer.

Each core was scanned using Bruker Tracer IV-SD for data consistency. The instrument settings for trace elements analysis are 40 kV, 14.3 mA, Al-Ti filter, collection time of 60 seconds per sample. The setups for major elements analysis are 15 kV, 35 mA, 30 seconds per sample, with the vacuum pump (no filter). The current method provides rapid and non-destructive measurements of major elements heavier than sodium, and trace elements from barium to uranium. Quantification of elemental concentrations was performed using matrix-specific calibration described in Rowe et al. (2012). In addition a large number of samples was collected for carbonate content measurements based on sample weight difference before and after acid treatment. Resulted carbonate content (wt. %) of collected samples was compared to calcium content (wt. %) measured using non-destructive XRF analysis for data validation.

Results

Figure 3a provides comparison of the carbonate content from discrete hand samples versus calcium content from continuous XRF analysis for all three wells. Note that Phoenix-1 carbonate content data were taken from a USGS public data set, and not measured by the author. Calcium measurements by hand-held XRF appear to have excellent correlation with carbonate content, and provide an even higher resolution record that could be used for well-to-well correlations.

Figure 3b displays a chemostratigraphic summary of the Shublik Formation in Merak-1 core. This summary plot includes calcium and silicon content as carbonate and detrital deposition proxies; phosphorus and sulfur content as phosphate and sulfur enrichment indicators; and molybdenum and nickel as proxies for reducing conditions and productivity, respectively.

The collected XRF data were also compared to the gamma ray zonation (from A to D). The lithologic contrast between zone B and the over- and underlying zones A and C is easily recognized by elevated phosphorus content. Similarly, Zone D is composed of phosphorus-rich sediments, however silicon content seem to get increasingly higher towards the underlying Ivishak sandstone. Note that due to high phosphate content of the Shublik Formation, phosphorus is reported in net count rates instead of wt. %. The reference material set was developed for typical mudrock analysis and all references have phosphorus concentrations less than 20 wt. %, whereas the Shublik Formation is a very phosphate-rich unit and its phosphorus content often exceeds 20 wt. %. Thus, a broader range of reference materials is needed to define the phosphorus calibration curve for proper net count rates to concentration conversion (Rowe et al., 2012).

Finally, a multicomponent statistical analysis has been applied to all the major and trace elemental data in order to subdivide the Shublik Formation into XRF chemofacies. Results are validated using conventional geologic description of the core. There is a general agreement between core-derived lithofacies and XRF-derived chemofacies (Fig. 3b).

Figure 3: a - Carbonate content (acid-treatment method) versus calcium content (non-destructive hand-held

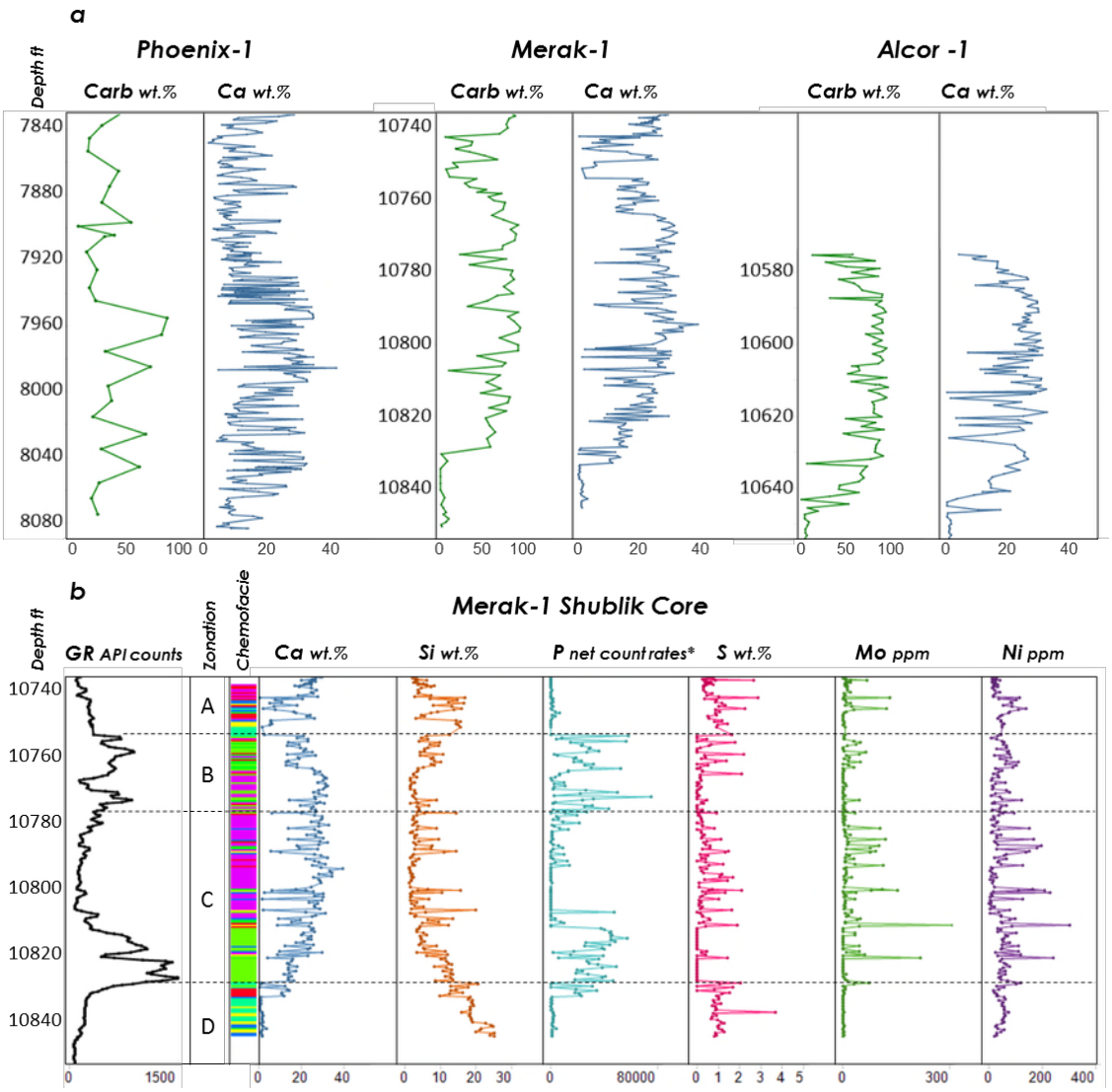

XRF) comparison of three wells. b – Shublik chemostratigraphy of Merak-1 core.* Note that due to high phosphate content of the Shublik Formation, phosphorus is reported in net count rates instead of wt. % (see text for details).

Summary

Rapid, non-destructive chemostratigraphic analysis of the Shublik Formation was performed using a handheld XRF tracer. Measured major element and trace metal composition were used as a proxy for paleoredox and paleoproductivity. In addition to analysis of individual major and trace elements (over 20 elements) and elemental ratios (e.g. Si/Al, Si/Ti), a multicomponent statistical analysis has been applied to produce

chemofacies. Using continuous XRF scanning of core, results show that the Shublik Formation can be effectively subdivided into chemofacies that are in agreement with lithofacies and can be used for well-to-well correlations and heterogeneity analysis. Moreover, current work also includes combining chemofacies with biomarker paleoredox proxies, and stochastic electrofacies analysis of well logs. Thus, this provides a highly-detailed, core-based understanding of depositional environments of the Shublik source rock of Arctic Alaska, which will ultimately contribute to the growing body of knowledge in such exploration frontiers linking geochemistry, sedimentology, and unconventional resource analysis.

Acknowledgements

We thank Les Magoon and Ken Bird for their support and recommendations during this research. We also thank Dr. Bruce Kaiser and Bruker Corporation for their discussions and assistance with instrumentation access. Special thanks are due to Ed and Karen Duncan and Great Bear Petroleum for granting access to Alcor-1 and Merak-1 Shublik cores and for sponsoring this research.

References

Bailey, A., 2012, The oil's there: Petroleum News, 17, no. 39, 1–15.

Bird, K.J., and Molenaar, C.M., 1987, Stratigraphy, in Bird, K.J., and Magoon, L.B., eds., Petroleum geology of the northern part of the Arctic National Wildlife Refuge, northeastern Alaska: U.S. Geological Survey Bulletin 1778, p. 37-59.

Bird, K.J., 1994. Ellesmerian(!) petroleum system, North Slope, Alaska, USA, in Magoon, L.B., Dow, W.G., eds., The Petroleum System – From Source to Trap. Tulsa, AAPG Memoir 60, p. 339–358.

Bird, K.J., and Houseknecht, D.W., 2011, Geology and petroleum potential of Arctic Alaska, in Spencer, A.M., Embry, A.F., Gautier, D.L., Stoupakova, A.V., and Sørensen, K., eds., Arctic petroleum geology: Geological Society of London Memoir 35, p. 485–499.

Capone, D.G and Hutchins, D.A., 2013, Microbial biogeochemistry of coastal upwelling regimes in a changing ocean: Nature, v. 6, p. 54-57, doi: 10.1038/ngeo1916.

Demaison, G.J. and Moore, G.T., 1980, Anoxic environments and oil source bed genesis: AAPG Bulletin 64, 1179-1209.

Hosford Scheirer, A., Magoon, L.B., Bird, K.J., Duncan, E.A., and Peters, K. E., 2014, Toward Successful Petroleum Production from Unconventional and Conventional Reservoirs in the Central Alaska North Slope: Unconventional Resources Technology Conference Control ID Number 1934939, 25-27 August, Denver, CO.

Houseknecht, D.W., and Bird, K.J., 2004, Sequence stratigraphy of the Kingak Shale (Jurassic–Lower Cretaceous), National Petroleum Reserve in Alaska: AAPG Bulletin 88, p. 279–302.

Jarvie, D. M., 2012, Shale resource systems for oil and gas: Part 1—Shale-gas resource systems, in J. A. Breyer, ed., Shale reservoirs - Giant resources for the 21st century: AAPG Memoir 97, p. 69–87.

Kelly, L.N., Whalen, M.T., McRoberts, C.A., Hopkin, E., and Tomsich, C.S., 2007, Sequence stratigraphy and geochemistry of the upper Lower through Upper Triassic of Northern Alaska: Implications for paleoredox history, source rock accumulation, and paleoceanography: Alaska Division of Geological & Geophysical Surveys Report of Investigation 2007-1, 50 p.

Kupecz, J.A., 1995, Depositional setting, sequence stratigraphy, diagenesis, and reservoir potential of a mixed-lithology, upwelling deposit, Upper Triassic Shublik Formation, Prudhoe Bay, Alaska: AAPG Bulletin 79, no. 9, p. 1301–1319.

Magoon, L.B. and Bird, K.J., 1985. Alaskan North Slope petroleum geochemistry for the Shublik Formation, Kingak Shale, pebble shale unit, and Torok Formation, in Magoon, L.B., Claypool, G.E., eds., Alaska North Slope Oil/Source Rock Correlation Study, vol. 20. Tulsa, AAPG Studies in Geology, pp. 31-48.

Masterson, W. D., 2001, Petroleum filling history of central Alaskan North Slope fields: Ph.D. thesis, University of Texas at Dallas, Dallas, Texas, 222 p.

Parrish, J.T., 1987, Lithology, geochemistry, and depositional environment of the Triassic Shublik Formation, northern Alaska, in Tailleur, I.L., and Weimer, P., eds., Alaskan North Slope geology: Field Trip Guidebook – SEPM, Pacific Section, Special Publication 50, p. 391–396.

Parrish, J.T., Whalen, M.T., and Hulm, E.J., 2001, Shublik Formation lithofacies, environments, and sequence stratigraphy, Arctic Alaska, U.S.A., in Houseknecht, D.W., ed., Petroleum Plays and Systems in the National Petroleum Reserve – Alaska: SEPM (Society for Sedimentary Geology) Core Workshop No. 21, p. 89–110.

Pedersen, T.F. and Calvert, S.E., 1990, Anoxia vs. productivity: what controls the formation of organic carbon-rich sediments and sedimentary rocks? AAPG Bulletin 74, p. 454 - 466.

Peters, K.E., Magoon, L.B., Bird, K.J., Valin, Z.C., and Keller, M.A., 2006, North Slope, Alaska: source rock distribution, richness, thermal maturity, and petroleum charge: AAPG Bulletin 90, p. 261–292.

Peters, K. E., Ramos, S. L., Zumberge, J. E., Valin, Z. C., and Bird, K. J., 2008, De-convoluting mixed crude oil in Prudhoe Bay Field, North Slope, Alaska: Organic Geochemistry 39, p. 623–645.

Robison, V.D., Liro, L.M., Robinson, C.R., Dawson, W.C., and Russo, J.W., 1996, Integrated geochemistry, organic petrology, and sequence stratigraphy of the Triassic Shublik Formation, Tenneco Phoenix #1 well, North Slope, Alaska, U.S.A.: Organic Geochemistry 24, no. 2, p. 257–272.

Rowe, H., Hughes, N., and Robinson, K., 2012, The quantification and application of handheld energy dispersive xray fluorescence (ED-XRF) in mudrock chemostratigraphy and geochemistry: Chemical Geology 324‐325, p. 122‐131.

Seifert, W. K., Moldowan, J. M., and Jones, R. W., 1980, Application of biological marker chemistry to petroleum exploration: Proceedings of the 10th World Petroleum Congress, Bucharest, Romania, September 1979, Paper SP8: Heyden & Son Inc., Philadelphia, Pennsylvania, p. 425–440.

Wicks, J. L., Buckingham, M. L., and Dupree, J. H., 1991, Endicott field– U.S.A., North Slope basin, Alaska, in N. H. Foster and E. A. Beaumont, eds., Structural traps V: AAPG Treatise of Petroleum Geology, Atlas of Oil and Gas Fields, p. 1–25.

MATHEMATICAL MODELING OF FRACTURE GROWTH IN SOURCE ROCK DURING KEROGEN THERMAL MATURATION

Yunfei (Iris) Yang* **and Gary Mavko**
Department of Geophysics, Stanford University
*iyyang@stanford.edu

Introduction

With the success of hydraulic fracturing and increasing popularity of basin modeling packages, there is an increasing need to understand the effects of hydrocarbon (HC) generation on the mechanical properties of source rocks. By evaluating these effects, we can establish relationships between geochemical and geomechanical parameters and potentially reduce the uncertainties associated with conventional and unconventional reservoir evaluation.

In this paper we present a simulation of fracture growth based on a three-dimensional source rock system. In the reference state, the system is composed of a shale matrix and kerogen solid; the kerogen is initially placed in the center of the system. Upon thermal maturation, the kerogen generates vapor and/or liquid products, most of which are HCs. The generated products exert excessive pore pressure due to volume expansion; this pressure is released through the expansion of pore volumes and formation of fractures. Assuming elastic deformation of each constituent within a framework of linear elastic fracture mechanics, our model calculates fracture sizes (length, aperture and volume) and the final pore pressure when fracture growth terminates. We validate this model using experimental observations, and find that the crack aperture estimate agrees closely with the results shown in Kobchenko et al. (2011). Finally, we ran the model for a geologic setting and concluded that the overpressure can result in submicron fractures with lengths 6 to 10 times larger than the original length-scale of the solid kerogen.

Methodology

In our model (Figure 1), the organic shale system is treated as a spherical pore of radius R embedded in a Vertical Transverse Isotropic (VTI) shale matrix. Initially, the pore space contains only kerogen and water, with volumetric fractions (1-S_w) and S_w, respectively, where S_w is the water saturation. The system is subjected to a far-field confining stress σ_0 normal to the bedding planes. We adopt the sign convention that a positive value represents a tensile stress; this means that $\sigma_0 < 0$. In most SEM images of organic pores (Lash and Engelder, 2005; Loucks et al., 2009), horizontal microcracks are dominant in the system despite the fact that vertical confining stress is usually thought to be the greatest. We interpret these images as indicating that the fracture toughness is anisotropic. It is possible to imagine a case where such anisotropies promote the propagation of the cracks along bedding planes (because the fracture toughness value is the lowest perpendicular to those planes). Under sufficient overpressure cracks are created and form an axisymmetric fracture plane with an axis of symmetry normal to the bedding planes.

The water in the pores has a pressure of p_H, which is sometimes, but not always, equal to hydrostatic pressure. As the kerogen matures, part of the pore space is taken up by HCs. Because the generated HC has a lower density than kerogen, overpressure $\Delta P = p_p - p_H$ is generated; this tends to expand the pore space and lead to the propagation of cracks. In our model, we assume pre-existing defects of length L_0 around the pore. These defects initially have zero aperture, but under excessive overpressure they can grow into fractures and create extra pore space. With more pore space to accommodate the HCs, overpressure drops and crack propagation eventually terminates.

The shale matrix is characterized by its drained Young's modulus E_{sh}, Poisson's ratio v_{sh}, and Mode I fracture toughness K_{Ic} across the bedding planes. The rock grain solid is characterized by its bulk modulus K_s. The kerogen and water in the pore space have bulk moduli of K_k and K_w, respectively. The bulk modulus of the HC varies between the laboratory and the geologic settings. In the laboratory, because of the elevated temperature (390˚C) and lack of confining stresses, generated HCs approximately follow the ideal gas law with $K_{HC} = P_p$. The total number of moles of HCs that can be generated per unit volume of kerogen, $n/V_{k,i}$, is specified by the chemical reaction of kerogen maturation. In geologic conditions, HCs are assumed to be in the liquid phase, with a constant bulk modulus of K_{HC}. Before the development of overpressure, in-situ kerogen and HCs have densities of $\rho_{k,i}$ and $\rho_{HC,i}$, respectively. The ratio, $D = \rho_{HC,i}/\ \rho_{k,i}$, is the volume expansion parameter in-situ associated with HC generation. The subscript i denotes the reference state where the system is subjected to confining stresses σ_0 from outside, and a pore pressure p_H from inside. Finally, the entire system is assumed to be impermeable.

Under laboratory conditions, $\sigma_0 = -1$ atm and $T = 390$˚C. Because free water has evaporated at such a temperature, the original volume of water in the pore space is taken up by void instead. K_w is thus irrelevant and $p_H = 1$ atm. Under the geologic condition, we would like to plot stresses and fracture sizes in terms of both the Transformation Ratio (TR) and geologic time, t. As a result, the magnitudes of σ_0, p_H and T increase linearly over geologic time due to assumed constant burial rate, S, and heating rate, H.

Modeling Results

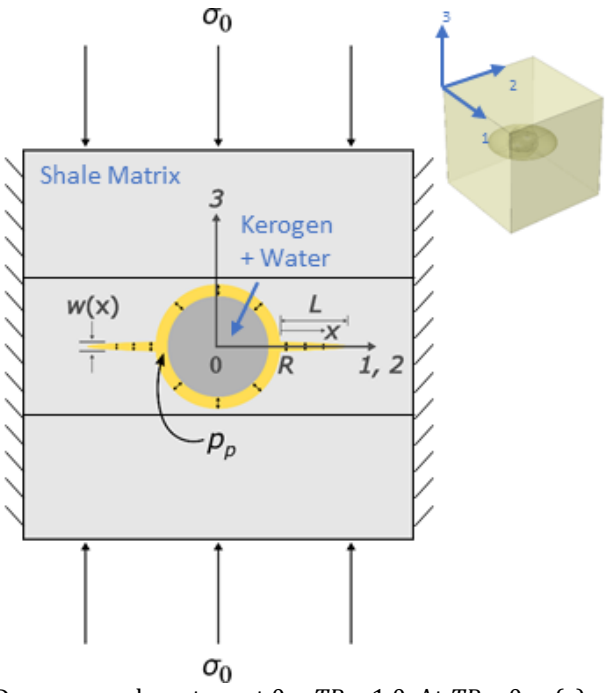

Figure 1: Side-view of the 3D source rock system at $0 < TR < 1.0$. At $TR = 0$, $w(x) = 0$ and the kerogen solid fills up all the pore space. At the end of thermal maturation, 30% of the kerogen solid remains in the system in the form of coke. At some $TR > 0$, the fracture reaches a final length of L, with a crack aperture profile $w(x)$. The associated overpressure at equilibrium is given by $\Delta P = p_p - p_H$. TR, transformation ratio.

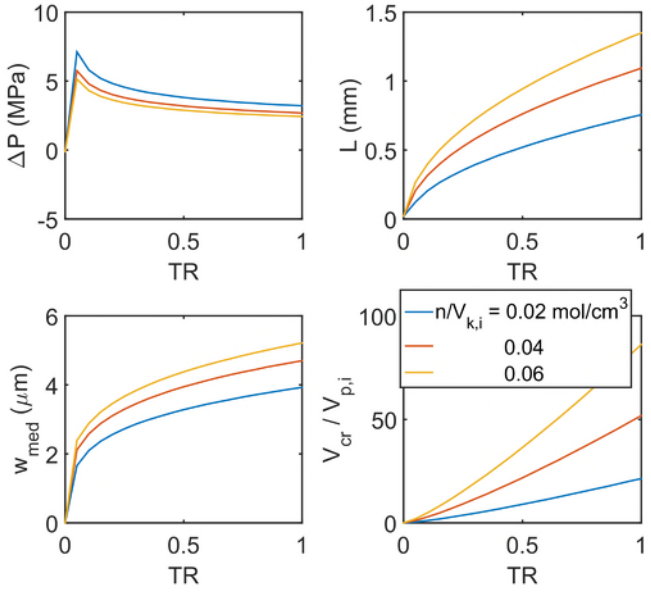

Figure 2: Parametric study of volume expansion parameter, $n/V_{k,i}$, in the laboratory conditions (T = 390°C, $p_H = -\sigma_0$ = 1 atm). Overpressure (upper left), crack length (upper right), median crack aperture (lower left) and crack volume normalized by initial pore volume (lower right) plotted against the Transformation Ratio (TR). Three curves with various $n/V_{k,i}$ ratios were plotted. R = 40 μm, and K_{Ic} = 0.10 MPa-m$^{1/2}$.

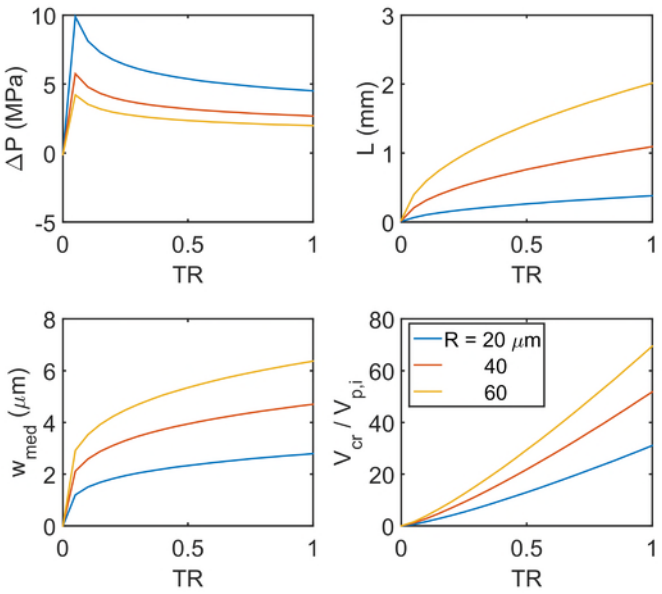

Figure 3: Parametric study of initial pore radius, R, in the laboratory conditions (T = 390°C, p_H = -σ_0 = 1 atm). Overpressure (upper left), crack length (upper right), median crack aperture (lower left) and crack volume normalized by initial pore volume (lower right) plotted against the Transformation Ratio (TR). Three curves with various R values were plotted. $n/V_{k,i}$ = 0.04 mol/cm^3, and K_{Ic} = 0.10 MPa-m$^{1/2}$.

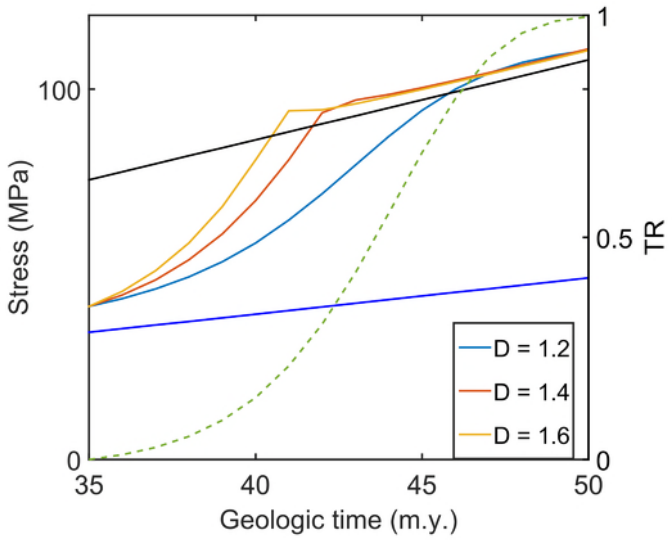

Figure 4: Stress history plotted against geologic time. The black line denotes the magnitude of lithostatic stress, $|\sigma_0|$; the blue line denotes the pore pressure pH in the reference state. Three curves with various volume expansion parameters, D, are also plotted to show changes in p_f over time. In all cases, pf starts near p_H and gradually increases, eventually exceeding $|\sigma_0|$. Larger D values cause pore pressure to build up more quickly, initiating crack propagation at earlier stage. For D = 1.4 and 1.6, fracture propagation occurs around 42 m.y. so that pf drops and follows the trend of $|\sigma_0|$ in later stages. The green dashed curve represents the Transformation Ratio of the kerogen over geologic time R = 40 μm, and K_{Ic} = 0.05 MPa-m$^{1/2}$.

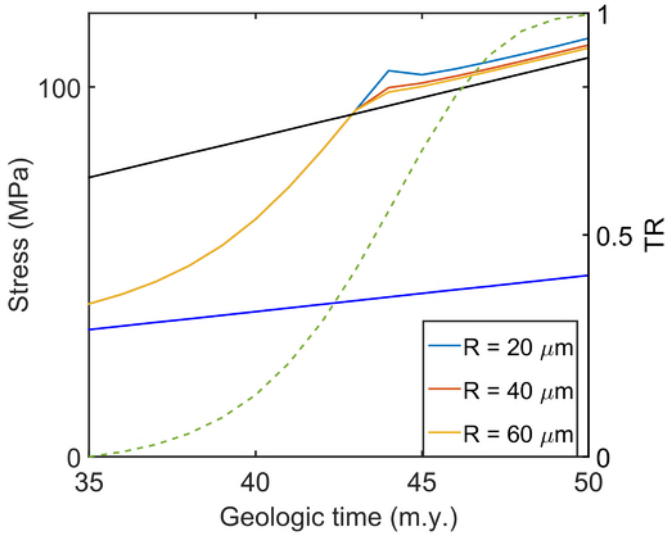

Figure 5: Stress history plotted against geologic time. The black line denotes the magnitude of lithostatic stress, $|\sigma_0|$; the blue line denotes the pore pressure p_H in the reference state. Three curves with different initial pore radii, R, show changes in p_f over time. In all cases, p_f starts near the p_H and gradually increases eventually exceeding $|\sigma_0|$. The smaller pore withstands higher p_f than the larger pores, but the difference is not significant. The green dashed curve represents the Transformation Ratio of the kerogen over geologic time. D = 1.3, and K_{Ic} = 0.05 MPa-m$^{1/2}$.

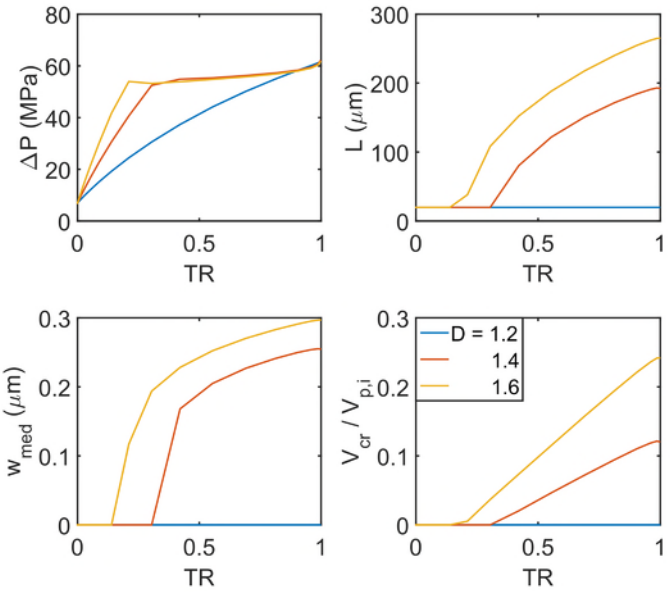

Figure 6: Parametric study of the kerogen-to-HC density ratio, D, in the geologic conditions ($|\sigma_0|$ and p_H shown in Figure 5, T follows a thermal gradient H = 2.5°C/m.y. and T_0 = 25°C). Overpressure (upper left), crack length (upper right), median crack aperture (lower left) and crack volume normalized by initial pore volume (lower right) plotted against the Transformation Ratio (TR). Three curves with various D values are plotted. R = 40 μm, and K_{Ic} = 0.05 MPa-m$^{1/2}$.

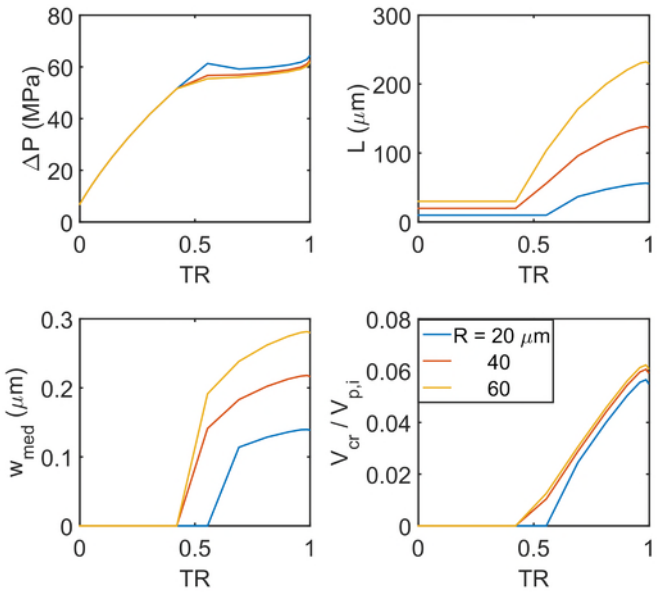

Figure 7: Parametric study of the initial pore radius, R, in the geologic conditions ($|\sigma_0|$ and p_H shown in Figure 6, T follows a thermal gradient H = 2.5°C/m.y. and T_0 = 25°C). Overpressure (upper left), crack length (upper right), median crack aperture (lower left) and crack volume normalized by initial pore volume (lower right) plotted against the Transformation Ratio (TR). Three curves with various R values are plotted. K_{Ic} = 0.05 MPa-m$^{1/2}$, and D = 1.3.

Table 1: Parameters for the simulation.

Parameter	Variable	Value	Reference
Parameters for laboratory setting			
Ambient temperature	T	390°C	Kobchenko et al. (2011)
Confining stress	σ_0	-0.1 MPa	Kobchenko et al. (2011)
Water (Void) saturation	S_w	0.05	
Total Organic Carbon (TOC)	TOC	10 wt.%	Kobchenko et al. (2011)
Bulk modulus of kerogen	K_k	0.83 GPa	Zeszotarski et al. (2004)
Bulk modulus of rock grains	K_s	3.90 GPa	Mavko et al. (2009)
Drained Young's modulus of shale	E_{sh}	1.00 GPa	Closmann et al. (1979)
Drained Poisson's ratio of shale	ν_{sh}	0.30	Chong et al. (1980)
Density ratio of shale to kerogen	$\rho_{sh,i}/\rho_{k,i}$	2.0	
Initial defect length	L_0	$0.5R$	
Parameters for geologic setting			
Activation energy of kerogen	E_a	52 kcal/mol	Burnham (2015)
Pre-exponential factor	A	7×10^{13} s^{-1}	Peters et al. (2016)
Surface temperature	T_0	25°C	
Sedimentation rate	S	100 m/m.y.	
Heating rate	H	2.5°C/m.y.	
Average overburden density	ρ_{ob}	2200 kg/m^3	
Water density	ρ_w	1000 kg/m^3	
Water saturation	S_w	0.05	
Total Organic Carbon (TOC)	TOC	10 wt.%	Kobchenko et al. (2011)
Bulk modulus of hydrocarbon	K_{HC}	0.68 GPa	Mavko et al. (2009)
Bulk modulus of water	K_w	2.73 GPa	Mavko et al. (2009)

Bulk modulus of kerogen	K_k	3.32 GPa	Zeszotarski et al. (2004)
Bulk modulus of rock grains	K_s	15.6 GPa	Mavko et al. (2009)
Drained Young's modulus of shale	E_{sh}	4.00 GPa	Closmann et al. (1979)
Drained Poisson's ratio of shale	ν_{sh}	0.30	Chong et al. (1980)
Density ratio of shale to kerogen	$\rho_{sh,i}/\rho_{k,i}$	2.0	
Initial defect length	L_0	$0.5R$	

Summary and Conclusions

We present an organic shale model that predicts the fracture growth and pore pressure changes during the process of kerogen thermal maturation. This model is primarily based on elasticity and LEFM. By running the simulation under laboratory conditions, we obtained similar crack aperture ranges to those measured by Kobchenko et al. (2011). Secondary porosity generated by crack opening is significant under laboratory conditions: the induced fracture planes can accommodate several times of the initial pore volume. In contrast, under geologic conditions, no significant secondary porosity is generated through the crack opening. If the kerogen-to-HC density ratio is high enough, fractures can propagate, but the extent of propagation and resulting apertures are much smaller than those generated under laboratory condition due to the stress exerted by the overburden. Parametric studies show that the volume expansion parameter ($n/V_{k,\mathrm{i}}$ ratio or D), initial pore size, and fracture toughness of the shale matrix all have major effects on the final fracture sizes and pore pressures in varying degrees.

It should be noted that we have assumed VTI for the shale matrix with the underlying assumption that the fracture toughness is lower across the layers of bedding planes, which makes fracture propagation along those planes favorable. If the mechanical parameters that characterize the shale matrix across the bedding planes vary, we should expect different results for final fracture size and pore pressure because they are directly involved in the calculation of crack aperture. A compilation of mechanical properties measured in oil shales can be found in Eseme et al. (2007).

The shale matrix is assumed to be impermeable throughout the kerogen thermal maturation. If permeability were allowed we would expect the pore pressure to decrease over time and eventually equilibrate with hydrostatic pore pressure. In order to maintain the fracture opening after the drop in pore pressure associated with fluid flow, inelastic deformation in the shale matrix must take place. This would need to be taken into account by more comprehensive modeling of the mechanical evolution of host rocks during the thermal maturation of kerogen.

References

Burnham, A. K. (2015). A simple kinetic model of oil generation, vaporization, coking, and cracking. Energy & Fuels 29 (11), 7156-7167.

Chong, K., K. Uenishi, J. Smith, and A. Munari (1980). Non-linear three dimensional mechanical characterization of Colorado oil shale. In International Journal of Rock Mechanics and Mining Sciences & Geomechanics Abstracts, Volume 17, pp. 339-347. Elsevier.

Closmann, P., W. Bradley, et al. (1979). The effect of temperature on tensile and compressive strengths and young's modulus of oil shale. Society of Petroleum Engineers Journal 19 (05), 301-312.

Eseme, E., Urai, J. L., Krooss, B. M., & Littke, R. (2007). Review of mechanical properties of oil shales: Implications for exploitation and basin modelling. Oil Shale, 24(2), 159-175.

Kobchenko, M., H. Panahi, F. Renard, D. K. Dysthe, A. Malthe-Sørenssen, A. Mazzini, J. Scheibert, B. Jamtveit, and P. Meakin (2011). 4D imaging of fracturing in organic-rich shales during heating. Journal of Geophysical Research: Solid Earth 116 (B12).

Lash, G. G. and T. Engelder (2005). An analysis of horizontal microcracking during catagenesis: Example from the catskill delta complex. AAPG Bulletin 89 (11), 1433-1449.

Loucks, R. G., Reed, R. M., Ruppel, S. C., & Jarvie, D. M. (2009). Morphology, genesis, and distribution of nanometer-scale pores in siliceous mudstones of the Mississippian Barnett Shale. Journal of sedimentary research, 79(12), 848-861.

Mavko, G., Mukerji, T., & Dvorkin, J. (2009). The rock physics handbook: Tools for seismic analysis of porous media. Cambridge university press.

Peters, K., A. Burnham, and C. Walters (2016). Petroleum generation kinetics: Single versus multiple heating-ramp open-system pyrolysis: Reply. AAPG Bulletin 100 (4), 690-694.

Zeszotarski, J. C., Chromik, R. R., Vinci, R. P., Messmer, M. C., Michels, R., & Larsen, J. W. (2004). Imaging and mechanical property measurements of kerogen via nanoindentation. Geochimica et Cosmochimica Acta, 68(20), 4113-4119.

GEOCHEMICALLY DISTINCT OIL FAMILIES IN THE MIDDLE MAGDALENA VALLEY, COLOMBIA

William Thompson-Butler[1,*], Kenneth E. Peters[1, 2], Leslie B. Magoon[1], Allegra Hosford Scheirer[1], and Stephan A. Graham[1]
[1]Department of Geological Sciences, Stanford University
[2]Schlumberger
[*]rthomps@stanford.edu

Introduction

The Middle Magdalena Valley (MMV) is an intermontane basin and petroleum province in northwestern Colombia located between the Central and Eastern Cordilleras of the Andes Mountains. During the Cretaceous, restricted marine conditions within a broad foreland basin that included the MMV resulted mainly in deposition of organic-rich carbonate and siliciclastic sediments. The Upper Cretaceous La Luna Formation is the primary regional source rock (e.g., Zumberge, 1984, Ramon and Dzou, 1999), but other source rocks may contribute. This study uses chemometrics (multivariate statistics) of source-related biomarker and isotopic ratios for 96 crude oil and rock extract samples from the MMV to establish distinct oil families and infer their source rock depositional environment, lithology, and organic matter type.

Geochemical data for the samples were provided by GeoMark Research, Inc. and were analyzed using laboratory methods described in Peters et al. (2007). Source rock extracts and highly mature or biodegraded oils were excluded at this stage to yield a training set of 67 samples. The parameters selected for the chemometric analysis include one porphyrin ratio (V/Ni), fourteen terpane ratios (C_{19}/C_{23}, C_{22}/C_{21}, C_{24}/C_{23}, C_{26}/C_{25}, Tet/C_{23}, C_{27}T/C_{27}, C_{28}/H, C_{29}/H, C_{30}X/H, Ol/H, C_{31}R/H, Ga/C_{31}R, Ts/Tm and C_{35}S/C_{34}S), five sterane ratios (Ster/Terp, Rearr/Reg, %C_{27}, %C_{28}, and %C_{29}), and three stable carbon isotope ratios (canonical variable, $\delta^{13}C_{aromatics}$ and $\delta^{13}C_{saturates}$). These 23 source-related parameters were used to construct a hierarchical cluster analysis (HCA) dendrogram, which defines five oil tribes within the study area. The tribes may originate from different source rocks or organofacies of the same source rock (e.g., La Luna Formation) and they show systematic distributions by map location (Figure 1) and reservoir age (Figure 2). Tribes 1 through 3 are from Paleogene reservoir rocks in the south to central portion of the study area. Tribes 4 and 5 on the other hand are from Cretaceous to early Paleogene reservoir rocks in the northern portion of the study area.

The source-related biomarker and isotopic ratios are used to infer differences in organic matter type and source rock depositional environment between the oil tribes. All five tribes show stable carbon isotope ratios for saturate and aromatic hydrocarbons that indicate marine organic matter based on the Sofer (1984) diagram. Terpane ratios (C_{22}/C_{21}, C_{24}/C_{23}, C_{31}R/H, and C_{29}/H) suggest marine shale to marine carbonate source rocks for the oil samples (Peters et al., 2005). Tribes 1 and 2 show mainly a marine shale source rock, with marine shale to marine carbonate for Tribe 3 and marine marl to carbonate for Tribes 4 and 5. Dibenzothiophene/phenantrene (DBT/P) and pristane/phytane (Pr/Ph) ratios

support these interpretations. Finally, C_{27} diasterane/regular sterane and Ts/Tm ratios indicate that Tribe 5 is more thermally mature than Tribes 1 through 4.

In conclusion, chemometric analysis of 23 source-related biomarker and carbon isotope parameters has been used to identify 5 distinct oil tribes within the MMV. In addition, inferences on source rock depositional environment, lithology, and organic matter type for each tribe can be made. More work is needed to identify the specific source rocks for the oil tribes defined in this study. Further chemometric analyses such as alternating least squares to concentration (ALS-C) performed on the current dataset can help identify end members from mixtures on the HCA dendrogram. Additional geochemical analyses performed on a new oil dataset provided by Ecopetrol and PSI can help expand the study and address new questions as well.

References

Peters, K. E., L. S. Ramos, J. E. Zumberge, Z. C. Valin, C. R. Scotese, and D. L. Gautier, 2007, Circum-Arctic petroleum systems identified using decision-tree chemometrics: AAPG Bulletin, v. 91, no. 6, p. 877-913.

Peters, K. E., C. C. Walters, and J. M. Moldowan, 2005, The biomarker guide: Cambridge, UK, Cambridge University Press, 1155 p.

Ramon, J. C., and L. I. Dzou, 1999, Petroleum geochemistry of the Middle Magdalena Valley: Colombia: Organic Geochemistry, v. 30, p. 249-266.

Sofer, Z., 1984, Stable carbon isotope compositions of crude oils: Application to source depositional environments and petroleum alteration: AAPG Bulletin, v. 68, no. 1, p. 31-49.

Zumberge, J. E., 1984, Source rocks of the La Luna Formation (Upper Cretaceous) in the middle Magdalena Valley, Colombia: Petroleum Geochemistry and Source Rock Potential of Carbonate Rocks (Palacas J. C., ed.), AAPG Studies in Geology #18, p. 127-133.

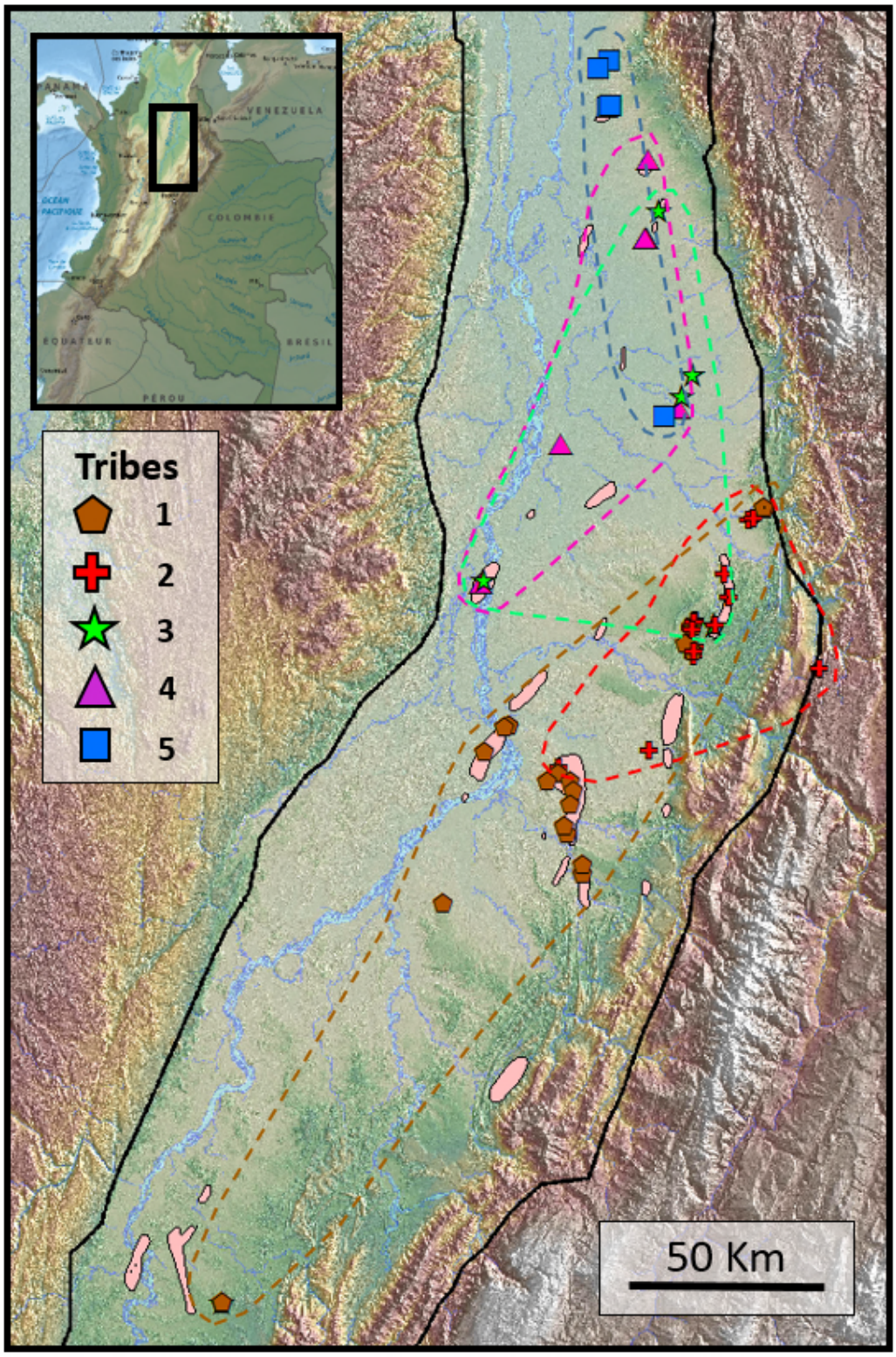

Figure 1: The geographic distribution and tribe identity of oil samples as defined by hierarchical cluster analysis. Dashed lines indicate the full extent of each tribe. Generalized primary oil field locations given by pink polygons.

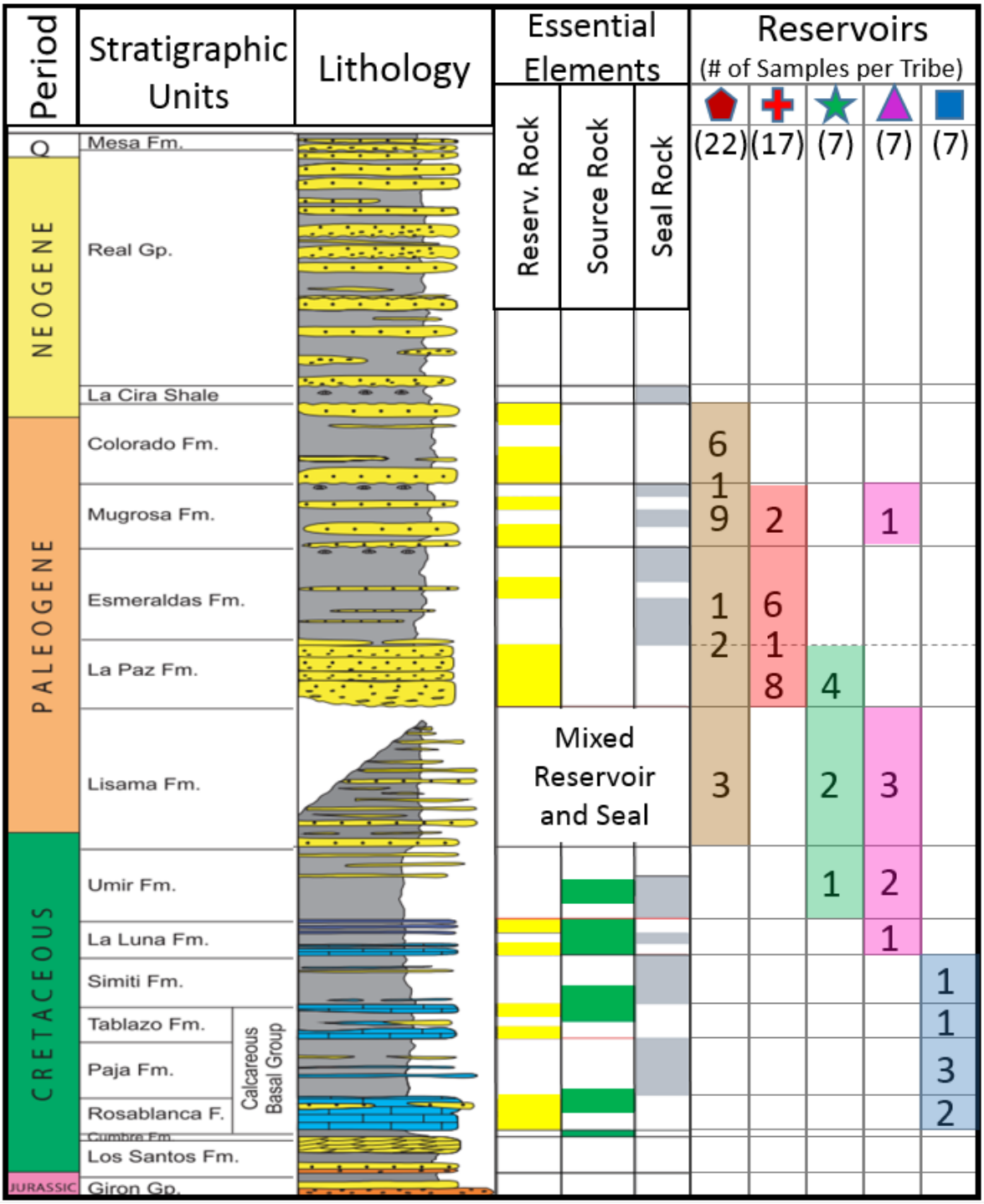

Figure 2: Stratigraphic column for the Middle Magdalena Valley illustrating the distribution of reservoir rocks for the oil samples from each Tribe. Values indicate the number of samples from a specific reservoir and values in between reservoirs indicate that multiple reservoirs were listed for those samples. 67 samples were included in the HCA however reservoir rock information was not included for every sample. Locations of petroleum system elements are approximate. Modified from ANH, 2007.

TOWARDS A BASIN & PETROLEUM SYSTEM MODEL FOR THE PEGASUS BASIN, NEW ZEALAND

Zachary F. M. Burton[1,*], J. Michael Moldowan[1,2], Kristian E. Meisling[1], Stephan A. Graham[1]
[1]*Department of Geological Sciences, Stanford University*
[2]*Biomarker Technologies, Inc., Rohnert Park, CA*
[3]*Schlumberger*
[*]zburton@stanford.edu

Introduction

Presence of onshore oil seeps, gas shows in shallow wells, and direct hydrocarbon indicators from seismic data provide evidence for active petroleum systems in the East Coast Province of New Zealand. The East Coast Basin alone is associated with over 300 onshore oil and gas seeps (Uruski, 2010). However, despite over a century of exploration efforts, the petroleum systems of the East Coast Basin remain poorly understood, and the characteristics of its offshore extensions, the Pegasus and Raukumara basins, are even less understood (Uruski, 2010).

This study will focus on the frontier Pegasus Basin, and will leverage the integration of oil seep and outcrop analogue geochemistry with seismic stratigraphy to constrain source rock, reservoir rock, and seal characteristics and extent. Insight and data garnered from geochemical and seismic analysis will provide input for utilization of basin and petroleum system modeling to address questions of generation (volume, timing), migration (with a focus on identifying basin-scale migration pathways), and accumulation.

The key objectives of this study are to:

(1) Make an oil-source rock correlation for those oil seeps inferred to be sourced from the Pegasus and East Coast basins
Motivation: Seeps share characteristics most diagnostic of the Whangai Fm., yet no oil-prone organofacies has been identified within this formation (Sykes et al., 2012)

(2) Identify and map out packages of probable reservoir
*Motivation: A*ll three deep wells drilled in the East Coast Basin had gas shows, but a lack of quality reservoir meant no commercial accumulations were found; Uruski & Bland, 2011), and

(3) Identify petroleum migration pathways within the basin
Motivation: Onshore seeps are proof of an active petroleum system, yet migration to these seeps from the pod of active source rock is poorly understood

Background

The Pegasus Basin of New Zealand lies east of Cook Straight, north of Chatham Rise, and southeast of the Hikurangi margin. It covers some 25,000 km^2 (seismic-based estimate; Bland et al., 2015) to 50,000 km^2 (gravity-based estimate; Uruski, 2010), and contains water depths <1,000 m to >3,000 m, with a significant portion of the basin at water depths

>2000 m (Bland et al., 2015). Overall sediment thickness is >5 s TWT (Uruski, 2010), estimated to represent anywhere from 6 to 9km (Bland et al., 2013; Bland et al., 2015).

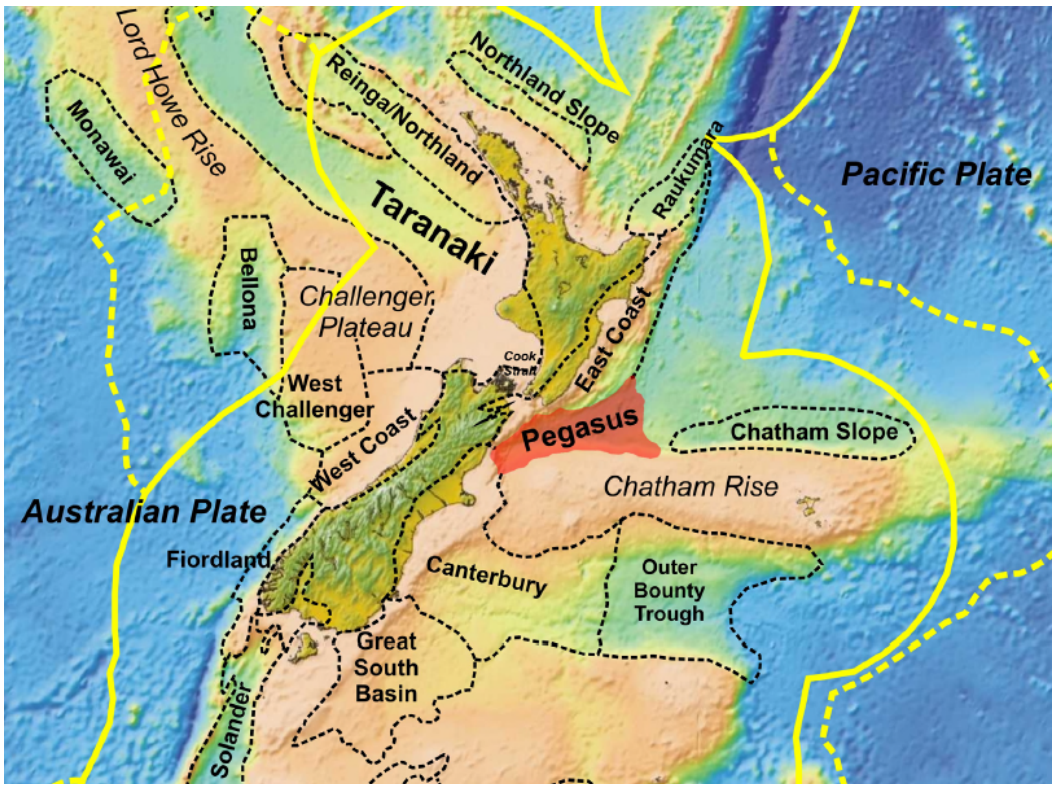

Figure 1. Sedimentary basins of New Zealand. Pegasus Basin represented by orange polygon. Adapted from Uruski & Bland, 2011.

Depositional history

Sediment fill in the Pegasus Basin overlies a basement [Fig. 2, "A," below] comprised of Jurassic to Early Cretaceous metasedimentary rock of the Torlesse Composite Terrane (Bland et al., 2015) and Early Cretaceous igneous rock of the Hikurangi Plateau (Davy et al., 2008). Earliest sediment fill is inferred to have been deposited starting in the late Early Cretaceous (Bland et al., 2015), coincident with the cessation of subduction of the Hikurangi Plateau beneath the Chatham Rise of Gondwana (Davy, 2014). Once subduction ceased, a prolonged (~50 to 75 Myr long) passive margin phase resulted in low rates of sedimentation and minimal tectonic activity [Fig. 2, "B," below] within the Pegasus and East Coast basins (Bland et al., 2015; Salazar et al., 2015). Initiation of a second phase of Hikurangi Plateau subduction, and formation of the modern Hikurangi margin, began ~30-24 Ma (Nicol et al., 2007). Though the passive margin, pre-Neogene depositional history [Fig. 2, "B," below] of the Pegasus and East Coast basins is similar, the migration of the newly activated Hikurangi margin resulted in a high degree of deformation in the East Coast Basin but left the Pegasus Basin relatively undeformed, and thus, structurally simple in nature. Lithospheric flexure associated with subduction along the Hikurangi margin created accommodation space in the Pegasus Basin (Bland et al., 2015). Inception of the

Alpine Fault coincided with the initiation of subduction ~24 Ma (Kamp, 1986), and fault movement and subduction-associated orogenic uplift led to increased rates of erosion and thus delivery of Neogene sediments to fill this accommodation space (Adams, 1981). Uplift of the Southern Alps contributed to accelerated deposition beginning ~10 Ma (Adams, 1981). Neogene deposition [Fig. 2, "C," below], which is inferred to account for the majority of sediment thickness in Pegasus Basin, was likely dominated by sources to the west (southern North Island; Wairarapa Region) and sources to the southwest (northern South Island; Marlborough Region and the Southern Alps) (Bland et al., 2015).

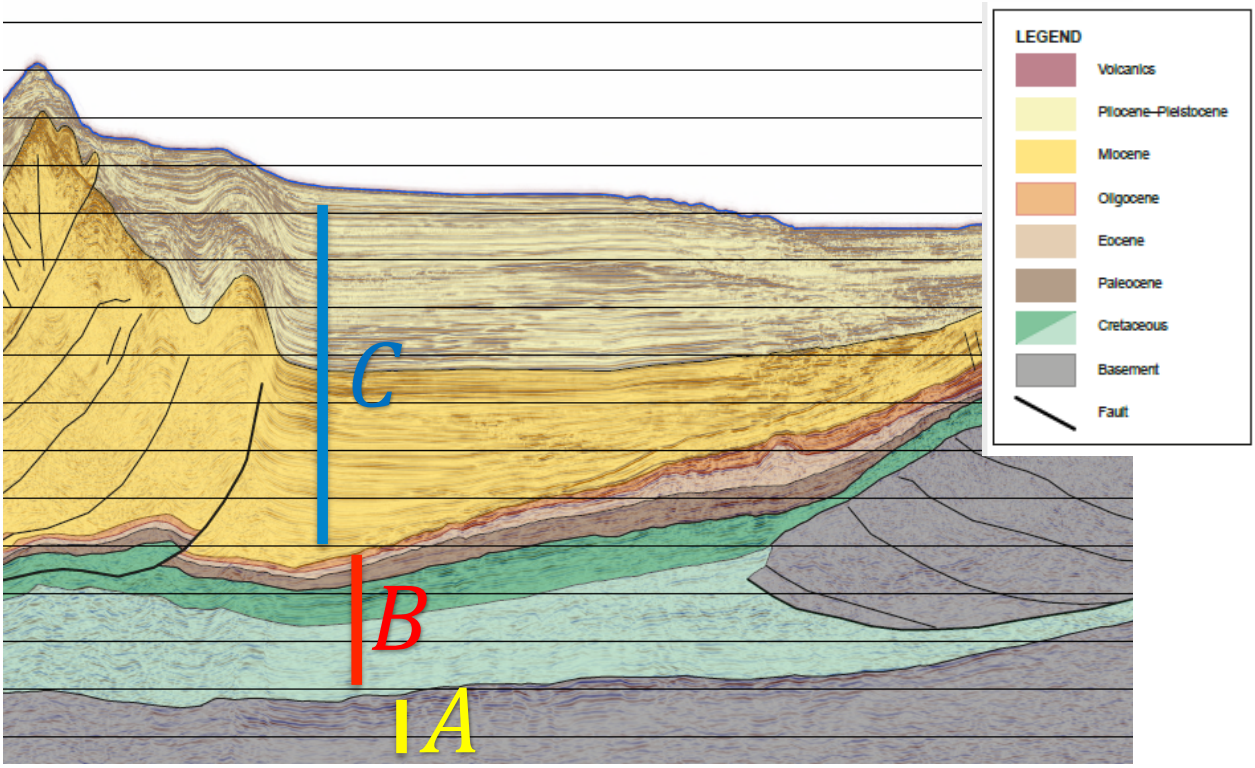

Figure 2. Panel from seismic line PEG09-17 with interpretations by Bland et al., 2013. "A" denotes basement, "B" indicates thin Cretaceous through Oligocene passive margin deposits, and "C" represents the thick Neogene succession.

Source Rock

Early Cretaceous to Paleocene shales are the most likely candidates for viable source rock in the basin, both based on organofacies and depth of burial necessary for maturation (Uruski & Bland, 2011). Uruski & Bland (2011) speculate about an Early Cretaceous marine source rock (e.g., Glenburn Formation turbidite sands with terrestrially-derived 2 wt.% TOC), however, the Whangai Formation shale of Late Cretaceous to Paleocene age and the Waipawa Formation black shale of Late Paleocene (Thanetian) age are most commonly invoked as potential source rocks (Schiøler et al., 2010; Uruski & Bland, 2011; Hollis et al., 2014). Both the Whangai and the Waipawa, which conformably overlies the Whangai (Leckie et al., 1995), were deposited during the passive margin phase of

Pegasus, East Coast, and Raukumara Basin sedimentation, likely in cool, marine settings (Leckie et al., 1995; Hollis et al., 2014). These formations have TOCs of 0.5-1.5wt.% in areas (Whangai Fm.; Uruski & Bland, 2011) to 0.5-12.0 wt.% (Waipawa Fm.; Hollis et al., 2014).

Reservoir Rock

Turbidites within the thick Neogene succession are inferred to represent potential reservoir. The Titihaoa-1 well in the East Coast Basin encountered Middle Miocene turbidite sands with porosities up to 23% (Uruski & Bland, 2011), however, despite gas shows in all three deeper East Coast Basin wells, no quality reservoir has been identified. Though it is important to recall that the Pegasus Basin is likely characterized by a different post-Oligocene depositional history than the East Coast Basin, insight gained into reservoir characteristics in the relatively undeformed Pegasus Basin will shed light on challenges encountered so far in the East Coast Basin.

Seal Rock

A number of candidates for an effective seal are inferred for the Pegasus Basin. These include the finding that East Coast Basin turbidites encountered both in wells and in outcrop contain up to 75% intra-formational mudstone (Uruski & Bland, 2011), the hypothesis that marls may provide a regional seal (Darby, 2002), and the fact that gas hydrates may have local sealing ability (Grauls et al., 1999; Grauls, 2001; Uruski & Bland, 2011).

References

Adams, C. J. (1981). Uplift rates and thermal structure in the Alpine fault zone and Alpine schists, Southern Alps, New Zealand. *Geological Society, London, Special Publications*, *9*(1), 211-222.

Bland, K.J., Hill, M.G., Strogen, D.P., Bache, F., Barker, D. H. N., Bull, S., Davy, B.W., & Sahoo, T. R. (2013). New Zealand National Seismic Framework: Reinga-Northland, Taranaki, Canterbury, Great South, Bounty Trough, and Pegasus-East Coast-Raukumara basins. *GNS Science consultancy report* 2013/254.

Bland, K. J., Uruski, C. I., & Isaac, M. J. (2015). Pegasus Basin, eastern New Zealand: A stratigraphic record of subsidence and subduction, ancient and modern. *New Zealand Journal of Geology and Geophysics*, 58(4), 319-343.

Darby, D. (2002). Seal properties, overpressure and stress in the Taranaki and East Coast Basins, New Zealand. *In 2002 New Zealand Petroleum Conference proceedings* (pp. 24-27).

Davy, B., Hoernle, K., & Werner, R. (2008). Hikurangi Plateau: Crustal structure, rifted formation, and Gondwana subduction history. *Geochemistry, Geophysics, Geosystems*, 9(7).

Davy, B. (2014). Rotation and offset of the Gondwana convergent margin in the New Zealand region following Cretaceous jamming of Hikurangi Plateau large igneous province subduction. *Tectonics*, 33(8), 1577-1595.

Grauls, D., Blanche, J. P., & Poudre, J. L. (1999). Sealing Efficiency of Gas Hydrates from Seismic AVO and Hydromechanical Approaches. *Proceedings Gas Habitats of SE Asia and Australasia Conference*: Abstract.

Grauls, D. (2001). Gas hydrates: importance and applications in petroleum exploration. *Marine and Petroleum Geology*, 18(4), 519-523.

Hollis, C. J., Tayler, M. J., Andrew, B., Taylor, K. W., Lurcock, P., Bijl, P. K., Kulhanek, D.K., Crouch, E. M., Nelson, C. S., Pancost, R. D., Huber, M., Wilson, G. S., Ventura, G. T., Crampton, J. S., Schiøler, P., & Phillips, A. (2014). Organic-rich sedimentation in the South Pacific Ocean associated with Late Paleocene climatic cooling. *Earth-Science Reviews*, *134*, 81-97.

Kamp, P. J. (1986). The mid-Cenozoic Challenger Rift System of western New Zealand and its implications for the age of Alpine fault inception. *Geological Society of America Bulletin*, *97*(3), 255-281.

Leckie, D. A., Morgans, H., Wilson, G. J., & Edwards, A. R. (1995). Mid-Paleocene dropstones in the Whangai Formation, New Zealand—evidence of mid-Paleocene cold climate?. *Sedimentary Geology*, *97*(3), 119-129.

Nicol, A., Mazengarb, C., Chanier, F., Rait, G., Uruski, C., & Wallace, L. (2007). Tectonic evolution of the active Hikurangi subduction margin, New Zealand, since the Oligocene. *Tectonics*, *26*(4).

Salazar, M. U., Francis, M., Brink, G., Guerra, I., & Hayo, K. (2015). Newly Acquired 2D Seismic Data Gives Insights into Prospectivity and Play Types of the Pegasus and East Coast Basins, New Zealand. *In SEAPEX Exploration Conference 2015.*

Schiøler, P., Rogers, K., Sykes, R., Hollis, C. J., Ilg, B., Meadows, D., Roncaglia, L., & Uruski, C. (2010). Palynofacies, organic geochemistry and depositional environment of the Tartan Formation (Late Paleocene), a potential source rock in the Great South Basin, New Zealand. *Marine and Petroleum Geology*, *27*(2), 351-369.

Sykes, R., Zink, K. G., Rogers, K. M., Phillips, A., & Ventura, G. T. (2012). New and updated geochemical databases for New Zealand petroleum samples, with assessments of genetic oil families, source age, facies and maturity. *GNS Science Consultancy Report 2012*, *37*, 29.

Uruski, C. I. (2010). New Zealand's deepwater frontier. *Marine and Petroleum Geology*, 27(9), 2005-2026.

SEISMIC CHARACTERIZATION OF THE SHUBLIK FORMATION, ALASKA NORTH SLOPE, FOR IMPROVED BASIN AND PETROLEUM SYSTEM MODELING

Mustafa Al Ibrahim[1,*], Tapan Mukerji[1], and Allegra Hosford Scheirer[2]
[1]*Department of Earth Resources Engineering, Stanford University*
[2]*Department of Geological Sciences, Stanford University*
[*]malibrah@stanford.edu

Geochemical input parameters, such as total organic content (TOC) and hydrogen index (HI) are important in obtaining realistic basin and petroleum system models. Data for these parameters is generally scarce and restricted to well locations. However, basin modeling requires these parameters to be defined on a regional scale. Seismic data have been extensively used in the past to characterize different types of heterogeneities at large scale. Success depends on the complexity of the studied rocks because the elastic signature measured by seismic is a function of the type and amount of constituent minerals, fluids, organic matter, and pore pressure. This study documents preliminary work on characterizing the Shublik source rock geochemical heterogeneity from seismic data from the Alaska North Slope.

In this part of the study, geochemistry data from two wells are used as calibration to estimate the present day TOC from the 3D seismic cube. Unfortunately, the wells lie on the edge of the seismic survey. However, these specific wells do provide a rich geochemical dataset that is needed in the analysis (see abstract by Inessa Yurchenko, this volume). Four horizons corresponding to the Top Kingak Shale, Lower Kingak Shale, Shublik Formation, and Ivishak Formation are interpreted from seismic data. Faults are observed crossing all the studied formations suggesting they have an origin at least as young as the top of the Kingak Shale (~145 Ma). Moore and Box (2016) summarized the tectonic history of Alaska North Slope and noted that the early Brookian orogeny (Late Jurassic and early Cretaceous) characterizes the deformation observed in the Northern domain of Alaska. The timing of the observed faults coincides with this tectonic episode.

Seismic impedance cubes are estimated from post stack time migrated seismic data. To accomplish that, a constant phase wavelet is extracted from a 200 ms window centered on the top of the Shublik Fm. with a dominant frequency of about 12 Hz. Model based inversion is applied on both mid (15°-30°) and far (30°-45°) offset partial stacks to obtain an estimate of P-wave impedance and elastic impedance, respectively. Inversion results (Figure 1) show that impedance variations do not follow the interpreted structure suggesting that variations observed might be linked to depositional or diagenetic processes.

To correlate the results of seismic inversion to total organic content, well logs and pyrolysis analysis results are used to build a model between P-impedance, S-impedance, and TOC. The total organic content in this dataset cannot be distinguished solely from gamma ray or P-impedance. Using both S-impedance and P-impedance is important in identifying TOC values higher than 2% in impedance space (Figure 2). A support vector machine model with a Gaussian kernel (e.g., Hastie et al., 2009) was used to obtain a misclassification percentage of 8.8% (Figure 3). A probability map of TOC larger than 2% is

then calculated using this model (Figure 4). The probability map can be used to create different realizations of TOC maps, which can in turn be used to explore parameter space for that important input in basin modeling.

The study showed that it is possible to distinguish rocks with high TOC in the Shublik Fm with this workflow. Validation is ongoing. Future work includes 1) incorporating automated and manual classification of facies into the workflow in attempt to separate different lithologies and build a separate TOC prediction model for each lithology, 2) building rock physics templates that incorporate organic matter to constrain the classification, and 3) studying the viability of using the method for estimating other parameters such as the hydrogen index.

References

Moore, T. E., and Box, S. E., 2016, Age distribution and style of deformation in Alaska north of 60°N: Implications for assembly of Alaska, Tectonophysics, in press, 38 p.

Acknowledgements

The authors thank Great Bear Petroleum for permission to use 3D seismic data for this study.

Figures

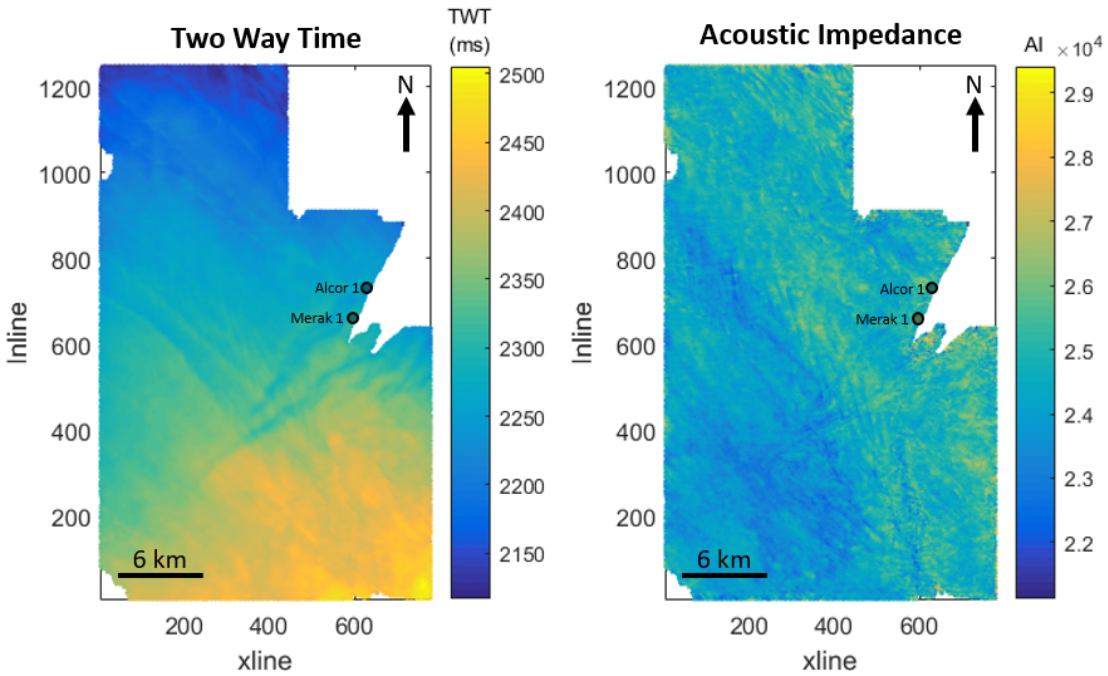

Figure 1. Two-way travel time and inverted acoustic impedance for the top of the Shublik Formation. Note that the structural trend does not correspond to the variations observed in the acoustic impedance.

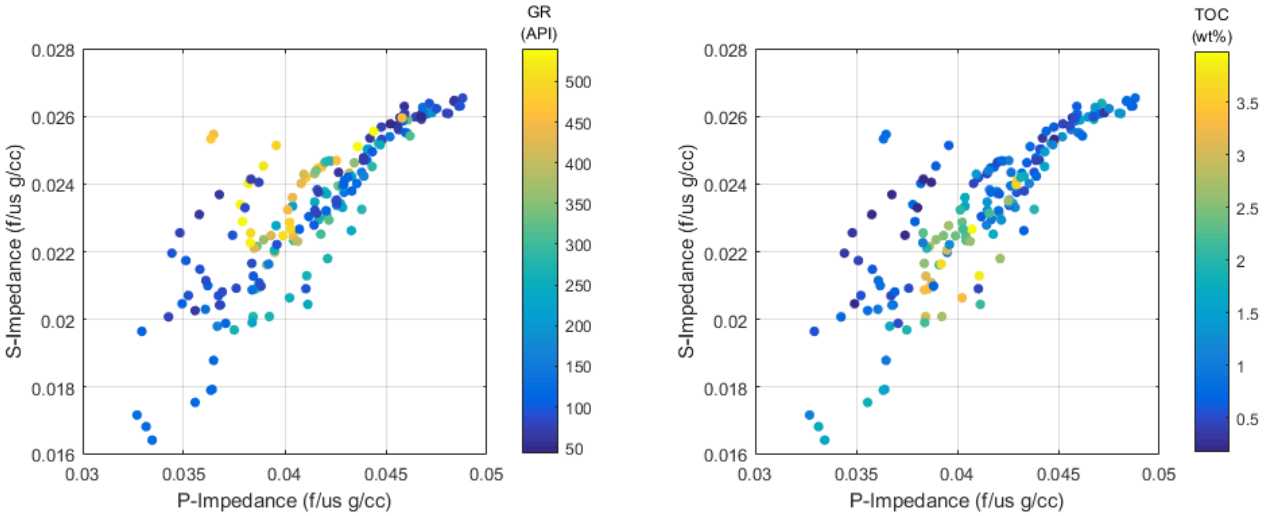

Figure 2. Compressional (P) and shear (S) impedance cross plots calculated from wells in the Shublik Formation. Note that the highest TOC does not correspond to the highest gamma ray (GR) values.

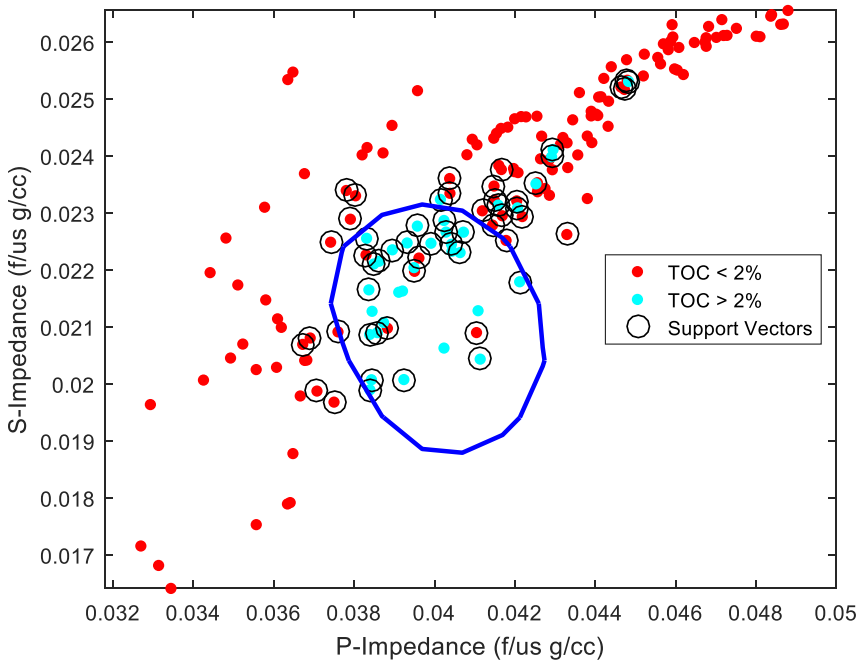

Figure 3. Support vector machine (SVM) with a Gaussian kernel classification boundary (blue line). Out of sample misclassification rate is 8.8%.

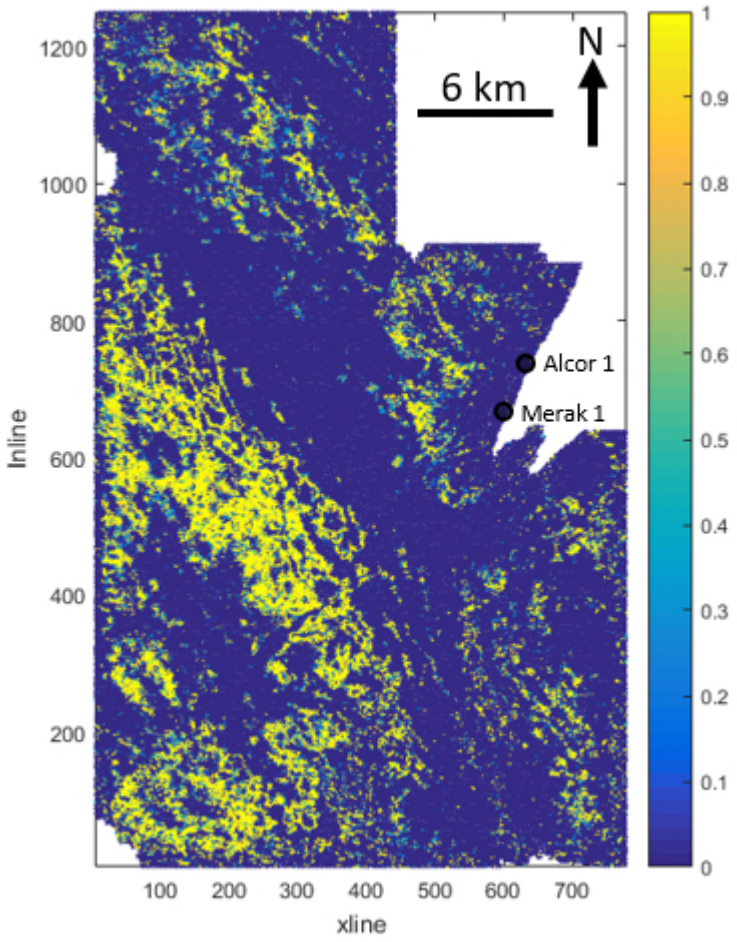

Figure 4. Probability of having TOC values higher than 2% at the top of the Shublik Formation.

BASIN-SCALE GEOMECHANICS OF POROPLASTICITY AND ITS INFLUENCE ON PREDICTING STRESS-STRAIN BEHAVIORS AND OVERPRESSURE GENERATION THROUGH GEOLOGIC TIME

Laainam Chaipornkaew[1,*], Tapan Mukerji[2], Stephan A. Graham[1], Noelle Schoellkopf[1,3], and Allegra Hosford Scheirer[1]

[1]*Department of Geological Sciences, Stanford University*

[2]*Department of Energy Resources Engineering, and of Geophysics, Stanford University*

[3]*Schlumberger*

[*]bestc@stanford.edu

Basin and petroleum system modeling (BPSM) simulates among other things, the stress history in sedimentary basins, which allows testing of different scenarios of overpressure development. Conventional 1D models apply Terzaghi's principle, which only approximates porosity compaction via vertical effective stress. However, this conventional approach is overly simplified for complex tectonic regimes. In certain tectonics regimes, horizontal stress significantly exceeds vertical overburden stress and thus it becomes the dominant force in driving deformation of porous material. In such cases, a poroelastic model is suitable where partial differential equations (PDEs) coupling deformation and fluid flow are solved for full stress and strain tensors. However, a poroelastic constitutive relations allows the modeled material to sustain high levels of shear with minimum deformation. Thus, implementing a poroelastic model yields unrealistic high shear stress values on materials that have gone beyond a shear failure envelope (Nikolinakou et al., 2012). The poroelastoplastic model, on the other hand, predicts shear stress that facilitates porosity loss and permanent deformation (Zoback, 2010), and allows for a more realistic prediction of stress and pore pressure.

This research is motivated by limitations identified by Burgreen-Chan et al. (2015) in their modeling of the East Coast Basin, New Zealand. Their poroelastic model, though providing good prediction for stress and pressure associated with compression, does not account for the effects of rock failure. Observations of fractures in outcrops (Field et al, 2004) as well as modeling results from Burgreen-Chan et al. (2015) indicate that natural hydraulic fracturing likely began during the onset of subduction (early Miocene). By not considering plastic deformation, their result has no stress limit at which failure would occur, and pore pressure prediction may be erroneous as stresses in the model exceed failure criterion (Figure 1).

A case study from the Managas Fold and Thrust Belt, Venezuela, by Hantschel et al. (2011) confirms that poroplastic approach yields generally lower stresses in the deeper part of the basin (Figure 2). This can be explained by shear-enhanced compaction mechanism. The Cam-Clay model is one constitutive relation that models this behavior. The elastoplastic stress path approaches the shear failure line and does not follow the normal compaction line (elastic stress path). The mean confining pressure at which a certain end-cap (failure envelope) is reached will decrease as shear stress increases (Zoback, 2010).

The simplified synthetic model by Nikolinakou et al. (2012) analyzes stress and pore pressure perturbation on sediment wall rocks around a spherical salt body. The effective stress increases next to the flank of the salt body, resulting in plastic behavior and decreases above and below salt, resulting in elastic behavior. The plastic approach (Figure 3C and 3D) results in relatively greater deformation and smaller changes of vertical effective stress in the region that yields compared to the poroelastic approach (Figure 3A and 3B).

We are currently building a synthetic model after Nikolinakou et al. (2012) using a finite-element multi-physics solver (COMSOL) to validate their numerical results. Following this initial step, the tested workflow can be applied to more complicated synthetic models and real case studies. We will test for the most appropriate poro-elasto-plastic constitutive relations for modeling basin scale deformation over geologic times. We also plan to include the effects of variable lithological facies and rock strength anisotropies arising from sub-grid heterogeneity. Sone et al. (2013) used shale-gas reservoir samples to show that the ductile creep property and brittle strengths are dependent on material composition and sample anisotropy. Thus, modeling inelastic behaviors of poroplastic materials in BPSM also requires calibration with experimental results in addition to advanced plasticity formulations.

The overall goals of this study are to (1) address the effects of plastic deformation in the context of the geological setting, and (2) propose workflows that enables a more robust poroplasticity treatment in BPSM. Poroplastic extensions in BPSM can significantly improve our understanding of stress-strain behaviors and overpressure generation. Successfully adding poroplasticity into BPSM will provide a more reliable basin analysis tool, especially if the validation to regional scale stress regimes is possible.

References

Burgreen-Chan, B., Meisling, K.E., Graham, S.A., 2015. Basin and petroleum system modelling of the East Coast Basin, New Zealand: A test of overpressure scenarios in a convergent margin. Basin Res. 1–32. doi:10.1111/bre.12121

Field, B.D., Higgs, K.E., Chanier, F., Nicol, A. and Darby, D., 2004. Play concepts for a complex margin: East Coast North Island, New Zealand. *In* 2004 New Zealand Petroleum Conference Proceedings, Ministry of Economic Development, Wellington, New Zealand.

Hantschel, T., Wygrala, B., Fuecker, M. and Neber, A., 2011, January. Modeling basin-Scale geomechanics through geological time. In International Petroleum Technology Conference.

Nikolinakou, M.A., Luo, G., Hudec, M.R. and Flemings, P.B., 2012. Geomechanical modeling of stresses adjacent to salt bodies: Part 2—Poroelastoplasticity and coupled overpressures. AAPG Bulletin, 96(1), pp. 65-85.

Sone, H. and Zoback, M.D., 2013. Mechanical properties of shale-gas reservoir rocks—Part 2: Ductile creep, brittle strength, and their relation to the elastic modulus. Geophysics, 78(5), pp.D393-D402.

Zoback, M.D., 2010. Reservoir geomechanics. Cambridge University Press.

Figures

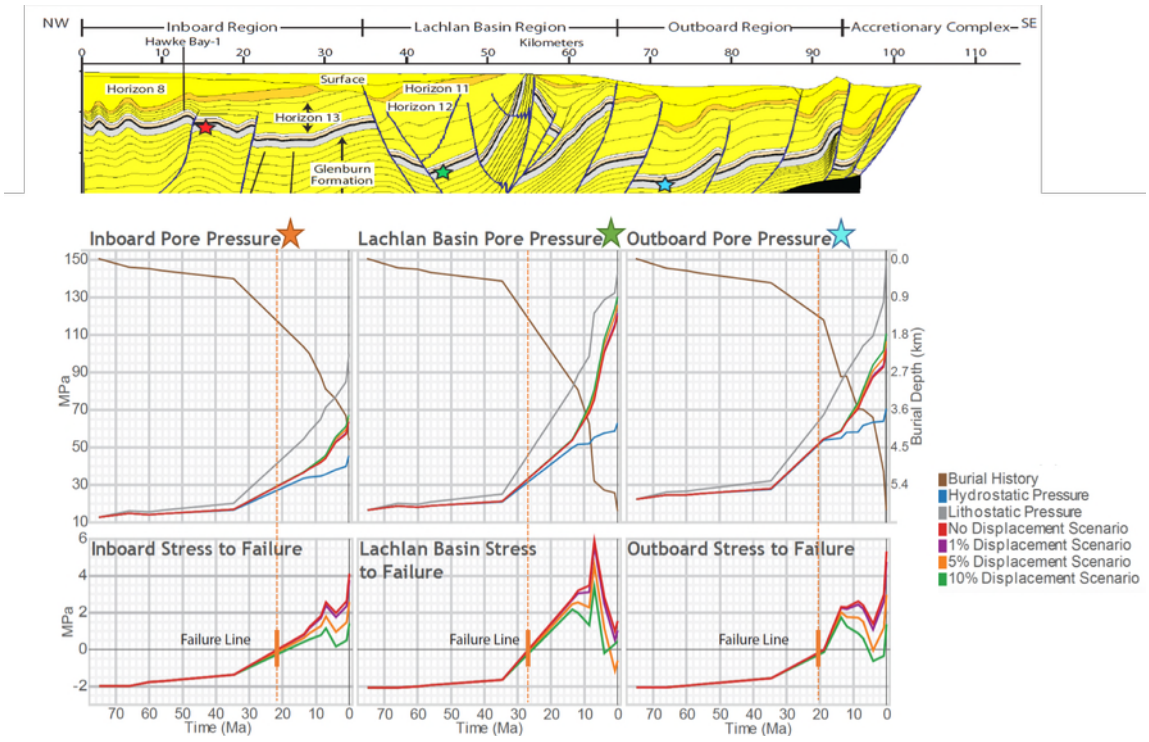

Figure 1: Pore pressure evolution and stress to failure of the Whangai Formation in the Inboard, Lachlan Basin, and Outboard regions of the East Coast Basin, New Zealand using the poroelastic model (see star markers for extraction locations). Failure occurs within the Whangai Formation around the beginning of shortening, although the associated plastic deformation and effects on pore pressure are not considered (Burgreen-Chan et al., 2015).

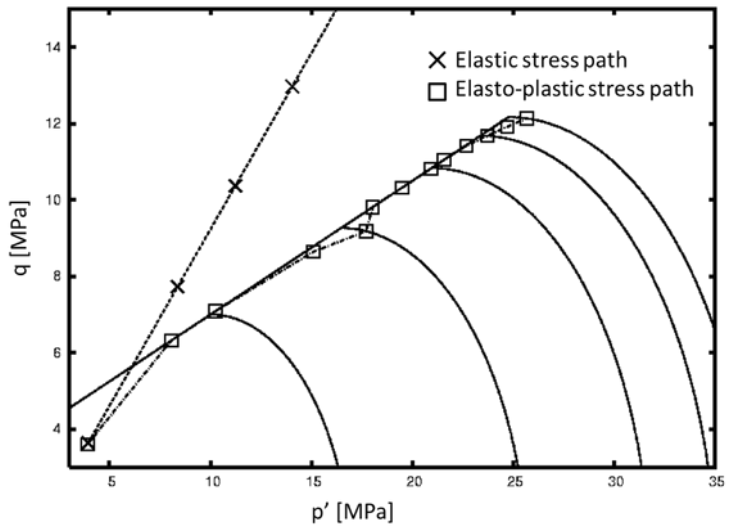

Figure 2: Stress paths for a grid cell at 3km depth calculated with the poroelastic (x) and poroplastic method (□) in a model of the Manogas Fold and Thrust Belt (Hantschel et al., 2011).

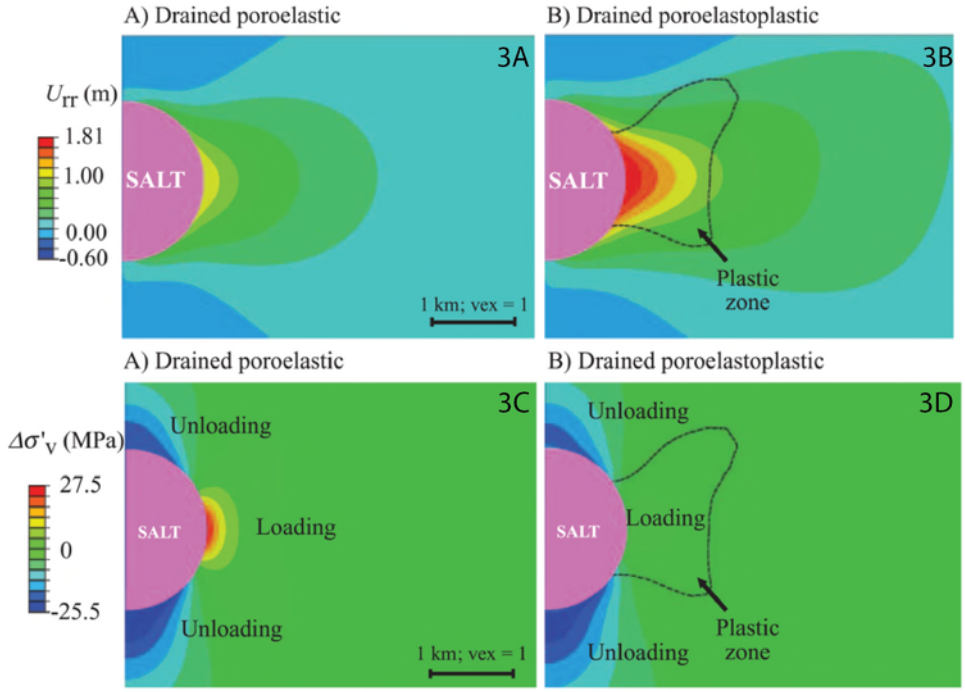

Figure 3: Comparison of deformation and changes of vertical effective stress of surrounding sediment wall rocks predicted by poroelastic and poroelastoplastic models for drained case (Nikolinakou et al., 2012).

THE EFFECT OF CHANGES IN PERMEABILITY DURING MATURATION ON PORE PRESSURE AND PETROLEUM MIGRATION IN BPSM

Krongrath Suwannasri[1,*], Noelle Schoellkopf[2,3], Allegra Hosford Scheirer[2]
[1]*Department of Geophysics, Stanford University*
[2]*Department of Geological Sciences, Stanford University*
[3]*Schlumberger*
[*]krath@stanford.edu

Permeability is a primary control on pore pressure and petroleum fluid migration in basin and petroleum system modeling (BPSM). Recent pyrolysis experiments show that its value changes significantly during thermal maturation (Figure 1). The increase in shale permeability during the thermal maturation process—immature to oil and gas windows—is 10 to 20 fold. Current BPSM practice mainly treats permeability as a function of porosity. The increase in permeability during thermal maturation is often accommodated by enhanced porosity such as secondary organic porosity. However, the expulsion of petroleum from kerogen could generate microcracks and substantially alter the microstructure of the source rock (Vernik, 1992, 1993, 1994; Vernik and Landis, 1996). Thus, porosity enhancement likely does not fully represent the entire increase in permeability during thermal maturation. Therefore, the BPSM workflow should include changing porosity-permeability functions during the thermal maturation process. This study proposes a new BPSM workflow that changes porosity-permeability relationships with increasing thermal maturity. This new workflow will be based on lab experiments and initially incorporated into BPSM using a simple stratigraphic column and a simple burial history. The end result will be comparisons of pore pressure and petroleum migration predictions between the models using variable and constant porosity-permeability relationships during thermal maturation.

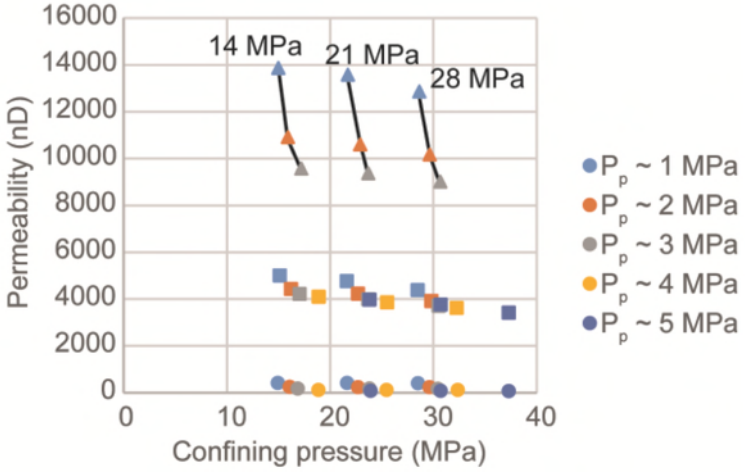

Figure 1: Changes in permeability from the immature (circle), to oil (square), and gas (triangle) windows from pyrolysis results (Allan, Clark and Vanorio, 2015).

References

Allan, A. M., Clark, A. C. and Vanorio, T. (2015) 'Pyrolysis-Induced Evolution of the Elastic and Transport Properties of the Barnett Shale', pp. 3068–3073.

Vernik, L. (1992) 'Ultrasonic velocity and anisotropy of hydrocarbon source rocks', Geophysics, 57(5), p. 727. doi: 10.1190/1.1443286.

Vernik, L. (1993) 'Microcrack-induced versus intrinsic elastic anisotropy in mature HC-source shales', Geophysics, 58(11), p. 1703. doi: 10.1190/1.1443385.

Vernik, L. (1994) 'Hydrocarbon-generation-induced microcracking of source rocks', Geophysics, 59(4), p. 555. doi: 10.1190/1.1443616.

Vernik, L. and Landis, C. (1996) 'Elastic anisotropy of source rocks: Implications for hydrocarbon generation and primary migration', AAPG Bulletin, 80(4), pp. 531–544. doi: 10.1306/64ED8836-1724-11D7-8645000102C1865D.